Design of Permanent Magnetic Solenoids for REGAE

Master thesis
by
Tim Gehrke

Universität Hamburg
Department Physik
10. Juli 2013

Gutachter: Prof. Dr. Florian Grüner
Zweitgutachter: Dr. Klaus Flöttmann

Abstract

The Relativistic Electron Gun for Atomic Exploration (REGAE) is a small linear accelerator at DESY in Hamburg, which produces short, low emittance electron bunches. It is originally designed and built for ultrafast electron diffraction (UED) within the framework of the Center for Free-Electron Laser Science (CFEL).
Aditionally, two future experiments are planned at REGAE. First, an external injection experiment for Laser Wakefield Acceleration (LWA) will be performed in the framework of the LAOLA collaboration (LAboratory fOr Laser- and beam-driven plasma Acceleration). This experiment will provide a method for the reconstruction of the electric field distribution within a linear plasma wakefield. Second, a time resolving high energy Transmission Electron Microscope (TEM) will be implemented. Among others it is designed to allow for living cell imaging.
Both experiments require strong focusing magnets inside the new target chamber at REGAE. Permanent magnetic solenoids (PMSs) can provide the needed focusing strength due to their enormous surface current density, while having compact dimensions at the same time.
The present thesis deals with the design of such strong focusing PMSs. Since short and strong solenoids, as required for REGAE, exhibit a distinct non-linearity, the induced emittance growth is relatively large. This emittance growth is investigated and minimized for different set-ups with axially and radially magnetized annular magnets. Furthermore a magnetic shielding is developed. Together with a mechanical lifting system it assures that magnetic leakage fields do not disturb experiments, where the PMSs are removed from the beamline.

Zusammenfassung

REGAE ist ein kleiner Linearbeschleuniger am DESY in Hamburg, der ultrakurze Elektronenpakete mit kleinen Emittanzen erzeugen kann. Am Center for Free-Electron Laser Science (CFEL) wurde er ursprünglich für zeitaufgelöste Elektronenbeugung entwickelt. Außer der Elektronenbeugung sind zwei weitere Experimente bei REGAE geplant. Einerseits wird ein Experiment zur externen Injektion für *Laser Wakefield Acceleration* (LWA) im Rahmen der LAOLA-Kooperation (LAboratory fOr Laser- and beam-driven plasma Acceleration) durchgeführt werden. Ein wichtiges Ziel ist hierbei, das elektrische Feld eines linearen *Wakefields* direkt zu rekonstruieren. Andererseits kann REGAE nach einigen Modifikationen auch als zeitauflösendes Hochenergie-Transmissionselektronenmikroskop betrieben werden. Es wird unter anderem ermöglichen, lebende biologische Zellen mit zeitlicher Auflösung abzubilden.
Beide zukünftigen Experimente benötigen stark fokussierende Elemente innerhalb der neuen Probenkammer bei REGAE. Permanentmagnetische Solenoide (PMSs) sind sehr kompakt und können gleichzeitig die benötigten Fokussierstärken liefern.
Die vorliegende Arbeit beschäftigt sich mit dem Design stark fokussierender PMSs. Gerade die kurzen und starken Solenoide, die für REGAE benötigt werden, weisen eine ausgeprägte Nichtlinearität auf. Dies führt zu einem relativ großen Emittanzwachstum. Die Zunahme der Emittanz wird bei verschiedenen Solenoiden aus axial- und radialmagnetisierten ringförmigen Permanentmagneten untersucht und minimiert. Außerdem wird eine magnetische Abschirmung entwickelt. Sie sorgt zusammen mit einem mechanischen Hubsystem dafür, dass der Betrieb von Experimenten, bei denen die PMSs aus dem Strahlengang gefahren sind, nicht durch magnetische Randfelder der PMSs gestört werden.

Contents

1 Introduction **7**
- 1.1 REGAE and ultrafast electron diffraction 8
- 1.2 External Injection 11
- 1.3 Transmission Electron Microscope 14

2 Physical basics **19**
- 2.1 Beam dynamics in solenoids 19
  - 2.1.1 Descriptive explanation of beam rotation and focusing in a solenoid 20
  - 2.1.2 Formal explanation of beam rotation and focusing in a solenoid . . 24
  - 2.1.3 Emittance growth induced by a solenoid 26
- 2.2 Generation of solenoidal magnetic fields 31
  - 2.2.1 Electromagnetic solenoid 31
  - 2.2.2 Permanent magnetic solenoid 35

3 Design of a permanent magnetic solenoid **41**
- 3.1 Axially magnetized solenoid 46
- 3.2 Modulation of the inner radius for an axially magnetized solenoid 54
- 3.3 Two axially magnetized solenoids 58
- 3.4 Pair of radially magnetized solenoids 62

4 Development of a magnetic shielding **67**
- 4.1 Magnetic shielding of an axially magnetized solenoid 68
  - 4.1.1 Suitable materials 72
  - 4.1.2 Thickness modulation along the shielding 75
  - 4.1.3 Dimensions of the shielding 78
  - 4.1.4 Influence on the focusing properties of the PMS 80
- 4.2 Magnetic shielding of two radially magnetized solenoids 81
  - 4.2.1 Thickness modulation along the shielding 84
  - 4.2.2 Influence on the focusing properties for two radially magnetized solenoids 87

5 Technical Implementation **91**
5.1 Implementation of two radially magnetized solenoids 91
5.2 Redesign of the magnetic shielding 93
5.3 Effects of the segmentation and production tolerances 96

6 Conclusion and Outlook **101**

Bibliography **105**

1 Introduction

In this thesis, the development of a permanent magnetic solenoid (PMS) is presented. Permanent magnetic solenoids are, different than electromagnetic solenoids, rather unusual focusing elements in particle accelerators [1, 2], due to the fact, that they cannot be adjusted in focusing strength. Besides this drawback, with which one has to deal, permanent magnetic solenoids are an interesting alternative when a low energy beam has to be strongly focused. Due to the enormous remanent magnetic flux density up to $B_R = 1.47\,\mathrm{T}$ [3], which today's permanent magnetic materials exhibit, compact PMSs can reach focusing strengths, which are hardly achievable by water cooled, normal conducting electromagnetic solenoids [4].
Such compact, strong focusing elements are needed for two future experiments at the Relativistic Electron Gun for Atomic Exploration (REGAE), a small linear accelerator on the DESY campus in Hamburg:

- An external injection experiment for laser wakefield acceleration (LWFA) will be performed, beginning in autumn 2013. It is going to merge conventional and laser wakefield accelerators by utilizing the sub 10 fs short, low emittance electron bunches, which REGAE can produce, in order to investigate a linear wakefield [5]. Accelerating electron bunches on different phases of the wakefield and performing a subsequent diagnostic, this pump-probe experiment will provide a method for direct reconstruction of the electric field within the wakefield. Therefore, it can be an important complement to theoretical models and particle-in-cell (PIC) simulations, describing and optimizing laser wakefields for electron acceleration. In order to inject the electron bunch into the wakefield, which has a transverse size of about 100 µm, the bunch has to be strongly focused by the PMS to reach its design beam diameter below 6 µm (rms). A small beam size at the target is crucial for the transverse resolution. Furthermore, a matching condition with respect to the transverse size has to be fulfilled in order to avoid a large emittance growth during the injection process [6].
  Besides the required strong focusing strength, the emittance growth, induced by the PMS's nonlinearity, should be as small as possible. Assuming that the spot

size on the target should stay below its limit, the beam divergency scales linearly with the emittance on the target, i.e. it increases for higher emittances.

- The second experiment, a dynamic Transmission Electron Microscope (TEM), is planned to be performed in late 2013 as well. Running REGAE with a mean beam energy of about 3 MeV and modifying the set-up of focusing elements to enable real space imaging, yields the possibility to operate a high energy TEM. Regarding multiple and inelastic scattering events, which decrease the resolution, increase the sample damage and limit the maximal sample thickness, a high energy TEM offers advantages over a conventional TEM (operated at a few hundreds of keV).
  The latter two advantages of a decreased sample damage and an increased maximal sample thickness could allow to perform living cell imaging with a high energy TEM. As REGAE is designed for ultrashort bunches, dynamic living cell imaging on the ps-scale could be feasible. The above mentioned modification of the focusing elements consists of a condenser lens in front of the sample, an objective lens directly behind the specimen and intermediate lenses before the screen. The condenser and the objective lens are identical and require a large focusing strength, in order to achieve large magnifications.
  As for the external injection, efforts should be made to keep the emittance growth small. In section 2.1.3 it will be shown, that the emittance growth is closely linked to the spherical aberrations of a lens, which is decisive for a TEM. Because of the same requirements, the PMS in front of the target position can be shared by both experiments. At the target position will be a lifting system, which allows to interchange the gas and the liquid cell for both experiments.

In the following three sections the accelerator REGAE, developed for ultrafast electron diffraction, and the two future experiments, that require the PMS – designed within this thesis–, are introduced in more detail.

1.1 REGAE and ultrafast electron diffraction

The Relativistic Electron Gun for Atomic Exploration (REGAE) is a compact linear accelerator on the DESY campus in Hamburg. The new accelerator has been built within the framework of the Center for Free-Electron Laser Science (CFEL), which is a collaboration of the Max Planck Society, the University of Hamburg and DESY. In November 2011, the first electrons were accelerated.
It is originally designed for ultra fast electron diffraction (UED), which is already performed at REGAE at the moment. The aim of UED is, to resolve transition states in

complex chemical molecules spatially as well as temporally. Expressing it descriptive, the vision is to "make a molecular movie" [7, 8], which shows chemical reactions. Such a tool would lead to a deeper understanding of chemical reactions and would have a huge influence, not only in chemistry but in biology and medicine as well. The wish to resolve single atoms inside the molecule, which are traveling the characteristic length, a bond length, on a timescale $< 100\,\mathrm{fs}$, directly defines the requirements concerning spatial and temporal resolution.
With REGAE's relativistic electrons that allow atomic resolution, its design bunch length of 7 fs (rms) and a predicted synchronization jitter between laser and RF-system $< 20\,\mathrm{fs}$ (rms), the requirements for the investigations are fulfilled. The method, used to achieve temporal resolution, is reminiscent of a stroboscopic process. The laser pulses from the Ti-sapphire laser (situated in the laser room on the level below the REGAE beamline) are split into two parts before one part induces the electron emission on the cathode. The second part is directed onto the sample, where it induces the chemical reaction and marks the moment $t = 0$. By means of a delay line in the laser path of the second part, the time delay between the pump laser pulse and the probe electron bunch is tunable. This so called pump-probe experiment allows to take images at different times during the reaction. Putting them together results in a movie of the reaction.

The ultra fast electron diffraction requires exceptional beam parameters. The following part will explain which beam parameters REGAE can provide and how they are achieved. REGAE can generate ultrashort electron bunches (sub 10 fs (rms)) with low emittances ($< 0.02\ \pi$ mm mrad) and a mean beam energy of about 5.6 MeV. The bunch charge is variable between 80 fC and several 10 pC. In order to achieve these remarkable beam parameters, REGAE has many specialized accelerator elements. A schematic of REGAE is shown in figure 1.1, by which the electron's path can be traced and all important parts are briefly described. The description is partly based on [10].
The first part of the accelerator is the RF gun, a 1.6 cell standing-wave cavity operated at 3 GHz (S-band). In the backplane of the gun, a Cesium Telluride photo cathode emits the electron bunch after illumination by a frequency tripled (266 nm), pulsed Ti-sapphire laser. The maximal repetition rate is 50 Hz. After injection the electrons are accelerated by the sinusoidal RF-field of the gun. The challenging and indispensable synchronization of laser pulse and RF-field (design jitter below 10 fs (rms)) ensures that the bunch is accelerated on-crest, which leads to a maximal mean beam energy of about 5.6 MeV.
The bunch then passes the first beam optics elements, where the bunch is focussed and its transverse position can be corrected. A correction is achieved by so called steerer magnets, a combination of two orthogonally positioned small dipoles, which give a kick to the electrons, adjusted by the dipole's field strength [11]. The first focussing is done by electromagnetic solenoids, whose operation is explicitly explained in section 2.1. Be-

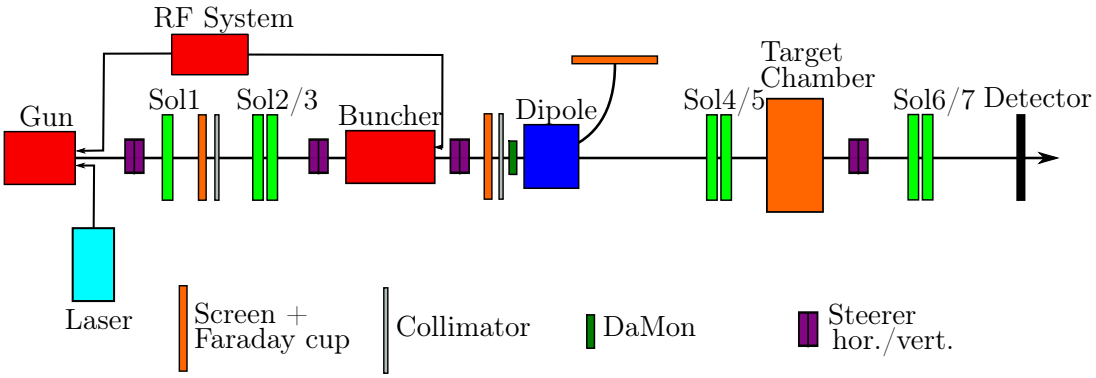

Figure 1.1 – Schematic of REGAE. Courtesy of [9], modified

sides the alignment of the beam onto the desired target position, matching the electrons trajectory with the solenoid's symmetry axis is the most important task of the steerers. Behind these beam optics elements, the bunch enters the S-band 4 cell standing-wave buncher cavity. Instead of further acceleration, this cavity can be used as bunching element if the electrons are injected into the sinusoidal RF-field at its zero crossing. Operation of the cavity at its so called bunching phase leads to the process of ballistic bunching. In the course of this, electrons in the front part of the bunch are decelerated while the rear electrons are accelerated, due to the steep rising slope around the zero crossing. This induced, almost linearly correlated energy spread of some 10 keV leads to a bunch length minimum approximately 4.2 m behind the buncher cavity, where the rear electrons overtake the front electrons. Simulations for REGAE predict a minimum bunch length of 7 fs (rms).

Having left the buncher cavity, the electrons pass a further steerer and solenoid until the bunch enters the target chamber. Here, the electrons hit the sample to be investigated. At the moment, the target chamber at REGAE hosts the electron diffraction. For the two future experiments, the external injection and the TEM set-up, a new target chamber is designed. It will allow to perform all three experiments at REGAE. Here, a lifting system inside the chamber can realize the required target and solenoid configuration in each case.

After interaction with the target, the beam can be focused and steered one more time before it hits the detector at the end of the accelerator. The data, recorded with this detector, are the essential results of the different experiments. Therefore the detector meets high requirements. It is a particularly sensitive scintillator screen, which allows to detect single electrons [12].

Further beam diagnostics are integrated along the whole accelerator and consist of three faraday cups with additional LYSO scintillator screens, indicated in figure 1.1 as screens.

The third screen is behind a dipole magnet, which is used as dispersive element for energy and energy spread measurements. Since these charge measurements are destructive, they are complemented by a cavity monitor (DaMon), which enables non-destructive charge measurements. When bunches pass the cavity, a voltage is induced, which is related to a certain bunch charge.
Recently two collimators were installed into the beam path. They provide apertures with different sizes that reduce the dark currents. These dark currents surround the actual bunch and cause an increased noise in the experimental results.
Furthermore an earth magnetic field compensation is installed. It consists of a Helmholtz-like coil pair, which compensates the dominant vertical component of the external field [13].

1.2 External Injection

In 2010, the idea emerged to use REGAE for a different interesting application, namely the investigation of laser induced wakefields inside a plasma [5]. These wakefields are in turn employed for particle acceleration, in so called laser wakefield acclerators (LWFA) [14, 15]. LWFAs utilize high power laser pulses ($\gg 1\,\mathrm{TW}$). Focusing such a laser pulse onto a gas target, its pre-pulses are intense enough to ionize the gas completely, so that the main pulse is propagating within a plasma. The main pulse exhibits intensities, where the ponderomotive force, acting on the plasma's electrons, is not negligible anymore. It displaces the electrons radially along the propagation direction of the laser, leading to a charge separation since the heavier ions are barely influenced. Behind the laser pulse, the removed electrons are again attracted by the ions, which finally leads to oscillations with a wavelength λ_p that is inversely proportional to the square root of the initial electron density. These oscillations are shown for the case of a linear wakefield (planned at REGAE) in figure 1.2.
Wakefields exhibit electric field strength on the order of $100\,\mathrm{GV/m}$, with which injected electrons can be accelerated very effectively. In comparison to maximum electric fields in conventional RF systems on the order of $100\,\mathrm{MV/m}$, the enormous field strength of a LWFA turns out to be one of its most important advantages. It will give rise to very compact accelerators.
In 2006, the generation of an electron beam with $1\,\mathrm{GeV}$ energy was accomplished on an acceleration distance of a few centimeters [16]. A further advantage is the intrinsically short bunch length, which results from the fact that self injected electrons are accelerated in electric fields with a typical wake-wavelength λ_p of about several $10\,\mu\mathrm{m}$. Additionally, the direct available synchronization between the electron bunch and a laser pulse, which

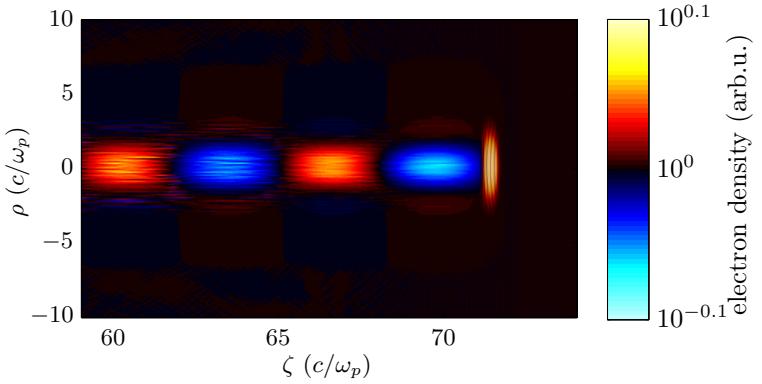

Figure 1.2 – Particle-in-cell (PIC) simulation of a quasi linear wakefield. The laser pulse, shown on the right side of the graph, generates strong charge separations inside the plasma. The oscillating electron density along the z-axis forms the linear wakefield, which exhibits an enormous longitudinal electric field. Courtesy of Christian Werle (*CFEL Hamburg*).

is branched off from the driver laser, is a valuable benefit. These unique features attract the attention to LWFAs as source of brilliant, ultrashort x-ray pulses [17–19].
LWFAs even have the potential to realize table-top free-electron lasers (FEL) [20–22]. If this goal is achieved, it will have a great impact on natural sciences since the availability of FELs, the fourth-generation x-ray sources with many important applications, would be drastically increased. It has already been shown that the requirement of a small transverse emittance for FELs can be met with LWFAs [23]. But two other important parameters for the realization of an FEL, the energy spreadand the shot-to-shot stability concerning energy and pointing, need to be further improved.Both parameters are dependent on the injection process. Among others, a much-noticed injection scheme, called bubble regime [24], exhibits a lack of controllability during the process, since plasma electrons are statistically scattered into a highly non-linear wakefield (self injection).
A deeper understanding and optimization of the injection process could lead to an improved energy spread and shot-to-shot stability. The external injection experiment at REGAE approaches to the problem at this point. By injecting a REGAE electron bunch with the above mentioned parameters into a linear or mildly non-linear wakefield, the injection mechanism should be sufficiently determined. The phase, at which the bunch is injected, will be varied and the energy spectrum, pointing, emittance and further parameters can be analyzed for every shot after injection and acceleration inside the plasma. The more controllable injection and the systematical investigation of the right timing could lead to the desired improvement of energy spread and stability. Furthermore, this experiment will give rise to a method of reconstruction of the electric field distribution

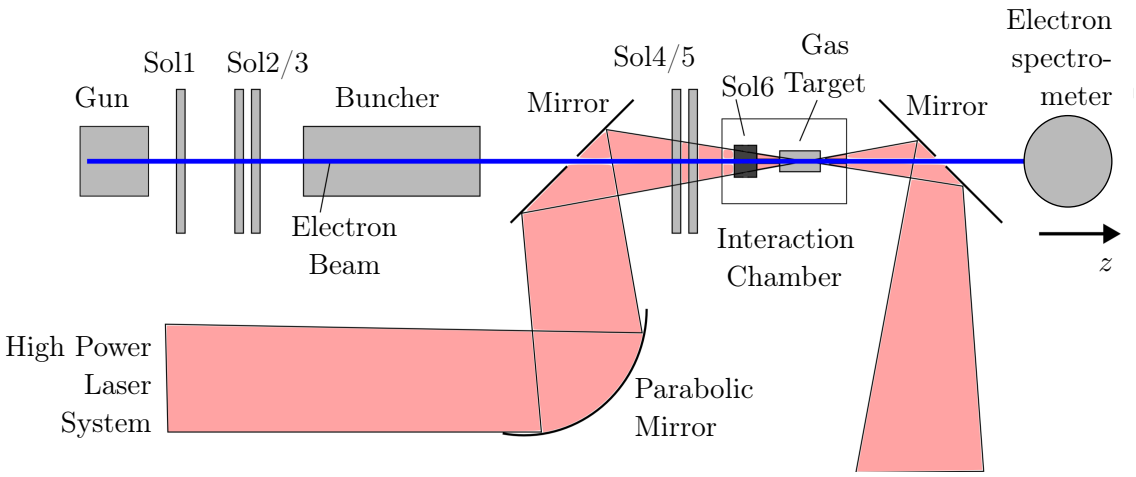

Figure 1.3 – Necessary modifications in the rear part of REGAE in order to perform the External injection experiment. Courtesy of [25].

within the wake and therefore provide the important experimental data besides theoretical models and PIC simulations. Last but not least, it will be a proof of principal for staging LWFAs, since the external injection is mandatory for the connection of at least two LWFAs.

As already mentioned, REGAE is in principle suitable for the external injection scheme, since the accelerator provides ultrashort electron bunches that are predestined for mapping a wakefield. Nevertheless, there are several modifications that need to be performed at REGAE in order to realize the experiment. They are indicated in figure 1.3.
First of all, a high power laser system has to be integrated into the experimental set-up, so that the electron bunch and the laser pulse can collinearly propagate to the target chamber. Since the introduction of a gas target requires additional measures to retain a vacuum with DESY specifications [26], a new target chamber has to be designed. Furthermore, a new imaging electron spectrometer (detection of an energy range between 1 MeV to 30 MeV; if needed extendable to higher energies with lower resolution) has to be installed for the diagnostics of the electron beam after the interaction with the wakefield. Comparing the design parameters of the ongoing electron diffraction experiment and the external injection, which are given in table 1.1, one can see that another element is needed. The beam has to be focused in order to decrease the actual beam radius by about two orders of magnitude for the external injection. A small beam spot size is crucial for the transversal resolution during the mapping of the wakefield. Hence, a strong focusing solenoid is required. The decision to utilize a permanent magnetic solenoid for this application and further design considerations are discussed in detail in chapter 3.

Design parameters	Diffraction	External Injection
Energy	ca. 5 MeV	5.6 MeV
Energy spread	20 keV	20 keV
Bunch charge	80 fC	100 fC
Bunch length	7 fs (rms)	< 10 fs (rms)
Transverse size	300 µm -600 µm (rms)	< 3 µm (rms)
Transverse emittance	0.02 π mm mrad	0.03 π mm mrad

Table 1.1 – Comparison of the design parameters for the electron diffraction and the external injection experiment

1.3 Transmission Electron Microscope

Since the first development of a transmission electron microscope (TEM) in 1932 [27], the TEM underwent a vast improvement of its spatial resolution and is still the instrument with an unprecedented subatomic resolution of 0.05 nm [28]. It plays a key role in imaging materials of physical, technological and biological interest in real space with atomic resolution. Especially the detection of defects in solid's lattices and their influence on the properties of the investigated material is an important application since these defects can hardly be detected with electron or x-ray diffraction.
In the following, a typical ray path for a TEM is briefly described. Electrons are emitted in the electron gun by thermionic, field or photo emission. The field emission provides the highest gun brightness (because of its small source spot size of ca. 10 nm), but if it is coming to temporal resolution the photo emission is preferable (because of its much higher current, which is needed to generate a distinct image within a short time) [29]. In conventional TEMs, the acceleration voltage inside the electron gun ranges between 100 kV and 500 kV. Behind the gun, the electrons pass a condenser lens system, which allows to collimate the beam and to adjust the area of the specimen illuminated.
In the sample, the electrons interact strongly with the atoms by elastic and inelastic scattering. The total cross section of these interactions are at least four orders of magnitudes larger than for the interaction of x-rays with atoms. While x-rays are only scattered on the electron distribution of the sample, electrons are scattered by the electron distribution as well as by the atomic nuclei. Regarding this fact, TEMs provide distinct pictures within a short "exposure time", which is only achieved by x-rays if the number of photons is orders of magnitudes higher than the number of electrons. For several materials, the large amount of photons causes a higher radiation dose than the smaller amount of electrons [30]. Concerning biological samples, a small radiation dose is an important criterium for a suitable imaging method. The disadvantage of a conventional TEM, re-

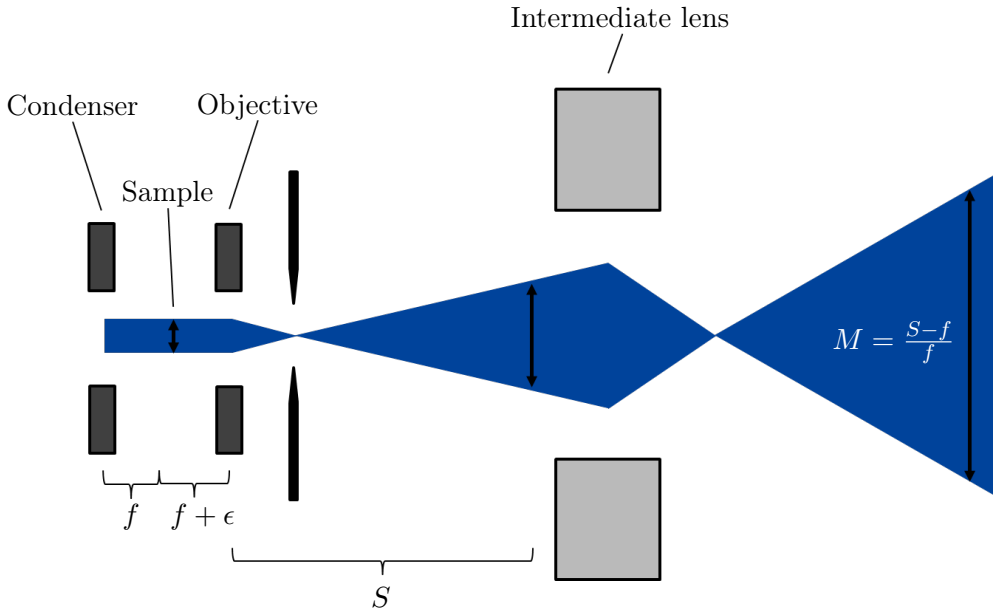

Figure 1.4 – Typical beam path of a TEM. The last condenser lens and the objective lens are going to be realized as PMSs. The given formula shows that a small focal length is needed for a large magnification. The ϵ indicates that the sample is not directly positioned in the focal plane of the objective lens, which is necessary to obtain a magnified picture.

lated to the large total cross section, is the small probe depth of electrons (10 nm-1 µm compared to several 10 µm for x-rays). Therefore, the possible sample thicknesses, which are suited for TEM investigations, are limited by the probe depth of 1 µm.
After the interaction with the thin sample, the electron-intensity distribution is imaged with an objective lens, one or more intermediate lenses and a projector lens onto a fluorescent screen, which is coupled to a CCD camera. The intermediate and projector lenses further increase the magnification M behind the objective, while the decisive lens for the resolution limit, set by spherical aberrations, is the objective lens. The fact that the first intermediate picture (second black arrow in figure 1.4) is already magnified by the objective lens, leads to lower requirements for the intermediate lenses concerning resolution. A schematic of a TEM set-up is shown in figure 1.4.

Since REGAE's electron gun is designed for high brightness beams, it is in principal possible to realize a TEM set-up at REGAE if the required lenses, indicated in figure 1.4, are fitted subsequently. The fact that REGAE can easily provide mean beam energies of about 3 MeV allows not only the operation of a conventional TEM (acceleration voltages smaller than 500 keV) but the operation of a high energy TEM (acceleration voltages up

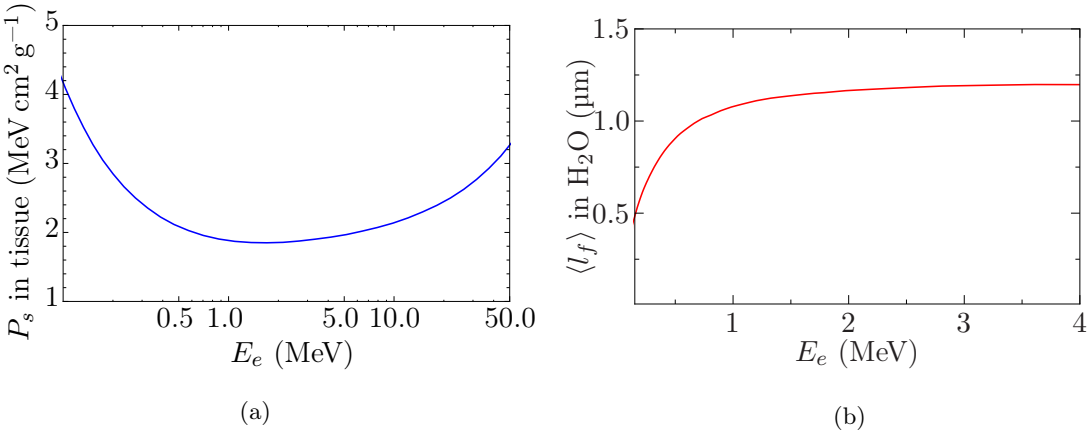

Figure 1.5 – (a) Total stopping power in tissue P_w over the kinetic energy of electrons E. (b) Mean free path $\langle l_f \rangle$ in water over the kinetic energy of electrons. It is comparable to the mean free path in tissue. [31]

to 5 MeV). Such a high energy TEM at REGAE is going to have two major advantages over TEMs with smaller acceleration voltages. The first advantage is the possibility to operate a TEM with a time resolution on the order of ps. REGAE uses the photo emission to generate electrons. This method allows to form ps electron bunches with at least 10^6 electrons (in case of utilizing field emission the bunch length is approx. 1 ms, assuming comparable bunch charge). This number of electrons is a rough orientation for the required amount of electrons that can form a single-shot image with sufficient contrast. In connection with the high beam energy, which has the important consequence that space charge effects are reduced, temporal resolutions on the order of a ps are conceivable for pump probe experiments. Compared to time resolutions of a conventional TEM on the order of ms, it constitutes a huge improvement and could lead to the observation of fundamental interactions with ps duration in biological samples. The second advantage is that the high energy beam allows to investigate specimen with increased thickness. The reason for that is the minimal inelastic scattering cross section at 3 MeV in tissue, which corresponds to minimal absolute energy losses ΔE within the sample. Hence, the relative energy losses $\Delta E/E$, which cause chromatic aberrations in the objective lens and therefore diminish the resolution, are significantly reduced compared to electron beams with less energy. This allows the mentioned increase of sample thickness and leads to reduced radiation damage due to ionization. Additionally, the mean free path for the elastic scattering of electrons in aqueous samples is increased for higher electron energies as well. It further improves the resolution for thicker samples [31]. The total stopping power in tissue P_s, correlated with inelastic scattering, and the mean free path

in water $\langle l_f \rangle$ are plotted against the electron's kinetic energy in figure 1.5. These major advantages could make it possible to perform time resolved living cell imaging at REGAE. This method would be a valuable tool for biological and medical research in order to get deeper insights in complex processes on the above named time and length scales within an intact cell.

2 Physical basics

In the introduction two future experiments at REGAE, the external injection and the transmission electron microscope, were presented. As briefly described in chapter 1 and discussed in more detail in chapter 3, there is a necessity for both experiments to integrate complementary strong focusing solenoids into the beamline of REGAE. One important part of the present master thesis is the design of these solenoids.
For the design, it is crucial to understand the solenoid's characteristics from a beam dynamics point of view. Therefore the derivations of the three most important characteristics, the rotation of the beam about the z-axis φ_L, the focusing strength $1/f$ and the emittance growth $\epsilon_{\mathrm{n,rms}}$, are performed in the following section 2.1.
Having deduced that every solenoid field exhibits focusing characteristics, the subsequent section 2.2 is about the generation of such fields. Two devices for the generation of magnetic fields that are in principal suitable for REGAE, the electromagnetic solenoid and the permanent magnetic solenoid (PMS), are introduced.
The decision for a permanent magnetic solenoid inside the target chamber (cf. chapter 3) leads to the necessity to utilize a magnetic shielding, surrounding the PMS (cf. chapter 4). Basic information about magnetic shieldings can be found for example in [32–34]. The considerations in the given literature are based on assumptions, which are not satisfied for a magnetic shielding of a PMS (e.g. homogenous magnetic fields or neglecting saturation effects in shielding materials). Therefore they do not lead to a solution for the present problem and are not introduced here. For more complex problems, the literature refers to Finite Element Method (FEM) simulations, which are directly used in chapter 4. The basics, which are presented in the following, are important for the design of the required solenoid and will be frequently used in chapter 3.

2.1 Beam dynamics in solenoids

An electromagnetic solenoid is, different than a permanent magnetic solenoid, a common element of particle accelerators, which is used to focus charged particle beams. Therefore, the term solenoid is mostly applied for a current-carrying coil, that produces a magnetic field. But in this thesis the term solenoid is used more generally and describes any device,

which produces a cylindrically symmetric magnetic field with a longitudinal component $B_z \neq 0$, especially including annular permanent magnets and the above named coils. In the course of this thesis, annular permanent magnets and coils are referred to as permanent magnetic solenoids (PMSs) and electromagnetic solenoids, respectively. All these solenoids yield a focusing characteristic for charged particle beams [35]. Due to the fact, that the solenoid's focal length f is proportional to the square of the particles' longitudinal momentum p_z^2, it is mainly applied in low energy parts of accelerators and other devices with lower particle energies, for example electron microscopes. For higher energies ($E_{\text{kin}} \gg 1\,\text{MeV}$) quadrupole lenses are more effective since their focal length is proportional to p_z, not to p_z^2 [36, 37]. In order to understand the characteristics of a solenoid, especially the focusing of charged particle beams (in the following an electron beam is considered), two explanations are given. The first explanation is rather descriptive and applied to the simplest case of a solenoid while the second is more formal, having validity for every rotationally symmetric magnetic field [38]. Both deliver the same expressions for the rotation of the beam about the z-axis φ_L and for the focusing strength $1/f$. Concerning the derivation of the emittance growth, induced by the solenoid's non-linearity, it is convenient to utilize the formal explanation.

2.1.1 Descriptive explanation of beam rotation and focusing in a solenoid

The following explanation, based on [37], is supposed to create an image of the focusing process in a solenoid in the reader's mind. Therefore the most simple model of a solenoid, the hard edge approximation, is assumed. Here, the longitudinal field can be considered as constant inside the annular solenoid $B_z = B_0$ and zero outside.
As can be seen in the following expansions [39], cylindrically symmetric fields are fully determined by the longitudinal on-axis field B_z. For the longitudinal magnetic field $B_{z,\text{gen}}$ holds

$$\begin{aligned} B_{z,\text{gen}}(z,r) &= \sum_{n=0}^{\infty} \frac{(-1)^n}{(n!)^2} \left(\frac{r}{2}\right)^{2n} \frac{\partial^{2n} B_z}{\partial z^{2n}} \\ &= B_z - \frac{r^2}{4}\frac{\partial^2 B_z}{\partial z^2} + \frac{r^4}{64}\frac{\partial^4 B_z}{\partial z^4} - \cdots, \end{aligned} \tag{2.1}$$

while the radial component B_r can be written as

$$\begin{aligned} B_r(z,r) &= \sum_{n=1}^{\infty} \frac{(-1)^n}{n!(n-1)!} \left(\frac{r}{2}\right)^{2n-1} \frac{\partial^{2n-1} B_z}{\partial z^{2n-1}} \\ &= -\frac{r}{2}\frac{\partial B_z}{\partial z} + \frac{r^3}{16}\frac{\partial^3 B_z}{\partial z^3} - \frac{r^5}{384}\frac{\partial^5 B_z}{\partial z^5} + \cdots. \end{aligned} \tag{2.2}$$

Here, r and z are cylindrical coordinates. This expansion allows to determine the radial magnetic field for the hard edge solenoid.

$$\begin{aligned} B_r(z,r) &= -\frac{r}{2}B_z' + \cancel{\frac{r^3}{16}B_z'''} + \dots \\ &= -\frac{r}{2}[B_0(\Theta(z+L/2) - \Theta(z-L/2))]' \\ &= -\frac{r}{2}B_0\left(\delta(z+L/2) - \delta(z-L/2)\right), \end{aligned} \tag{2.3}$$

where L is the solenoid's length, $\Theta(z)$ the Heaviside function and $\delta(z)$, its derivative, the Dirac delta distribution. If a beam is assumed, whose particles have no initial transverse velocity, the trajectory of any particle will be straight in front and behind the solenoid and helical inside the solenoid. Entering the solenoid, the particle obtains an azimuthal momentum because of the Lorentz force:

$$\gamma m\dot{v}_\varphi = -ev_z B_r(z) \tag{2.4}$$

$$\gamma m\dot{v}_\varphi = ev_z\frac{r_0}{2}B_0\delta(v_z t) \tag{2.5}$$

$$v_\varphi = \frac{r_0 eB_0}{2\gamma m} = r_0\omega_L, \tag{2.6}$$

where m is the electron rest mass, e the elementary charge, $\gamma = \left(1-\beta^2\right)^{-1/2}$, $\beta = v/c$ with v as particle velocity and c as speed of light in vacuum. r_0 is the initial radial coordinate and $\omega_L = eB_0/(2\gamma m)$ the well-known Larmor frequency.
As the transversal velocity changes, it is evident that v_z changes as well since the particle's energy is conserved in magnetic fields. But the change of the longitudinal velocity will be neglected in the paraxial approximation, which is justified later on in the formal explanation. Now, with the given transverse velocity, the radius of the helical trajectory r_h in the longitudinal field B_0 is easily computed by

$$-ev_\varphi B_0 = \frac{\gamma m v_\varphi^2}{r_h} \Leftrightarrow r_h = \frac{\gamma m v_\varphi}{eB_0} = \frac{r_0}{2}. \tag{2.7}$$

Equation (2.7) shows that every off-axis particle undergoes a helical trajectory with a radius $r_0/2$, which corresponds to half of the initial radial displacement. If these trajectories are projected into the transversal x-y-plane, as illustrated in figure 2.1 (a), it is directly visible, that the beam is focused by a hard edge solenoid. In the case of a very long solenoid, the beam undergoes periodic focusing. The particles' trajectories are shown as black, dashed circles, whereas their starting points A, B, C, D lie on the initial circumference, that is depicted as blue circle. After the beam has passed a certain

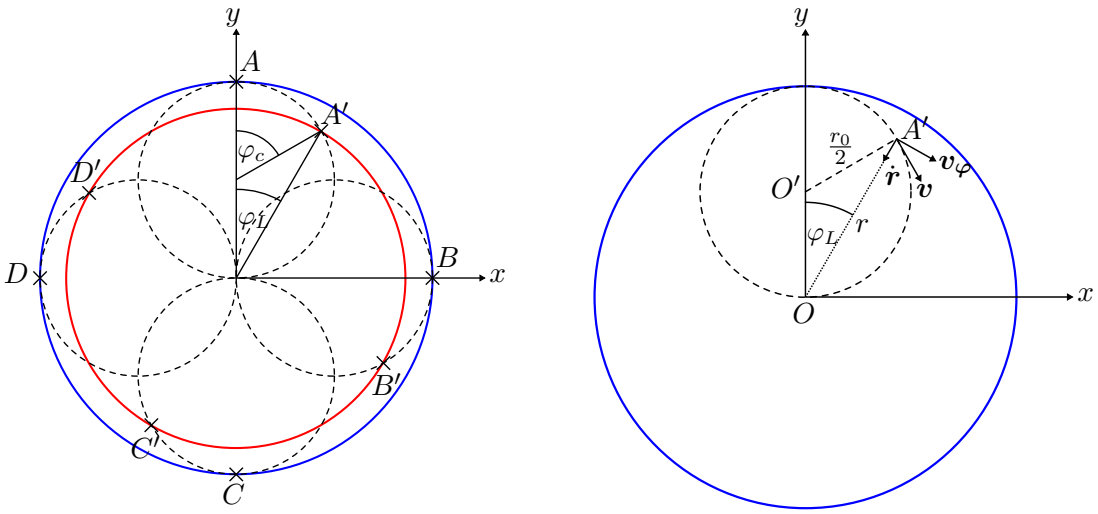

Figure 2.1 – (a) Schematic explanation of the focusing process in a solenoid and the difference between Larmor frequency and cyclotron frequency. The blue circle shows the initial beam size, which decreases inside the solenoid (red circle). Trajectories of single electrons are depicted with dashed circles. The relation between cyclotron angle and Larmor angle, $\varphi_c = 2\varphi_L$, is recognizable.
(b) The two velocity components in the transversal plane $\dot{\boldsymbol{r}}$ and $\boldsymbol{v_\varphi}$ are shown. They refer to the solenoid axis O and not to the axis of helical motion O'. The initial azimuthal coordinate φ_0 is $\pi/2$ with respect to the x-axis [37]

distance inside the solenoid, the actual particle's positions are A', B', C', D', which lie on the new circumference, depicted as red curve. In figure 2.1 the difference between the Larmor frequency and the cyclotron frequency can be seen as well. Of course, the electron rotates with the cyclotron frequency with respect to its "own" axis O', as expected for an electron inside a homogenous magnetic field. But with respect to the solenoid's axis O, it rotates with half the cyclotron frequency, referred to as Larmor frequency.
In a last step the particle's azimuthal and radial velocity at the transition to the field-free region is determined. Using figure 2.1 (b), the azimuthal and radial coordinate inside the solenoid can be expressed by

$$\varphi = \varphi_0 + \omega_L t \tag{2.8}$$

$$r = r_0 \cos(\omega_L t), \tag{2.9}$$

which leads after differentiation to

$$v_\varphi = r\omega_L \tag{2.10}$$

$$\dot{r} = -r\omega_L \tan(\omega_L t). \tag{2.11}$$

At the rear edge, the azimuthal velocity is exactly compensated by the Lorentz force due to v_z and B_r. Hence, there is no rotation of the beam in the field-free region and the total angle of the rotation, induced by the solenoid, can be given as

$$\varphi_L = \omega_L \frac{L}{v_z} = \frac{eB_0 L}{2\gamma v_z}. \tag{2.12}$$

In contrast, the radial velocity is not affected by the transition and thus is given by

$$\dot{r} = -r_1 \omega_L \tan\left(\frac{\omega_L L}{v_z}\right), \tag{2.13}$$

where r_1 denotes the radial coordinate at the rear edge. This equation states that there is a focal point in the field-free region.
If one now refers the thin lens approximation to the expression of the radial velocity, it reads as

$$\dot{r} = -\frac{re^2}{4\gamma^2 m^2 v_z} B_0^2 L, \tag{2.14}$$

using $\tan(x) \approx x$ for $x \ll 1$.
The results for the rotation angle φ_L and the radial velocity $\dot{r}$ can be further generalized to a thin solenoid without the requirement of a hard edge by approximating an arbitrary longitudinal field with a piecewise constant function. The result for φ_L, the so called Larmor angle, is then

$$\varphi_L = \int \omega_L \frac{\mathrm{d}t}{\mathrm{d}z} \mathrm{d}z = \frac{e}{2\gamma m v_z} \int B_z \mathrm{d}z, \tag{2.15}$$

while for the radial velocity, the following expression is valid

$$r' = \dot{r}\frac{1}{v_z} = -\frac{re^2}{4\gamma^2 m^2 v_z^2} \int B_z^2 \mathrm{d}z. \tag{2.16}$$

It leads to the well-known focal length f in thin lens approximation by using $-r'/r = f$:

$$\frac{1}{f} = \frac{e^2}{4\gamma^2 m^2 v_z^2} \int B_z^2 \mathrm{d}z. \tag{2.17}$$

The integrals, occurring in these expressions, are defined as the field integrals

$$\begin{aligned} F_1 &= \int B_z \mathrm{d}z \\ F_2 &= \int B_z^2 \mathrm{d}z, \end{aligned} \tag{2.18}$$

meaning that the Larmor angle is proportional to F_1 and the focusing strength is proportional to F_2.

2.1.2 Formal explanation of beam rotation and focusing in a solenoid

The two important relations (2.15), (2.17) and additionaly the emittance growth can be deduced in a formal way, starting with the relativistic Lorentz force equation for an electron within a magnetic field $\boldsymbol{B}$

$$\gamma m \ddot{\boldsymbol{r}} = -e\dot{\boldsymbol{r}} \times \boldsymbol{B}, \tag{2.19}$$

where $\boldsymbol{r}$ denotes the position vector of the electron and dots indicate time derivatives. γ is constant here, since electric fields are not present (space charge is neglected) and magnetic fields do not influence γ. Adapting to the cylindrical symmetry of the solenoid, it is convenient to express x, y and z by the cylindrical coordinates so that $\boldsymbol{B}$ can be described with only two components B_r, $B_{z,gen}$:

$$\begin{aligned} \boldsymbol{r} &= \begin{pmatrix} r\cos\varphi \\ r\sin\varphi \\ z \end{pmatrix}, & \dot{\boldsymbol{r}} &= \begin{pmatrix} \dot{r}\cos\varphi - r\dot{\varphi}\sin\varphi \\ \dot{r}\sin\varphi + r\dot{\varphi}\cos\varphi \\ \dot{z} \end{pmatrix}, \\ \ddot{\boldsymbol{r}} &= \begin{pmatrix} \ddot{r}\cos\varphi - 2\dot{r}\dot{\varphi}\sin\varphi - r\dot{\varphi}^2\cos\varphi - r\ddot{\varphi}\sin\varphi \\ \ddot{r}\sin\varphi + 2\dot{r}\dot{\varphi}\cos\varphi - r\dot{\varphi}^2\sin\varphi + r\ddot{\varphi}\cos\varphi \\ \ddot{z} \end{pmatrix}, & \boldsymbol{B} &= \begin{pmatrix} B_r\cos\varphi \\ B_r\sin\varphi \\ B_{z,gen} \end{pmatrix}. \end{aligned} \tag{2.20}$$

Inserting (2.20) in (2.19), where φ can be set to 0 without loss of generality because of the cylindrical symmetry, leads to three coupled differential equations

$$\gamma m(\ddot{r} - r\dot{\varphi}^2) = -er\dot{\varphi}B_{z,gen} \tag{2.21}$$

$$\gamma m \frac{d}{dt}\left(r^2\dot{\varphi}\right) = er\dot{r}B_{z,gen} - erB_r\dot{z} \tag{2.22}$$

$$\gamma m\ddot{z} = er\dot{\varphi}B_r \tag{2.23}$$

In order to eliminate B_r and $B_{z,\mathrm{gen}}$ one can use the important expansions (2.1) and (2.2) so that the properties of the solenoid can be described only by the longitudinal on-axis field $B_z := B_{z,gen}(r,z)|_{r=0}$ and its derivatives with respect to z $B_z', B_z'', \ldots$. In a first approach, the expansion is truncated after first order terms in r which is the first assumption of the paraxial approximation.

$$\gamma m(\ddot{r} - r\dot{\varphi}^2) = -er\dot{\varphi}B_z \tag{2.24}$$

$$\gamma m\frac{d}{dt}\left(r^2\dot{\varphi}\right) = eB_z r\dot{r} + e\frac{r^2}{2}B_z'\dot{z} = \frac{d}{dt}\left(\frac{e}{2}r^2B_z\right) \tag{2.25}$$

$$\gamma m\ddot{z} = -\frac{e}{2}B_z' r^2\dot{\varphi}. \tag{2.26}$$

Equation (2.25) can be easily integrated and results in

$$\gamma m r^2\dot{\varphi} = \frac{e}{2}r^2B_z + C. \tag{2.27}$$

If one considers a beam, with zero initial momentum in the field-free region, the constant of integration vanishes ($C = 0$). The angular velocity then reads as

$$\dot{\varphi} = \frac{e}{2\gamma m}B_z = \omega_L, \tag{2.28}$$

which is the well-known Larmor frequency. Inserting the Larmor frequency into (2.24), (2.26) yield two differential equations in r and z, respectively:

$$\ddot{r} = -\left(\frac{e}{2\gamma m}\right)^2 rB_z^2 \tag{2.29}$$

$$\ddot{z} = -\left(\frac{e}{2\gamma m}\right)^2 r^2B_zB_z' \tag{2.30}$$

In (2.30) it is noticeable that the longitudinal velocity v_z will change, which is comprehensible since the transversal velocity will change as well and energy conservation must hold. However, it is a second order effect and can therefore be neglected for higher beam energies. Together with the truncation after first order terms in r in the expansion of cylindrically symmetric fields, this assumption forms the paraxial approximation.
Finally, (2.29) is the differential equation for the radial motion, which can be written with the longitudinal coordinate as independent variable, using $\ddot{r} = r''\dot{z}^2 \approx r''(\beta c)^2$ since $\ddot{z}$ is zero in this approximation. The following equation is the well-known paraxial ray equation

$$r'' = -\left(\frac{e}{2p_z}\right)^2 rB_z^2. \tag{2.31}$$

After the integration of (2.31) with respect to z, application of the thin lens approximation, which states that r remains constant during the passage through the solenoid, and usage of the relation $-r'/r = 1/f$ it yields the expression for the focusing strength. Together with the integrated formula (2.28), whose independent variable is changed to z as well, the results correspond to the previously found equations (2.15), (2.17) :

$$\varphi_L = \frac{e}{2p_z}\int_{-\infty}^{\infty} B_z \mathrm{d}z = \frac{e}{2p_z}F_1 \tag{2.32}$$

$$\frac{1}{f} = \left(\frac{e}{2p_z}\right)^2 \int_{-\infty}^{\infty} B_z^2 \mathrm{d}z = \left(\frac{e}{2p_z}\right)^2 F_2. \tag{2.33}$$

2.1.3 Emittance growth induced by a solenoid

Having deduced and explained the rotation and the focusing of the beam, another important issue are the aberrations, which are caused by the solenoid's non-linearity, noticeable in (2.1) and (2.2). In the following considerations, aberrations up to the third order ($\propto r^3$) are regarded, that will lead to an emittance growth proportional to a third and fourth field integral F_3, F_4. In order to obtain an expression for the emittance growth,starting point of the discussion are again the three coupled differential equations, that will lead to an equation for the radial momentum. Using this equation for a description of the canonical momentum in Cartesian coordinates, the emittance growth can be deduced.

With the expansion truncated after third order terms in r the differential equations (2.21)-(2.23) read as

$$\gamma m(\ddot{r} - r\dot{\varphi}^2) = -er\dot{\varphi}\left(B_z - \frac{r^2}{4}B_z''\right) \tag{2.34}$$

$$\gamma m\frac{d}{dt}\left(r^2\dot{\varphi}\right) = er\dot{r}\left(B_z - \frac{r^2}{4}B_z''\right) - er\dot{z}\left(-\frac{r}{2}B_z' + \cancel{\frac{r^3}{16}B_z'''}\right) \tag{2.35}$$

$$\gamma m\ddot{z} = er\dot{\varphi}\left(-\frac{r}{2}B_z' + \cancel{\frac{r^3}{16}B_z'''}\right). \tag{2.36}$$

Analogue to the above procedure for the paraxial approximation, equation (2.35) can be integrated, using $\int r^3\dot{r}\mathrm{d}t = \frac{r^4}{4}$ for the additional term. The result is

$$\dot{\varphi} = \omega_L\left(1 - \frac{r^2 B_z''}{8B_z}\right), \tag{2.37}$$

which can be inserted into equation (2.34) and (2.36). After some algebra the differential equations for r and z look like

$$\ddot{r} = -\omega_L^2 r \left(1 - \frac{r^2 B_z''}{2B_z}\right) \tag{2.38}$$

$$\ddot{z} = -\left(\frac{e}{2\gamma m}\right)^2 r^2 B_z B_z' = -\omega_L^2 r^2 \frac{B_z'}{B_z}. \tag{2.39}$$

(2.39) is equivalent to (2.25), but determining third order aberrations, the acceleration in z-direction ($\propto r^2$) cannot be neglected. Since the integration of (2.39) is not possible without further ado, energy conservation can be used in order to obtain an expression for $\dot{z}$, which will be needed for the calculation of $\dot{r}$. The energy conservation can be expressed by

$$(\beta_0 c)^2 = \dot{z}^2 + r^2\dot{\varphi}^2 + \cancel{\dot{r}^2}, \tag{2.40}$$

where $\beta_0 c$ denotes the initial velocity, assumed to be parallel to the z-axis, and the right hand side is the velocity composition inside the solenoid. The contribution of $\dot{r}^2$ to the total velocity can be neglected, since the longitudinal and the azimuthal velocity component are much larger (cf. figure 2.1). Therewith the longitudinal velocity can be written as

$$\dot{z} = \sqrt{\beta_0^2 c^2 - r^2\omega_L^2 \left(1 - \frac{r^2 B_z''}{\cancel{2B_z}}\right)} = \beta_0 c \left(1 - \frac{r^2 e^2 B_z^2}{8 p_{z,0}^2}\right), \tag{2.41}$$

where r^4-terms are neglected and the square root is approximated by $\sqrt{1-x} = 1 - x/2$ for $x \ll 1$. $p_{z,0} = \gamma m \beta_0 c$ is the initial moment. Now, $p_r = \gamma m \dot{r}$ can be computed by inserting (2.41) for $\dot{z}$:

$$\begin{aligned} p_r &= \gamma m \int -\omega_L^2 r \left(1 - \frac{r^2 B_z''}{2B_z}\right) \frac{\mathrm{d}t}{\mathrm{d}z} \mathrm{d}z \\ &= -\frac{e^2}{4\gamma m \beta_0 c} \int \left(r B_z^2 - \frac{r^3 B_z'' B_z}{2}\right) \frac{1}{1 - \frac{r^2\omega_L^2}{2\beta_0^2 c^2}} \mathrm{d}z \\ &= -\frac{e^2 r}{4 p_{z,0}} \underbrace{\int B_z^2 \mathrm{d}z}_{F_2} + r^2 \underbrace{\int -\frac{B_z'' B_z}{2} \mathrm{d}z}_{F_3} + \frac{r^2 e^2}{8 p_{z,0}^2} \underbrace{\int B_z^4 \mathrm{d}z}_{F_4}, \end{aligned} \tag{2.42}$$

where in the last step, the geometric series $1/(1-x) = \sum_{n=0}^{\infty} x^n$ for $|x| < 1$ and the thin lens approximation are used, again strictly suppressing terms higher than $\propto r^3$. Moreover, two further field integrals F_3 and F_4 are defined, which will be used in the following.

Having deduced an expression for the azimuthal ((2.37)| $\cdot \gamma m r$) and the radial momentum, one way to determine the emittance growth is to convert to Cartesian coordinates and to utilize the canonical momentum. These calculations are performed for the motion in x-direction, but they are equivalently valid for the y-direction. After the conversion to Cartesian coordinates, the mechanical momentum in x-direction is given by

$$p_x = -\frac{x}{r}\frac{e^2 r}{4p_{z,0}}\left(F_2 + r^2 F_3 + \frac{r^2 e^2}{8p_{z,0}^2}F_4\right) - \frac{y}{r}\frac{er}{2}\left(B_z - \frac{r^2}{8}B_z''\right) \tag{2.43}$$

and the canonical momentum reads as

$$\begin{aligned}\tilde{p}_x &= p_x - eA_x \\ &= p_x + \frac{ey}{2}\left(B_z - \frac{r^2}{8}B_z''\right) \\ &= -\frac{e^2 x}{4p_{z,0}}\left(F_2 + r^2 F_3 + \frac{r^2 e^2}{8p_{z,0}^2}F_4\right).\end{aligned} \tag{2.44}$$

Since the normalized rms emittance is given by

$$\epsilon_{\mathrm{n,rms}} = \frac{1}{mc}\sqrt{\langle x^2\rangle\langle \tilde{p}_x^2\rangle - \langle x\tilde{p}_x\rangle^2}, \tag{2.45}$$

with $\langle\cdot\rangle$ as second central moment, the next step is to evaluate its terms separately:

- $\langle x^2\rangle$:

$$\begin{aligned}\langle x^2\rangle &= \int_{-R}^{R}\int_{-\sqrt{R^2-y^2}}^{\sqrt{R^2-y^2}} x^2 \underbrace{\frac{1}{\pi R^2}}_{f(x,y)}\,\mathrm{d}x\mathrm{d}y \\ &= \frac{R^2}{4},\end{aligned} \tag{2.46}$$

  where a normalized two dimensional uniform distribution for the transverse beam profile $f(x, y)$ is assumed. This is a valid description of the REGAE beam as long as a laser with transverse top head profile is utilized on the photocathode. It is planned for both future experiments. In general $\langle x^2\rangle$ is always proportional to σ_x^2, independently from the assumed transverse distribution. Only the proportionality factor is dependent on the distribution.

- $\langle \tilde{p}_x^2 \rangle$:

$$\begin{aligned}\langle \tilde{p}_x^2 \rangle =& \frac{e^4\langle x^2 \rangle}{16p_{z,0}^2}F_2^2 + \frac{e^4\langle x^2r^4 \rangle}{16p_{z,0}^2}F_3^2 + \frac{e^8\langle x^2r^4 \rangle}{1024p_{z,0}^6}F_4^2 \\ &+ \frac{2e^4\langle x^2r^2 \rangle}{16p_{z,0}^2}F_2F_3 + \frac{2e^6\langle x^2r^2 \rangle}{128p_{z,0}^4}F_2F_4 + \frac{2e^6\langle x^2r^4 \rangle}{128p_{z,0}^4}F_3F_4 \\ =& \frac{e^4R^2}{64p_{z,0}^2}F_2^2 + \frac{e^4R^6}{128p_{z,0}^2}F_3^2 + \frac{e^8R^6}{8192p_{z,0}^6}F_4^2 \\ &+ \frac{e^4R^4}{48p_{z,0}^2}F_2F_3 + \frac{e^6R^4}{384p_{z,0}^4}F_2F_4 + \frac{e^6R^6}{512p_{z,0}^4}F_3F_4,\end{aligned} \tag{2.47}$$

  where the occurring second central moments $\langle x^2r^2 \rangle = R^4/6$, $\langle x^2r^4 \rangle = R^6/8$ have been calculated analogously to (2.46).

- $\langle x\tilde{p}_x \rangle^2$:

$$\begin{aligned}\langle x\tilde{p}_x \rangle^2 &= \left(-\frac{e^2\langle x^2 \rangle}{4p_{z,0}}F_2 - \frac{e^2\langle x^2r^2 \rangle}{4p_{z,0}}F_3 - \frac{e^4\langle x^2r^2 \rangle}{32p_{z,0}^3}F_4 \right)^2 \\ &= \left(-\frac{e^2R^2}{16p_{z,0}}F_2 - \frac{e^2R^4}{24p_{z,0}}F_3 - \frac{e^4R^4}{192p_{z,0}^3}F_4 \right)^2 .\end{aligned} \tag{2.48}$$

Inserting these terms into expression (2.45) finally leads to

$$\begin{aligned}\epsilon_{\mathrm{n,rms}} &= \frac{1}{mc}\left(\frac{e^4R^8}{4608p_{z,0}^2}F_3^2 + \frac{e^8R^8}{294912p_{z,0}^6}F_4^2 + \frac{e^6R^8}{18432p_{z,0}^4}F_3F_4 \right)^{1/2} \\ &= \frac{1}{mc}\left(\frac{e^4R^8}{4608p_{z,0}^2}F_3^2\left(1 + \frac{e^2}{4p_{z,0}^2}\frac{F_4}{F_3} + \frac{e^4}{64\cancel{p_{z,0}^4}}\frac{\cancel{F_4^2}}{F_3^2} \right) \right)^{1/2} \\ &= \frac{1}{mc}\left(\frac{e^2R^4}{48\sqrt{2}p_{z,0}}F_3 + \frac{e^4R^4}{384\sqrt{2}p_{z,0}^3}F_4 \right) \\ &= \frac{1}{mc}\left(\frac{e^2\sigma^4}{3\sqrt{2}p_{z,0}}F_3 + \frac{e^4\sigma^4}{24\sqrt{2}p_{z,0}^3}F_4 \right),\end{aligned} \tag{2.49}$$

where $F_4/F_3 \ll 1$ is assumed, so that the $(F_4/F_3)^2$-term is canceled and the expansion of the square root is applicable. This assumption is justified since the F_4-term only

results from the small change in longitudinal velocity, which is dependent on the beam energy and mainly has to be taken into account for non relativistic energies (cf. (2.41)). In the last step, the rms value $\sigma = R/2$ for a symmetric beam $\sigma_x = \sigma_y = \sigma$ is introduced. The geometrical emittance is simply the product of the normalized emittance and $mc/\bar{p}_z = 1/(\beta\gamma)$ and reads as

$$\epsilon_{rms} = \frac{e^2\sigma^4}{3\sqrt{2}p_{z,0}^2}F_3 + \frac{e^4\sigma^4}{24\sqrt{2}p_{z,0}^4}F_4, \tag{2.50}$$

In the literature about electron optics, other than in the accelerator literature, the spherical aberration coefficient C_s of a solenoid is mostly introduced instead of using the emittance growth ϵ_{rms}. It is given with

$$\begin{aligned} C_s &= \frac{e}{96m\tilde{U}} \int \left(\frac{2e}{m\tilde{U}} B_z^4 + 5\left(B_z'\right)^2 - B_z B_z'' \right) R^4 \mathrm{d}z \\ &= \frac{2e^2R^4}{96p_{z,0}^2} \int \frac{4e^2}{p_{z,0}^2} B_z^4 - 6B_z B_z'' \mathrm{d}z \\ &= \frac{e^2R^4}{4p_{z,0}^2}F_3 + \frac{e^4R^4}{12p_{z,0}^4}F_4, \end{aligned} \tag{2.51}$$

where in the first step the relativistically corrected acceleration potential $\tilde{U}$ is replaced by $\tilde{U} = p_{z,0}^2/(2em)$, the thin lens approximation is applied, which states that R is constant over the magnetic field, and a partial integration of the second term in the integral is performed, which is allowed for an integration over the whole magnetic field of the solenoid. A comparison of both expressions shows, that the third and fourth field integral are decisive for the emittance growth as well as for the spherical aberration. But their prefactors are differently distributed for both expressions, which yields to the fact that F_4-term is $8/3$ times stronger weighted in C_s than in ϵ_{rms}. This difference results most probably from the fact, that in the literature about electron optics a single electron ray is considered.
In conclusion, it is good to see an agreement of these two different concepts, originating from the accelerator and the electron microscopy community. The derivation of the emittance growth might have seemed lengthy but the derivation of the spherical aberration coefficient is much more complex and extends over multiple pages [2, 40]. It shows the utility and comprehensibility of the emittance definition.

The emittance growth of a solenoid will become important in chapter 3, where the design of a permanent magnetic solenoid for REGAE is discussed. One important design criterion is the induced emittance growth. For this practical purpose the thin lens approximation, already introduced in equation (2.42), is still applied. It allows for writing R^4

out of the integrals and leads to an upper limit for the emittance growth in cases where a collimated or convergent electron beam enters the solenoid and the focal point is behind and not in the solenoid (here the beam radius is definitely decreasing inside the solenoid, so that an "effective" beam radius is smaller than the initial one). For divergent incoming beams and a focal length larger than the longitudinal extend of the magnetic field, the thin lens approximation leads to a lower limit of the emittance growth and is therefore not very meaningful. But for the external injection at REGAE, convergent beams at the solenoid are planned. And for the TEM experiment, the last condensor and the objective lens (identical PMSs) should always be arranged symmetrically around the target, so that the R-decrease and increase within both lenses compensate each other. Hence, the thin lens approximation is valid here as well. A second approximation is made by neglecting the fourth field integral. As already mentioned, F_4 originates from the change of the longitudinal velocity inside the solenoid, which is significant for non-relativistic electron energies. Furthermore, the typical field distributions under investigation in chapter 3 yield to values of $F_3/F_4 > 1 \times 10^4\,\mathrm{T}^{-2}\,\mathrm{m}^{-2}$. Together with their prefactors it turns out, that the contribution of F_4 to the emittance growth is on the order of 1 % of the contribution induced by F_3. Thus, F_4 is neglected in the following so that the normalized emittance writes as

$$\epsilon_{\mathrm{n,rms}} = \frac{1}{mc}\frac{e^2\sigma^4}{3\sqrt{2}p_{z,0}}F_3. \tag{2.52}$$

2.2 Generation of solenoidal magnetic fields

In the last paragraph it was shown, that cylindrically symmetric magnetic fields with a longitudinal component $B_z \neq 0$ can be used to focus charged particle beams. This section is about the generation of such magnetic fields. Two types of generations have already been mentioned, namely the electromagnetic solenoid and the permanent magnetic solenoid. These two important examples will be described in more detail here.

2.2.1 Electromagnetic solenoid

The electromagnetic solenoid consists in the simplest case of an air coil with a single layer of windings and without a yoke, as depicted in 2.2 (a). The magnetic field can be calculated by means of Biot-Savart's law. It provides an expression for the longitudinal on-axis field for a single current loop positioned at $z = 0$ with the radius R and current I

$$B_{z,\mathrm{loop}}(z) = \frac{\mu_0 I R^2}{2\left(z^2 + R^2\right)^{3/2}}, \tag{2.53}$$

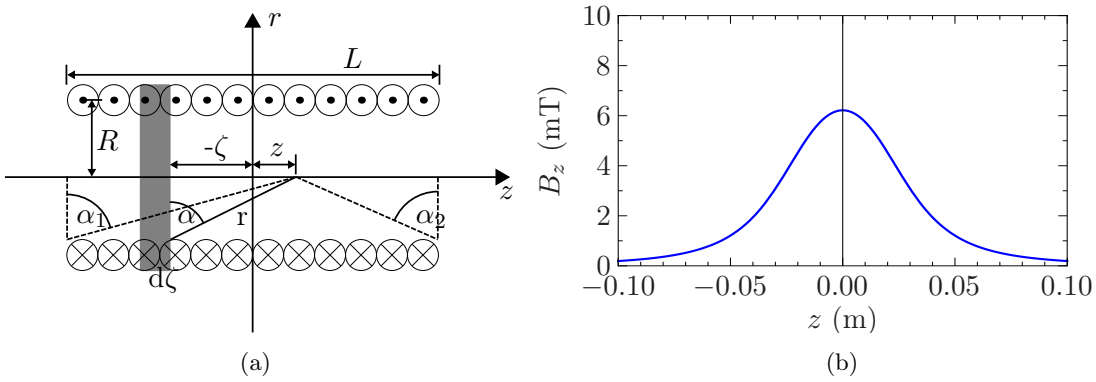

Figure 2.2 – (a) Scheme of an air coil, which illustrates how infinitesimal parts of the coil contribute to the magnetic field at the z-position [41].
(b) Corresponding longitudinal on-axis field for $L = 41.8\,\mathrm{mm}$, $R = 30\,\mathrm{mm}$, $I = 9\,\mathrm{A}$ and $N = 20$ (first layer of the solenoid, used at REGAE).

where $\mu_0 = 4\pi \times 10^{-7}\,\mathrm{Vs/(Am)}$ is the vacuum permeability. This magnetic field can easily be extended to an infinitesimal part of the longitudinal on-axis field of an air coil

$$\mathrm{d}B_z(z) = \frac{\mu_0 I n \pi R^2 \mathrm{d}\zeta}{2\pi \left((z-\zeta)^2 + R^2\right)^{3/2}}, \tag{2.54}$$

where $n = N/L$ denotes the winding's density and all other variables are defined in figure 2.2 (a). Finally, $B_z(z)$ is obtained by integration along the coil's length, which can be done with the substitution $z - \zeta = R\tan(\alpha)$:

$$\begin{aligned} B_z(z) &= \int_{-L/2}^{L/2} \mathrm{d}B_z = -\frac{\mu_0 I n}{2} \int_{\alpha_1}^{\alpha_2} \cos(\alpha)\mathrm{d}\alpha \\ &= \frac{\mu_0 I n}{2} \left(\frac{z + L/2}{\sqrt{R^2 + (z + L/2)^2}} - \frac{z - L/2}{\sqrt{R^2 + (z - L/2)^2}} \right) \end{aligned} \tag{2.55}$$

The magnetic field (2.55), which is illustrated in figure 2.2 (b), will become helpful later in the discussion of permanent magnetic solenoids but common solenoids in particle accelerators are built in a different manner. Here, many of the single-layer windings are laid on top of each other so that, for example, a rectangular cross section of windings results. While figure 2.3 (a) illustrates such a solenoid, which is actually used at REGAE in combination with an iron yoke, the blue curve in figure 2.3 (b) shows the corresponding magnetic field simulated in the Finite-Element-Method (FEM) code Opera-2D [42]. It can be shown that this type of field can be approximated by a field of two current loops,

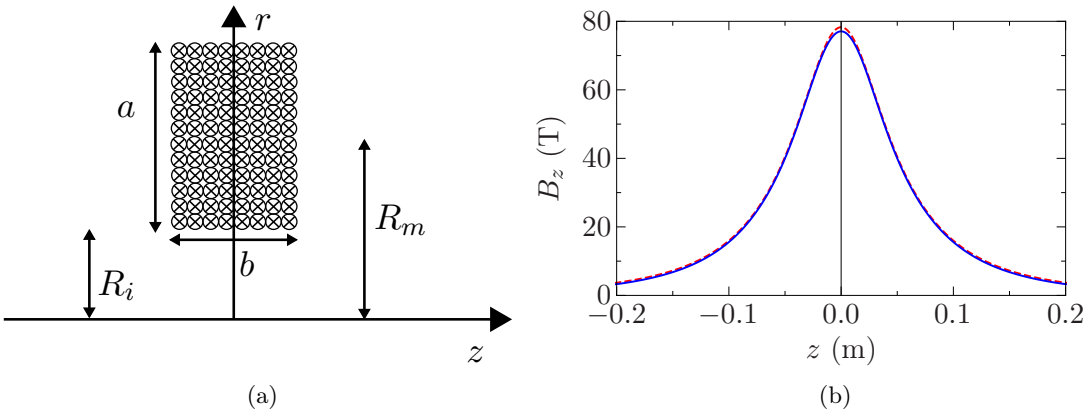

(a) (b)

Figure 2.3 – (a) Scheme of an coil with rectangular cross section (only upper half is shown). Such a coil with parameters $a = 99.5\,\text{mm}$, $b = 41.8\,\text{mm}$, $R_i = 30\,\text{mm}$ and $R_m = 79.75\,\text{mm}$ is used in electromagnetic solenoids at REGAE.
(b) Corresponding longitudinal on-axis field for the above named parameters and $I = 9\,\text{A}$, $N = 1000$. Simulation (blue) and analytical approximation by two current loops (red)

each providing half of the total current, already given in (2.53) [43]. To do so, effective radii of the single loops $R_{sq} + c$, $R_{sq} - c$ are introduced, with

$$\begin{aligned} R_{sq} &= R_m \left(1 + a^2/(24R_m^2)\right) \\ c^2 &= \frac{b^2 - a^2}{12}, \end{aligned} \tag{2.56}$$

where R_m denotes the mean radius, a is the radial dimension and b the axial dimension of the rectangular cross section. For the special case of a square cross section $a = b$, the emerging magnetic field can be described by one single loop current, carrying the total current, with effective radius R_{sq} [44]. For the general case, the approximation finally reads as

$$B_z(z) \approx \frac{\mu_0 N I}{4} \left(\frac{(R_{sq}+c)^2}{(z^2 + (R_{sq}+c)^2)^{3/2}} + \frac{(R_{sq}-c)^2}{(z^2 + (R_{sq}-c)^2)^{3/2}} \right), \tag{2.57}$$

that is shown as red curve in figure 2.3 (b). As can be seen, it is a practical approximation. Regarding figure 2.3 (b), the maximal magnetic flux density along the z-axis of an air coil is not very large and can easily be increased by employing an iron yoke, which shields the coil expect for an air gap on the inner radius of the coil (see 2.4 (a)). This leads to a concentrated on-axis field, often an order of magnitude larger than without

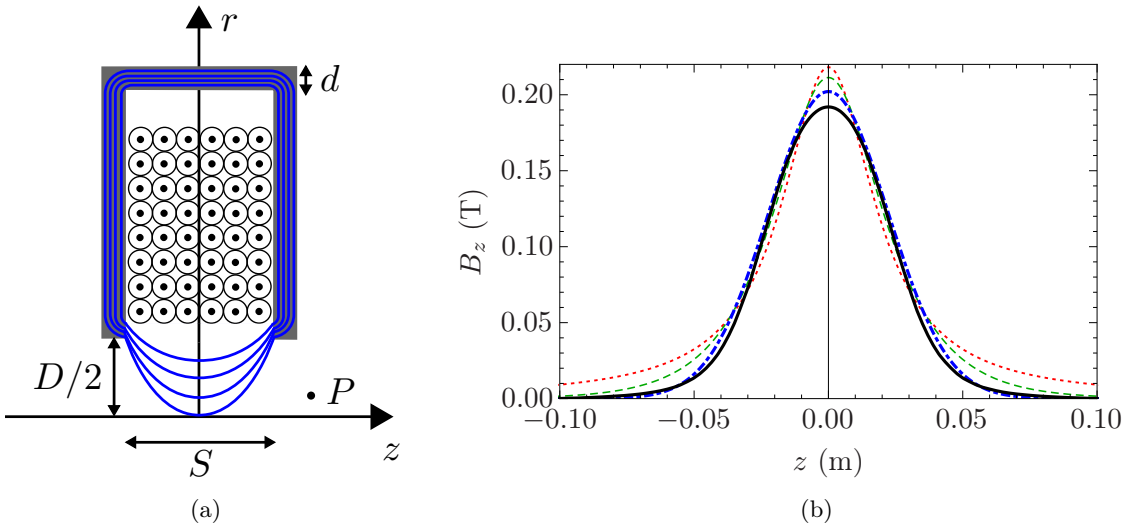

Figure 2.4 – (a) Scheme of an electromagnetic solenoid with iron yoke (only upper half is shown). With coil parameters like in 2.3, yoke thickness $d = 10\,\text{mm}$, bore radius $D/2 = 25\,\text{mm}$ and gap size $S = 41.8\,\text{mm}$ it corresponds to the design, used for REGAE's em-solenoids.
(b) The black curve shows the corresponding measured field map. The red dotted, green dashed and blue dot-dashed curves show the Glaser-, Grivet-Lens- and Gaussian-model respectively. The models are defined in table 2.1

iron yoke, with the consequence, that stronger focusing solenoids can be built, saving electrical power and weight of copper at the same time [1]. The on-axis magnetic field of a shielded coil can be described by bell-shaped curves, where its characteristics are independent of the air coil's shape as long as the iron is not saturated ($\mu_{iron} \gg 1$). If that is the case, the width of the curve (described by the half width at half maximum) is only dependent on the yoke design, characterized by the parameter S/D, not on the number of ampere-turns $I \cdot N$. However, the peak field B_0 is proportional to the number of ampere-turns [38]. If the number of ampere-turns are increased such that saturation effects of iron occurs, it is obvious that the yoke can not lead the total magnetic flux anymore and the magnetic flux density is increased in the bore at positions further away from the gap S (see position P in figure 2.4 (a)). Hence, the bell-shaped curve will become broader and B_0 will not rise linearly with $I \cdot N$ but converge. Due to many different designs of pole pieces and the saturation effects, numerous fitting models for the bell-shaped curves have been published [40, 45–47]. They all have validity for different reasons like good agreement for non-saturated or saturated iron yokes, analytic solvability of the paraxial ray equation and so forth. In this thesis, the most common

Model	Description of $B_z(z)$	F_2/F_3
Glaser [40]	$\frac{B_0}{1+z^2/w^2}$	$4w^2$
Grivet-Lenz [45]	$B_0\,\mathrm{sech}(1.32\frac{z}{w})$	$3.44w^2$
Gaussian	$B_0 \exp\left(-\ln(2)\frac{z^2}{w^2}\right)$	$2w^2/\ln(2)$

Table 2.1 – Mathematical description of the longitudinal on-axis field in common models for electromagnetic solenoids with iron yoke. The parameter w is the half width at half maximum. In figure 2.3 one can see, that the Glaser model exhibits a wider field distribution than the other two models. It leads to a better ratio of focusing strength and emittance growth (larger F_2/F_3).

Glaser-, Grivet-Lenz- and a Gaussian distribution are compared by fitting a measured fieldmap of REGAE's single electromagnetic solenoid. The models are defined in table 2.1 and the result of the comparison is shown in figure 2.4 (b). As one can see, both, the Glaser- and the Grivet-Lenz model decrease more slowly than the measured field distribution. Furthermore their curves, fitted with the least-squares method, exhibit an approximately 10 % higher peak field than the real magnetic field. These differences from the real solenoidal field will cause significant errors in the calculation of the focal length and the induced emittance growth. Surprisingly, the Gaussian distribution, which is not mentioned as model for solenoids in literature, reproduces the decreasing and the peak of the field noticeably better. Thus, during the selection of the most suitable model for a real solenoid, several models should be compared, since the most common models do not have validity for any yoke design. In the next section, it is shown that this problem does not occur for permanent magnetic solenoids since it is not necessary to utilize iron yokes and the field distribution is assessable by Biot-Savart's law.

2.2.2 Permanent magnetic solenoid

After this introduction to electromagnetic solenoids, which explained why most of the accelerators and electron microscopes are using the concept of the shielded electromagnetic solenoid and how the emerging magnetic field can be described, the next paragraph deals with the permanent magnetic solenoid (PMS). First, the physics of a permanent magnet is shortly presented, which yields a description of a solenoid's magnetic field. Different than for an electromagnetic solenoid, a PMS with iron yoke is not necessary due to its intrinsic strong fields. Finally pros and cons towards electromagnetic solenoids are discussed.

Permanent magnets are based on ferromagnetic materials like iron-, nickel- and cobalt-alloys, which have the particular property to retain their magnetization after they have experienced a field. Especially two rare earth alloys, samarium cobalt (SmCo) and neodymium (NdFeB) magnets with a large remanence field of $B_{\mathrm{R,SmCo}} = 1.12\,\mathrm{T}$ and $B_{\mathrm{R,NdFeB}} = 1.47\,\mathrm{T}$ are widely used since their discovery in the early 1970' and 1981.
Microscopically, the magnetic field is generated by atomic magnetic moments $\boldsymbol{p_m}$, caused by circular currents of the atom's electrons. The vector sum of these magnetic moments per volume element $\boldsymbol{M} = \frac{1}{V}\sum_V \boldsymbol{p_m}$ results in the macroscopic magnetization $\boldsymbol{M}$. During the magnetization process of permanent magnets, a rising external magnetic field $\boldsymbol{H}$ is applied. The result is an adjustment of atomic magnetic moments, which leads to an enhanced magnetization $\boldsymbol{M}$. This magnetization contributes together with the external field to the magnetic flux density

$$\boldsymbol{B} = \mu_0\,(\boldsymbol{H} + \boldsymbol{M}) = \mu_0\mu\boldsymbol{H}, \tag{2.58}$$

where μ is the relative permeability. At low external fields acting on a material, which has never experienced a magnetic field before, a linear relation

$$\boldsymbol{M} = \chi\boldsymbol{H} \tag{2.59}$$

is observable, but with increasing external field, the magnetization saturates, meaning that χ and μ converges to 0 and 1, respectively (inserting (2.59) into (2.58) shows $\mu = 1+\chi$). If the external field is reduced again, the magnetization $M(H)$ and therewith the flux density $B(H)$ will not follow the initial curve a but curve b, which does not reach the origin. The remaining flux density $B_R(0) = \mu_0 M$ is the remanence field, mentioned above. The oppositely directed external field H_C, which is needed in order to remove the remanence field, is called coercivity. Increase of the oppositely directed field until a second saturation is reached and going back completes the measurement, that exposes the hysteresis loop $b + c$ and the initial magnetization curve a [41]. A schematic of such a hysteresis curve is shown in figure 2.5.
Permanent magnets (magnetically "hard") exhibits a large remanence field, which defines the strength, and a high coercivity, which corresponds to a good stability of the permanent magnet. Therefore curve $b$in the second quadrant is decisive for permanent magnets as it indicates the remanence field and the coercivity. With respect to iron, nickel, cobalt and its alloys (magnetically "soft", because of a small remanence field and coercivity), the initial magnetization curve a is the most important one, as it shows the permeability of a virgin material and its saturation. This material parameter is decisive if the magnetically "soft" material should be deployed to guide magnetic fields, as it is required for magnetic shieldings. The higher the permeability of the material, the more suitable it is for magnetic shieldings. Both materials and its magnetic characteristics are

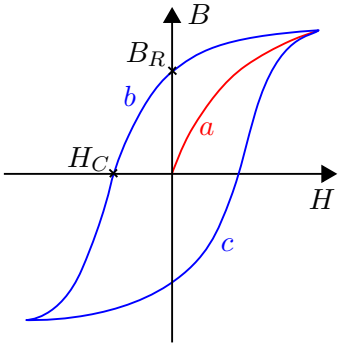

Figure 2.5 – Hysteresis in ferromagnetic materials. a shows the initial curve, b and c the hysteresis loop with its remanence field B_R and coercivity H_C. The slope of the non-linear curve a corresponds to the relative permeability μ.

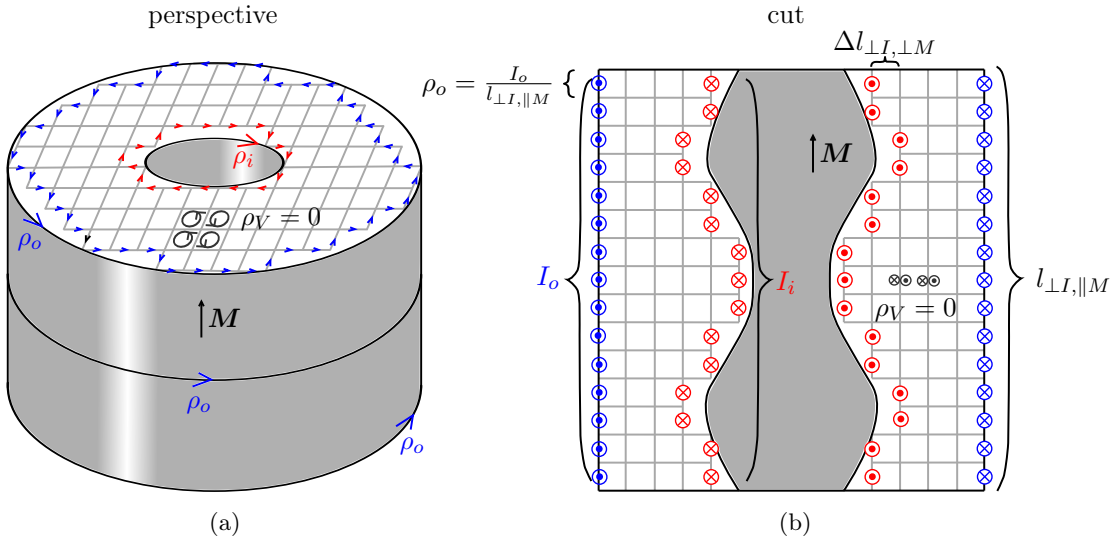

Figure 2.6 – (a) Perspective view of an axially magnetized PMS, which illustrates the origin of the magnetization: Surface currents due to atomic currents.
(b) Corresponding cross section view. The illustration of the shaped inner radius shows, that the surface currents do not occur on length elements, perpendicular to the magnetization. Due to the fact, that the outer surface current is as larger as the inner surface current, the first field integral F_1 and therewith the Larmor angle is always zero for PMSs.

important for this thesis because the solenoid and the shielding will be produced from them.

Having recapitulated the microscopic origin of the magnetic field of permanent magnets, an easy possibility to describe the arising fields, based on electric currents, can be presented. Regarding an axially magnetized permanent magnetic solenoid, as depicted in figure 2.6, the atomic circular currents flow in planes perpendicular to the magnetization. Inside the volume, every atomic current is compensated by neighboring atomic currents. The complete compensation does not occur on surfaces parallel to the magnetization so that surface currents result, indicated as I_o and I_i on the right hand side in figure 2.6. In order to express the current independently from the magnet's length, the surface current density ρ [A/m] is introduced. For a given remanence field, the surface current density is calculated by $B_R = \mu_0 \rho$, which leads, e.g. in the case of NdFeB, to the enormous current density of approximately 1170 kA/m. Figure 2.6 shows that the surface current I_i is not increased by extending the surface without extension of the length $l_{\perp I,\parallel M}$. The reason for this is that the atomic currents do not occur on length elements $\Delta l_{\perp I,\perp M}$, which are perpendicular to the magnetization $\boldsymbol{M}$. This fact will become important if the inner radius is modulated in order to shape the magnetic field. For the easier case of a constant inner and outer radius R_i, R_o along the length L, the permanent magnet's field can be calculated as a superposition of two air coils with opposite current direction and different radii R_i, R_o. With the formula (2.55), given in 2.2.1, the superposition looks like

$$\begin{aligned} B_z(z) = \frac{\mu_0 \rho}{2} \Bigg(& \frac{z + L/2}{\left(R_i^2 + (z + L/2)^2\right)^{1/2}} - \frac{z - L/2}{\left(R_i^2 + (z - L/2)^2\right)^{1/2}} \\ & - \frac{z + L/2}{(R_o^2 + (z + L/2)^2)^{1/2}} + \frac{z - L/2}{(R_o^2 + (z - L/2)^2)^{1/2}} \Bigg), \end{aligned} \tag{2.60}$$

where IN/L has been replaced by the corresponding current density. The longitudinal on-axis field thus depends on the solenoid's dimensions R_i, R_o, L, and surface current density ρ. While the current density only scales the field, the other three parameters provide a variety of field shapes. In figure 2.7 four different field maps are shown as exemple. All curves exhibit a positive peak or plateau, which originates from the inner surface current. These peaks or plateaus are superimposed by the negative and broad field from the outer current, which leads in all cases to undershoots left and right of the positive peak or plateau. For the case of the long solenoid with a small difference between inner and outer radius (red) it even leads to a dip at $z = 0$. The reason is that

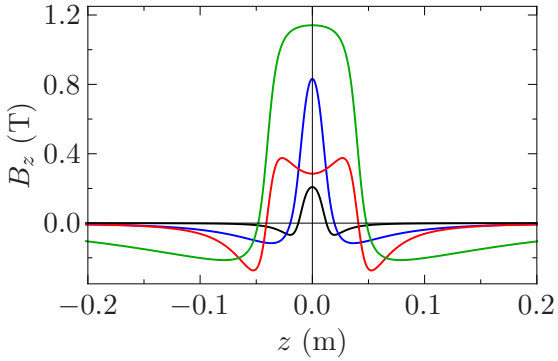

Figure 2.7 – The longitudinal on-axis fields for four different PMS dimensions are shown. The black and the blue curve show magnetic fields of short solenoids. The black curve corresponds to a small outer radius, the blue curve to a large outer radius. Long solenoids induce magnetic fields, shown as red and green curve. Red corresponds to a small, green to a large outer radius.

the field of the inner current almost reached its maximum plateau value of

$$B_{z,i}(z=0) = \frac{\mu_0 \rho}{2} \frac{L}{\sqrt{R_i^2 + L^2/4}} \approx \mu_0 \rho = B_R, \tag{2.61}$$

for $L = 8R_i$, while the negative field of the outer current still has a peaked form. Based on the the field value $B_z(z=0)$ a parameter ϵ can be introduced, which will be used in the following. It directly shows the decrease of $B_{z,i}(z=0)$ generated by the inner current due to superposition with the negative $B_{z,o}(z=0)$ originated by the outer current. Therefore a comparison of $B_z(z=0)$ between the case of an infinite outer radius and a practicable solenoid is made

$$\frac{1-\epsilon}{\sqrt{R_i^2 + L^2/4}} = \frac{1}{\sqrt{R_i^2 + L^2/4}} - \frac{1}{\sqrt{R_o^2 + L^2/4}}, \tag{2.62}$$

which leads to

$$R_o^2 = \frac{L^2/4\left(1-\epsilon^2\right) + R_i^2}{\epsilon^2} \Leftrightarrow \epsilon^2 = \frac{R_i^2 + L^2/4}{R_o^2 + L^2/4}. \tag{2.63}$$

The left expression in (2.63) can be used to substitute R_o with ϵ in $B_z(z, R_i, R_o, L, \rho)$. Characteristics of permanent magnetic solenoids, like focusing strength and emittance growth are proportional to F_2 and F_3 respectively (cf. (2.33) and (2.52)), which depend only on the longitudinal on-axis field. Hence, the systematic investigation of the longitudinal on-axis field $B_z(z, R_i, \epsilon, L, \rho)$, its derivatives and integrals is a crucial part of this thesis.

After this description of PMSs, they finally can be compared to electromagnetic solenoids. The first important advantage is the fact, that PMSs are much more compact and light compared to conventional electromagnetic solenoids. This fact has a universal reason, namely that an annular permanent magnet does not change its maximum field value, if all dimensions are equally reduced (e.g. for a PMS: (2.61), which is analogously valid for the magnetic field induced by the outer currents, does not change its value for a constant ratio R_i/L). If an electromagnetic solenoid is reduced in size, the current density in the coils has to be increased in order to keep the maximal field value constant. At some point, this will lead to insurmountable cooling problems, so that a permanent magnet can always produce higher fields below a certain size.
To name another example, short permanent magnetic quadrupoles (PMQs) exhibit enormous high field gradients [4]. PMQs are already successfully applied [48].
Furthermore PMSs do not require any electrical power. It does not only save energy, but rather makes power supplies and water-/He-cooling systems needless, which is very attractive for in-vacuum designs.
The most important disadvantage is the fact that a PMS is not intrinsically adjustable in focusing strength, as it is the case for an electromagnetic solenoid. This implies some challenges, one has to cope with during the design of a PMS (cf. chapter 3). A second disadvantage is the larger integrated curvature of the longitudinal on-axis field in comparison to the magnetic field of an electromagnetic solenoid (cf. figures 2.7 and 2.4 (b)). The consequence is a larger emittance growth, even for optimized designs as will be shown in the sections 3.1-3.4.

3 Design of a permanent magnetic solenoid

This chapter deals with the development of a permanent magnetic solenoid (PMS). Here the first important step is the identification of the requirements, which result from two experimental set-ups at REGAE, the external injection experiment and the transmission electron microscope (TEM). Having defined the demands, the decision for a permanent magnetic solenoid and against an electro solenoid is explained. Besides the advantages, which lead to the decision, the major disadvantage of a PMS, that it cannot be switched off, yields further challenges. They are briefly described in this section, whereby the most important one — the development of a magnetic shielding — is explicitly discussed in chapter 4. Subsequently, four different designs of a PMS are presented and assessed with respect to the found requirements.

As explained in the introductions about the external injection experiment (cf. 1.2) and the TEM (cf. 1.3), both experiments require a very small transverse beam size on their targets. Concerning the TEM design parameters, a spot size below 10 µm (rms) is foreseen. For the external injection an even smaller spot size below 3 µm (rms) is desired. It is obvious that the presently installed electromagnetic solenoids for the diffraction experiments with a planned spot size of around 100 µm (rms) have to be supplemented by another focusing element in order to realize the two future experiments. At first there are two feasible solutions. One possibility is to install a further solenoid in front of solenoid 4/5 (see 1.1), which has a lower focusing strength than the ones that are already in use at REGAE. The other possibility is to place a solenoid downstream of solenoid 4/5, which will need a focusing strength much larger than the upstream focusing elements. Comparing these two options (in figure reffi:Xrms), one can see that the divergence of the first case is only one fourth of the divergence of the second case.

By means of the rms trace space emittance examined at the focal spot

$$\epsilon_{tr,x} = \sqrt{\langle x^2\rangle\langle x'^2\rangle - \cancel{\langle xx'\rangle^2}} = x_{\mathrm{rms}}x'_{\mathrm{rms}}, \tag{3.1}$$

(the correlation is canceled due to the coincidence of the trace space ellipse's half-axes with the principle axes in the focal spot) it is seen that the focal spot size of the first

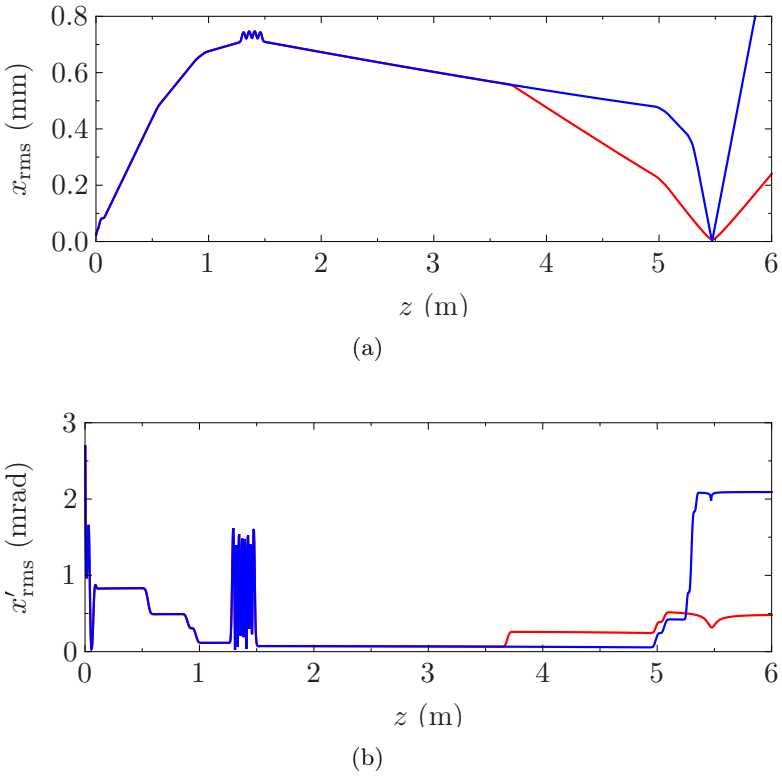

Figure 3.1 – (a) The transverse profile for the design case of the external injection experiment is shown. The red curve results if a weak solenoid is utilized in front of solenoid 4/5, which is positioned at $z = 5\,\mathrm{m}$. The blue curve corresponds to the case with a strong solenoid right before the target. (b) The associated divergences for both cases.

solution will be four times as large as for the second one. For this estimation, similar emittances for both cases were assumed. As it is essential for the external injection to have the smallest possible spot size in order to probe the wake field with a good transverse resolution, the second possibility should be preferred. Regarding the TEM experiment, the same conclusion applies. In order to achieve a large magnification $M = (S - f)/f$ with a reasonable distance to the screen S (see 1.3), the focal length should be as small as possible. Hence the second solution with a strong focusing solenoid is preferable here as well.

Another important requirement is a small emittance growth induced by the solenoid. There are two reasons for this demand with respect to the external injection experiment.

First, as can be seen in formula (3.1), any emittance growth will cause an increased focal spot size, which should be avoided as discussed before. Second, the external injection experiment will be an important experiment in order to demonstrate the possibility of staging laser wakefield accelerators (see 1.2). A proof of principal for staging has to show, that an electron bunch leaves the first gas target with a small enough emittance, which allows it to focus the beam into the following gas target. It would be counterproductive, if the emittance was noticeably enlarged even before it enters the first gas target. In case of the TEM, the necessity of a small emittance growth is clear. As deduced in 2.1.3, emittance growth and the spherical aberrations are closely related and the spherical aberration is a decisive parameter for the TEM's quality.

Due to the decision to use a strong focusing element, placed in between solenoid 4/5 and target, a compact design of the additional solenoid is essential. The longitudinal distance between the rear edge of solenoid 4/5 and the target is only 410 mm. The target chamber, the solenoid and eventually a beam arrival monitor (BAM) have to be installed in this section with the consequence that an electromagnetic solenoid will not be compact enough. To illustrate this fact, REGAE's double electro solenoid is considered. It is an array of two single solenoids with counter-propagating currents, which are already described in more detail in section 2.2.1. Hence, the magnetic on-axis field consists of a positive and a negative bell-shaped peak. In good approximation its focusing strength $1/f_2$ is twice the focusing strength of the single solenoid $1/f_1$, because of the small overlap between the positive and the negative peak. The double solenoid has a value of about $3 \times 10^{-3}\,\mathrm{T}^2\,\mathrm{m}$ for the second field integral F_2 if the maximal current of 9 A is applied. The limitation of the applicable current is given by thermal heating, which can be controlled for currents up to 9 A by the installed water cooling system. Assuming the design beam energy for the external injection experiment of 5.6 MeV, it corresponds to a focusing strength of $1/f_2 = 1.75\,\mathrm{m}^{-1}$. That is only equivalent to 40 % of the focusing strength, assumed in figure 3.1 for the strong focusing case (blue curve), to achieve a spot size of 3 µm (rms). To create the associated magnetic field, 2000 windings of copper wire are used, which corresponds to a wire-length of 1 km and a weight of about 26 kg. More than doubling the focusing strength would most probably lead to dimensions, which are too big to combine the target chamber, the solenoid and the BAM on a length of 410 mm, since the water cooling system of the solenoid has to be enlarged [4].

These considerations yield a demand for a different way to build a strong focusing solenoid. Since permanent magnets exhibit a large remanence field of about $B_R \approx 1.4\,\mathrm{T}$, which results from an enormous surface current density of about $\rho = 1170\,\mathrm{kA/m}$ (compare section 2.2.2), they offer decent properties in order to realize a strong focusing element. Therefore, they will be deployed for the focusing solenoid in front of the target and for the second solenoid behind the target. As mentioned before, the second solenoid

is needed for the TEM experiment and will be equivalent to the front solenoid (compare figure 3.2). In order to emphasize the large surface current density, one can calculate the current on the inner surface of a permanent magnetic solenoid with a length of 41.8 mm, which corresponds to the length of REGAE's single electro solenoid. In this case, the permanent magnetic solenoid exhibits an inner current of about $I_i = 49\,000\,\mathrm{A}$. If this total current was produced by an electro solenoid with a current of 9 A approximately 5400 turns would be needed.

Using permanent magnetic solenoids directly leads to further requirements. Since PMSs do not have an on/off switch and will not be needed for every ongoing experiment at REGAE, e.g. the electron diffraction experiments, the possibility of removing them from the beam is essential. This is feasible, if vacuum suitable PMSs are included into the target chamber and provided with a lifting system of at least 100 mm travel distance. In figure 3.2, the concept of a removable PMS is schematically illustrated for different experiments. However, chapter 4 will show, that this travel is not sufficient in order to

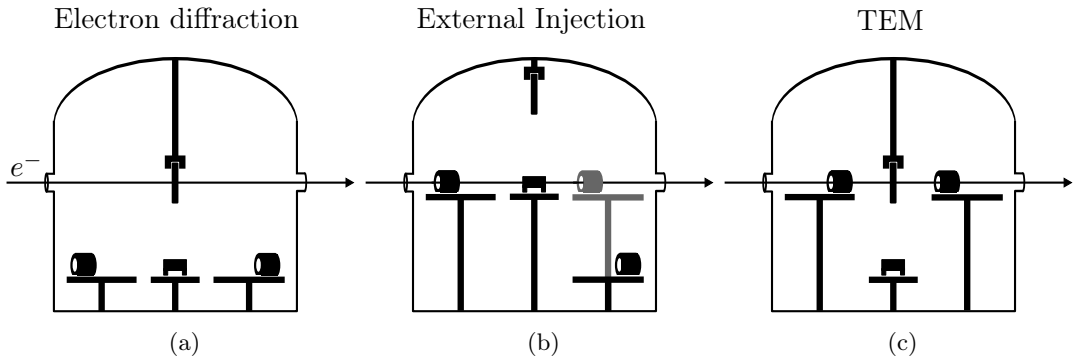

Figure 3.2 – (a) Configuration for the electron diffraction. Both PMSs are not needed, only the manipulator from above in the beam path.
(b) For the external injection the front PMS and the gas target from below are in the beam. The second solenoid could allow a first focusing behind the gas target.
(c) During the TEM experiment, both PMSs from beneath are in the beam. The target is positioned with the top manipulator.

ensure, that the electron beam is not significantly influenced by the fringe fields of the PMSs. Hence, an additional magnetic shielding has to be developed.

The fact, that a PMS does not have an adjustable focusing strength, makes it desirable to embed it movable along the longitudinal axis. As the positioning of focusing elements (not only along the longitudinal axis but especially in the transverse plane) has to be precise on a µm-scale, micropositioning stages are required. Due to their piezo-element based

External Injection	TEM	Resulting requirements
beam size: $< 3\mu m$ (rms)	- beam size: $< 10\mu m$ (rms) - small f for large M	**large focusing strength 1/f**
small emittance growth	small spherical aberrations	**optimized focusing characteristics**
compact and vacuum suitable design, which allows to position two solenoids in the target chamber		**permanent magnetic solenoid**
ensure that the three experiments do not disturb each other (Ext. Inj., TEM, Diffr.)		**magnetic shielding**
- accurate positioning - macroscopic travel in longitudinal ($f_{5.6MeV} \approx 23\,cm$, $f_{3MeV} \approx 8\,cm$) and transverse axes		**weight of the system beneath 1.5 kg**

Table 3.1 – Summary of the requirements for the solenoid. They are defined by the two future experiments at REGAE.

operation, they have a limitation of the load capacity, given with 1.5 kg. As discussed in chapter 4, the solenoid and the magnetic shielding cannot be embedded separately. Thus, both elements and their mechanical connections to the micropositioning stage have to weigh less than 1.5 kg.

The requirements concerning a permanent magnetic solenoid, which are defined by both experiments, the external injection and the TEM, are summarized in table 3.1. With these requirements, different designs for a PMS will be evaluated in the following.

As deduced in chapter 2.1.2, not only an annular permanent magnet with axial magnetization (see figure 2.6) — mostly mentioned in literature [1, 49] when it comes to permanent magnetic lenses — can focus charged particles. But rather every device with a magnetic field, which is cylindrically symmetric and has a longitudinal component $B_z \neq 0$. After examination of the axially magnetized solenoid (set-up 1), a modification in which the focusing performance is optimized by shaping the inner radius (set-up 2) is discussed. A combination of two axially magnetized solenoids (set-up 3) is also assessed with respect to the ratio between focusing strength and emittance growth. In the last section, a promising design approach consisting of two radially magnetized solenoids (set-up 4) is proposed and investigated.

3.1 Axially magnetized solenoid

In section 2.1 the expressions for the focusing strength $1/f$ and the growth of the normalized emittance $\epsilon_{n,rms}$ were derived for solenoids within the thin lens approximation. In this context, two field integrals F_2 and F_3 are defined [50], which are only dependent on the properties of the solenoid and decoupled from beam properties like transverse size, particle's charge or momentum. For repetition, they are shown here:

$$\frac{1}{f} = -\frac{e^2}{4\gamma^2 m^2 v_z^2} \overbrace{\int B_z^2 \mathrm{d}z}^{F_2} \tag{3.2}$$

$$\epsilon_{\mathrm{n,rms}} = \frac{1}{mc} \frac{e^2 R^4}{\sqrt{2}\,48\, p_{z,i}} \underbrace{\int \left(-\frac{B_z B_z''}{2}\right) \mathrm{d}z}_{F_3} \tag{3.3}$$

If one wants to improve the ratio between focusing strength and emittance growth only by the design of the solenoid, the ratio F_2/F_3, referred to as focusing performance below, has to be maximized. With the demand for a minimal F_3 and without consideration of F_2, numerical algorithms would converge to the trivial solution of no magnetic field at all. Thus F_2 has to be kept fixed.

Regarding the integrand of F_3, one can directly see that a magnetic field without any curvature, so to say a perfectly linear focusing element, would lead to a vanishing third field integral. The term "linear" refers to the fact, that $B_z(z)$ consists only of sections with linear slope, which is linked by the series expansion (2.2) to the fact, that $|B_r(r)| = |-rB_z'/2|$ linearly increases with rising r. To give an example, a triangle or trapezoid longitudinal on-axis field would be a perfect field distribution for a focusing element. This is of course unrealistic to reach, as a discontinuity in slopes can only occur at material transitions, but an electron beam has to stay in vacuum. Nevertheless, it is a descriptive example for the following optimization of the field distribution of an axially magnetized solenoid.

As it is already shown in figure 2.7, such a PMS exhibits various types of field distributions $B_z(z, R_i, \epsilon, L, \rho)$, dependent on the solenoid's dimensions. The variables, which are used to describe the solenoid, are illustrated in figure 3.3. Here, a typical field map is shown as well. During this chapter, a surface current density of $\rho = 1.15 \times 10^6\,\mathrm{A/m}$ is assumed. It corresponds to the remanence field $B_R = 1.44\,\mathrm{T}$, which is reached by the magnetic material *Vacodym 745 HR* [51].

In order to assess the dimensions systematically with respect to the criterion F_2/F_3, a numerical program varies the dimensions within reasonable limits and evaluates the value

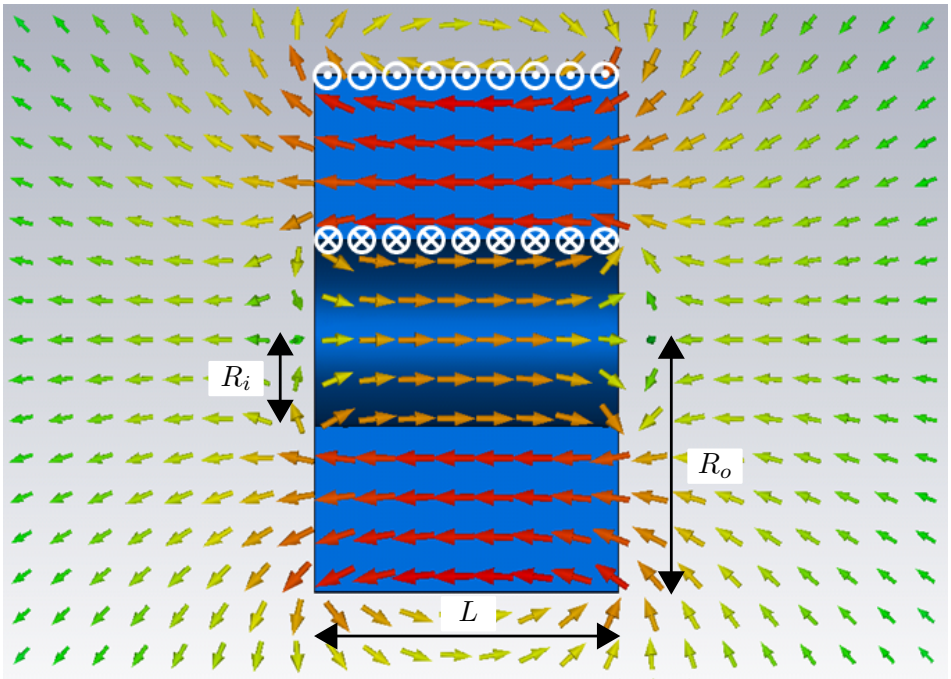

Figure 3.3 – Illustration of an axially magnetized solenoid. The PMS can be described geometrically by the inner radius R_i, the outer radius R_o and its length L. The magnetic field map shows the typical changes of direction at the edges of a PMS (in contrast to the magnetic field of a electromagnetic solenoid). In the following algorithm the longitudinal on-axis field is analytically evaluated by means of the surface currents with Biot-Savart-law

of F_2/F_3 for each parameter set. Thereby, the inner radius R_i and ϵ are freely varied. ϵ is preferred over R_o as parameter to define the solenoid. It directly indicates the decrease of the magnetic field of the inner current, which is caused by the outer current with opposite direction (see (2.63)). The last dimension, the length L, is not freely varied. In every parameter set (R_i, ϵ), L is numerically adapted in a way, that F_2 retains a fixed value required by the experimental set-up. For both experiments, F_2 is set to $7.26 \times 10^{-3}\,\mathrm{T}^2\,\mathrm{m}$ which corresponds to focal lengths of $f_{5.6\mathrm{MeV}} = 229\,\mathrm{mm}$ and $f_{3\mathrm{MeV}} = 76\,\mathrm{mm}$ and leads to the required small focal spot sizes, as already shown in figure 3.1. The longitudinal on-axis field B_z of a PMS, which is needed for the calculation of F_2 and F_3 is given by

the following formula, developed earlier in chapter 2.2.2:

$$B_z(z,L) = \frac{\mu_0 \rho}{2}\left(\frac{z+L/2}{\sqrt{R_i^2+(z+L/2)^2}} - \frac{z-L/2}{\sqrt{R_i^2+(z-L/2)^2}}\right. \tag{3.4}$$

$$\left. - \frac{z+L/2}{\sqrt{\left(L^2/4\,(1-\epsilon^2)+R_i^2\right)/\epsilon^2+(z+L/2)^2}} + \frac{z-L/2}{\sqrt{\left(L^2/4\,(1-\epsilon^2)+R_i^2\right)/\epsilon^2+(z-L/2)^2}}\right),$$

where R_o from equation (2.60) was replaced by the expression given in (2.63). The square of this expression is not analytically integrable, so that the program performs a numerical integration in order to determine the field integrals F_2 and F_3. Derivatives of equation (3.4) are derived analytically. In figure 3.4 the result of this algorithm is shown.

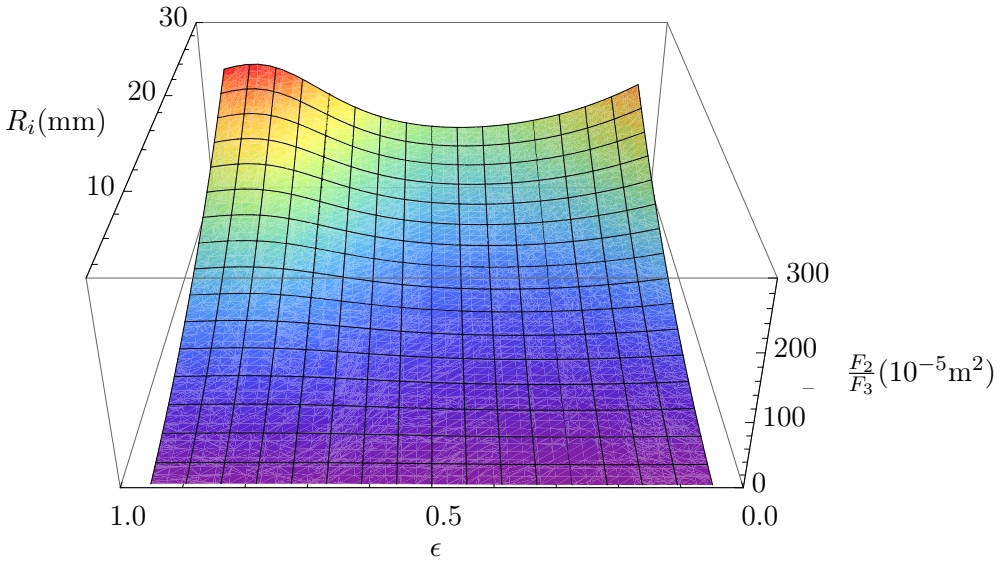

Figure 3.4 – The algorithm, which is explained in the text, calculates the focusing strength for different PMS dimensions. The resulting topography is shown here. The inner radius ranges between 3 mm and 30 mm, ϵ between 0.05 and 0.95. Therewith R_o reaches values between 15 mm for the smallest R_i and large ϵ and 637 mm for the largest R_i and minimal ϵ. The step size of variation is 0.5 mm for ΔR_i and 0.025 for $\Delta\epsilon$.

The most noticeable property of this topography is the increasing value of F_2/F_3 with rising inner radius. It occurs for all values of ϵ and can be explained by lengthening and flattening of the magnetic field, which is associated with an increased inner radius. It can be seen for the two examples $R_i = 5$ mm and $R_i = 10$ mm, of which the magnetic fields are shown in figure 3.5 (a).

If the third field integral is partially integrated, which is justified here because (3.4) is continuously differentiable (attention for the triangle shaped field, mentioned above), one can show that the relation

$$\int -\frac{B_z B_z''}{2} \mathrm{d}z = \int \frac{(B_z')^2}{2} \mathrm{d}z \tag{3.5}$$

holds in case of integration along the complete magnetic field. Regarding $(B_z')^2/2$ as integrand of F_3 , it is obvious that a lengthened magnetic field with smaller slopes leads to an improved focusing performance. In order to illustrate this, the integrand of F_3 after integration by parts is shown in figure 3.5 (b) for the corresponding fields in (a).

The next fact, which catches the reader's eye, is the drop and the subsequent rise of the focusing performance with increasing ϵ. This effect, that is particularly strong for larger R_i, is depicted for $R_i = 30\,\mathrm{mm}$ in figure 3.5 (c), which shows the magnetic field for $\epsilon = 0.1$, 0.5 and 0.9. Basically, the reason for this behavior is similar to the explanation of the increasing focusing performance with rising inner radius. A flattened field, expressed by a large ϵ, results in a lengthening, if a constant focusing strength is assumed. This in turn leads to smaller slopes at the edges, that are moving away from each other. But for $\epsilon < 0.5$, this effect is superimposed by a second process, namely the formation of the undershoots. These undershoots increase the slope and therefore diminish F_2/F_3 until they are readily formed at $\epsilon = 0.5$. For larger ϵ, the process of flattening becomes dominant. It can be easily understood by means of graph (d) in figure 3.5.

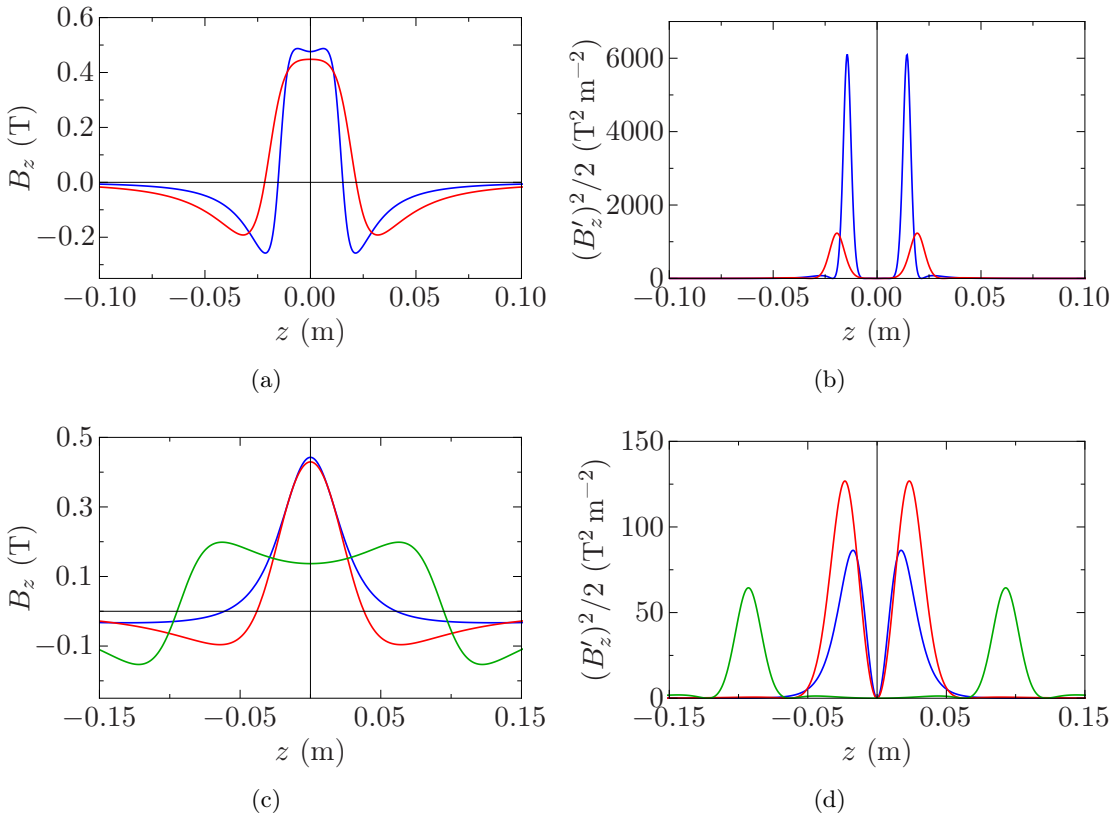

Figure 3.5 – (a) Longitudinal on-axis field for different inner radii $R_i = 5\,\text{mm}$ and $R_i = 10\,\text{mm}$ (blue and red). $\epsilon = 0.65$ is identical for both PMSs; the length are $L/2 = 14.4\,\text{mm}$ and $19.4\,\text{mm}$ for the blue and red curve respectively, which are determined by the condition that the focusing strength is constant for any case.
(b) The corresponding integrands of the field integral F_3, which is proportional to the induced emittance growth, are shown. The advantage of a large inner radius is visible.
(c) Longitudinal on-axis fields for different ϵ but equal inner radius $R_i = 30\,\text{mm}$. The blue curve corresponds to ($\epsilon = 0.1$, $L/2 = 10.9\,\text{mm}$), the red curve to ($\epsilon = 0.5$, $L/2 = 22.3\,\text{mm}$) and the green curve to ($\epsilon = 0.9$, $L/2 = 92.9\,\text{mm}$).
(d) Corresponding integrands of F_3. The rise and subsequent fall of the integral for increasing ϵ is clearly visible

Having understood the general behavior, the considerations have to be complemented by constraints concerning weight and size. Due to the fact, that the whole system has to weigh less than 1.5 kg, the maximal weight of the solenoid is set to 650 g. In chapter 4 it is shown that an effective magnetic shielding for this set-up (basically a cylinder, which is surrounding the PMS and exhibits two holes on its axis for the beam) has to weigh ca. 700 g. This explains the weight limit for the PMS, if a cautious estimation of 150 g for the weight of all mechanical parts is assumed.

A limit for the length arises from the focal length of 76 mm at 3 MeV (defined as length between principal plane of the solenoid and focal point). Subtracting half the length of a sample holder for a liquid cell, which is foreseen with maximal 15 mm, and a small safety distance between target and shielding, the maximal half length of the magnetic shielding is set to 57.5 mm. As will be shown in the section 4.1.4, a magnetic shielding, that is too close to the PMS diminishes the focusing strength in this particular set-up 1 and the focusing performance F_2/F_3 in any set-up. For the first understanding, a qualitative description of this effect is given. Subsequently, a practical quantitative formulation follows, which will be used in chapter 4. The reduction of the focusing strength is caused by a redistribution of the longitudinal magnetic field along the z-axis. A larger part of the magnetic flux is directed through the shielding and a smaller amount of field lines runs through the bore of the PMS. Hence, for moderately long field distributions the large peak of $B_z(z)$ is decreased while the smaller negative undershoots are increased in size. This causes a diminished focusing strength proportional to $F_2 = \int B_z^2 \mathrm{d}z$, where regions with larger absolute values of magnetic flux density have a larger contribution than regions with smaller ones (even if $\int |B_z| \mathrm{d}z$ is identical for both regions). In cases, where the length of the magnetic field is larger, the integral $\int |B_z| \mathrm{d}z$ over the whole set-up is decreased, so that F_2 is diminished anyway.
The decrease in focusing performance $F_2/F3$ is mainly caused by an increased slope at the undershoots if the PMS is too close to the shielding. The closer the distance is, the more abrupt the flux density drops from the field value of the undershoot to zero.

To reduce these effects, the maximal half length of the shielding will be exploited and an upper limit for the half length $(w/2)_{\max}$ of the magnetic field is set. The length of a field can be defined in many different ways. In this case, typical definitions like FWHM or rms of the positive peak are not practical, since the longitudinal distance from the undershoot to the shielding determines the reduction of F_2 and F_2/F_3. And as can be seen in figure 3.5 (c), the ratio between FWHM and the position of the undershoot is not constant for the various field types. That is why the distance from the origin to the position of the undershoot, which is the minimum of the curve, is a practical definition of the half length $w/2$.

The maximum value for $w/2$ is defined by two conditions here. Either it is reached at the point where 20 % of the focusing strength is lost or at the point where a local maximum of F_2/F_3 is reached, depending on which case occurs first. A further lengthening of $w/2$ leads to an improved focusing performance for a PMS without shielding. But it would be either connected with a larger loss of F_2 or overcompensated by the increased slope at the undershoots within a shielding.
For set-up 1, $(w/2)_{\max}$ is reached at 35 mm because the focusing strength falls below 80 % of the initial focusing strength (see section 4.1.4). It must be noted here, that the loss of focusing strength and performance inside a magnetic shielding is not only dependent on the half length of the magnetic field. In the case of moderately long field distributions $w/2 \ll (w/2)_{\max}$ the ratio $B_{z,\max}/B_{z,\min}$ should have an influence for example. So, the utilization of the length of the magnetic field $w/2$ to determine the loss of the focusing strength within a shielding can only be an approximate but necessary orientation.

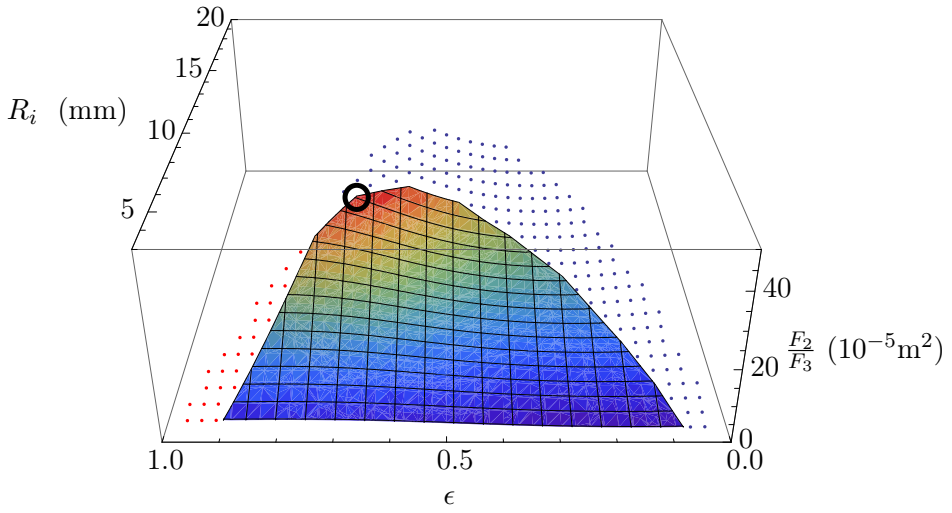

Figure 3.6 – The solutions after application of the weight and size limitation ($m < 0.65\,\mathrm{kg}$, $w/2 < 35\,\mathrm{mm}$) are shown. The colored surface depicts the solutions, where both limitations are fulfilled. The optimal feasible solution is given by the dimensions, which are marked by the black circle ($F_2/F_3 = 32.89 \times 10^{-5}\,\mathrm{m}^2$). The blue points indicates solutions, which fulfill the length but not the weight limitation. For the red points, it is the other way around.

Figure 3.6 shows the possible solutions after application of the weight and size limitations. The specifications of the resulting optimum case, which is marked with a black circle, are given in table 3.2. The blue points show, that there would be better dimensions of a PMS if the weight limitation was repealed. Thus, the optimum is limited by the weight restriction not by the length restriction. In the following, the expression “weight limited” or “length limited” will be used.

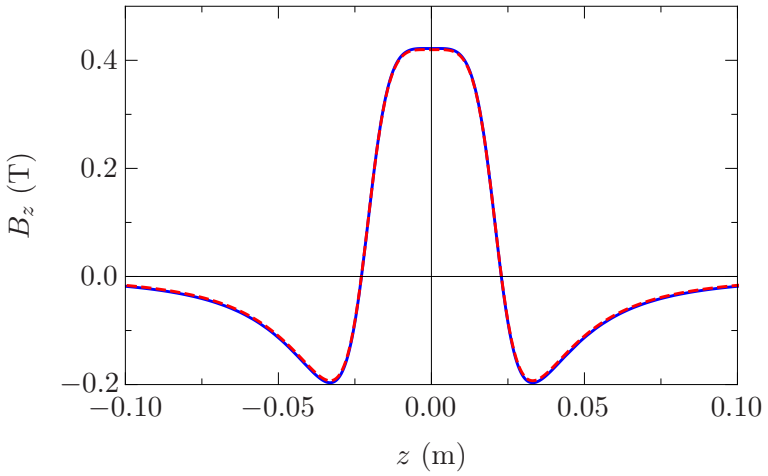

Figure 3.7 – The longitudinal on-axis field, which corresponds to the optimal dimensions from table 3.2, is shown as blue curve. A Finite Element Method (FEM) simulation of the same solenoid (red dashed curve) shows good agreement to the analytical calculation, performed in the algorithm

The magnetic field, corresponding to the optimum dimensions of set-up 1, is shown as blue curve in figure 3.7. The shape of this field and its corresponding focusing performance will be compared to the fields of the following set-ups in order to assess them. The red dashed curve represents the result of a FEM-simulation of the PMS [42], which can be used as cross check for the formulas applied in the algorithm. The shape of the magnetic fields are in good agreement and the deviation between both maximal fields $B_z(0)$ is only 0.5 %.

In order to classify the optimized focusing performance for set-up 1, it can be compared with the focusing performance of the double electromagnetic solenoid, already installed at REGAE. Due to the large focusing strength, the intrinsic undershoots and the short length of the PMS, where the solenoid's non-linearity is worst in general, the focusing performance of the PMS is only 22 % of the focusing performance of the double electromagnetic solenoid ($F_2/F_3 = 144.4 \times 10^{-5}\,\mathrm{m}^2$ at $F_{2,max} = 3 \times 10^{-3}\,\mathrm{T}^2\,\mathrm{m}$).
But considering the emittance growth from equation (3.3), which is not only proportional to the third field integral F_3 but to the fourth power of the transverse beam size as well, the PMS at REGAE will have an advantage over the electromagnetic solenoids. Since one single electromagnetic solenoid, two double solenoids and a buncher cavity, which has focusing properties as well, are ahead of the PMS, the transverse beam size in the PMS is smaller than in the electromagnetic solenoids. For the design parameters of the external injection experiment at a bunch charge of 100 fC, the transverse beam size at the

dimension specifications		focusing properties	
R_i (mm)	10	F_2 ($\mathrm{T^2\,m}$)	7.26×10^{-3}
ϵ	0.675	F_3 ($\mathrm{T^2\,m^{-1}}$)	22.08
R_o (mm)	27.1	F_2/F_3 ($\mathrm{m^2}$)	32.89×10^{-5}
$L/2$ (mm)	20.8		
m (kg)	0.633		

Table 3.2 – Optimal dimensions for set-up 1. The first field integral F_1, which determines the beam rotation φ_L, is not mentioned in the focusing properties, since it is always zero for PMSs

entrance of the PMS is 0.38 mm (rms), while the largest spot size in an electromagnetic solenoid is 0.65 mm (rms). With the formula (2.52), developed in section 2.1.3, it turns out that the normalized emittance growth for the PMS $\epsilon_{\mathrm{n,rms}}^{\mathrm{PMS}} = 3.1 \times 10^{-3}\,\pi\,\mathrm{mm\,mrad}$ is comparable to the one for an electromagnetic solenoid $\epsilon_{\mathrm{n,rms}}^{\mathrm{EMS}} = 2.4 \times 10^{-3}\,\pi\,\mathrm{mm\,mrad}$. Nevertheless, it is useful to try to decrease the emittance growth independently of the beam radius. Because if the beam radius is just 20 % larger than in the simulation (e.g. for higher charge or different beam optics), the emittance growth, induced by the PMS, is three times as large as for the one, induced by the electromagnetic solenoids. Hence, other set-ups are investigated in order to improve the focusing performance.

3.2 Modulation of the inner radius for an axially magnetized solenoid

One possibility to further improve the focusing performance of the first set-up is to change the shape of the solenoid while keeping the dimensions, which are already determined in the previous section, constant. A modulation of the shape will certainly influence the magnetic field and the aim is to decrease the third field integral by minimizing the field's curvature. During this thesis it was not possible to develop an analytical description for this problem, so that again a numerical optimization is chosen. In the following it is explained, how the magnetic field of a cylindrically symmetric permanent magnet, which does not have a rectangular cross section in the r-z-plane, can be calculated.
The resulting expression is used for an evolutionary algorithm, which tries to find an optimized shape of the solenoid by means of the criterion F_2/F_3. As the inner radius has a larger influence on the on-axis magnetic field than the outer radius, a modulation of the inner radius is described here. A modulation of the outer radius can be performed analogously and was investigated as well. The result was less effective than for a modified

inner radius.
If the solenoid is not an annular permanent magnet with rectangular cross section anymore, the field cannot be described as a field of two air coils with different radii R_i, R_o and opposite current direction. This model was used in the first set-up. In the case of a shape, where the inner radius is modulated along the longitudinal direction, as illustrated in figure 2.6, equation (2.54) can be utilized to determine the magnetic field. In order to approximate the integration of (2.54) by a sum, $\mathrm{d}\zeta$ is replaced by a small but not infinitesimal $\Delta\zeta$, so that the sum reads as

$$B_z(z) \approx \frac{\mu_0 \rho}{2} \left(\sum_{j=1}^{n-1} \frac{\left((R_{i,j+1} + R_{i,j})/2\right)^2 \Delta\zeta}{\left[\left(z - (\Delta\zeta(j - 0.5) - L/2)\right)^2 + \left((R_{i,j+1} + R_{i,j})/2\right)^2 \right]^{3/2}} - \frac{z + L/2}{\sqrt{R_o^2 + (z + L/2)^2}} + \frac{z - L/2}{\sqrt{R_o^2 + (z - L/2)^2}} \right), \tag{3.6}$$

where $(R_{i,j+1} + R_{i,j})/2$ denotes the inner radius on the j-th segment of $n - 1$ segments. With this stepwise approximation of a modulated inner radius, the magnetic field and its field integrals are numerically accessible.

To get a rough idea, how a modified inner radius, which yields a larger focusing performance, could look like, the inner ring of the PMS is divided into $n-1 = 9$ large segments along the length L. In each of these segments the inner radius is varied in $k = 10$ coarse steps over a range of $[R_{i,\min}, R_{i,\max}]$, while R_o is kept fixed. If a symmetric magnetic field is assumed ($B_z(z) = B_z(-z)$), $k^{n/2}$ possibilities are evaluated. Similarly to the algorithm of the first set-up, the focusing strength is kept constant for every possibility. Here it is performed by adapting the mean inner radius after variation. The result of this algorithm for a PMS, which has already optimized dimensions, is shown in figure 3.8 (a). This solenoid has indeed an improved focusing performance, but it is only increased by 3 %.

Further improvement can be achieved by smoothing this coarse modulation. For this task, an evolutionary algorithm is used. Because if k and n were increased, the above described algorithm would quickly lead to millions of possibilities. As every variation takes about one second, it would be an excessively time consuming method.
In the evolutionary algorithm, there are much more segments n. For every iteration, the inner radius of each segment is varied by a small and randomly chosen value. After correction of the focusing strength by adjusting the mean inner radius, F_2/F_3 is determined. If the focusing performance is better than in the previous iteration, the actual modulation is taken as starting point for the next iteration. Otherwise, the next iteration starts from the previous modulation. Hence, this process converges to a maximum if the

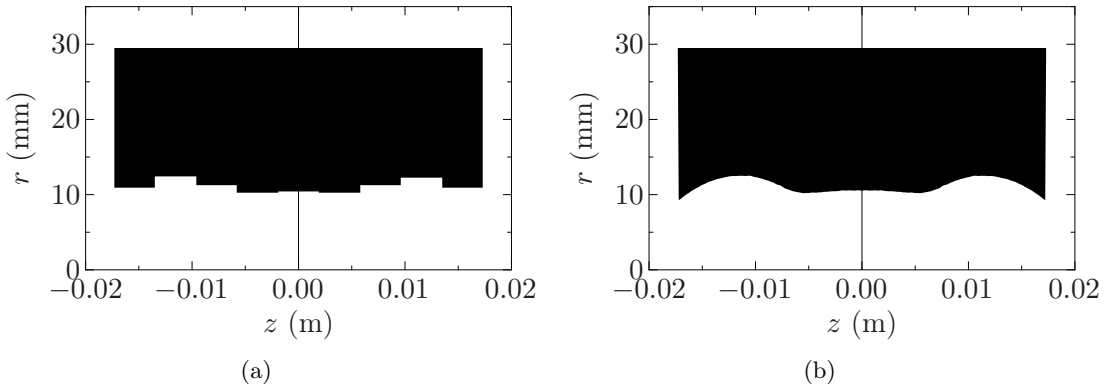

Figure 3.8 – (a) The result of the described algorithm, which yields the best focusing performance within the investigated limits. The length of the PMS is divided into nine parts. For every part, the inner radius is varied between 8 mm and 14 mm in 10 steps. $R_o = 29.5\,\text{mm}$ and $L/2 = 17.3\,\text{mm}$ are fixed. (b) Result of the evolutionary algorithm. The length is divided into 200 parts. The random variation is between $-1\,\mu\text{m}$ and $1\,\mu\text{m}$. Starting point is the modulation in (a).

number of iterations is large enough. In order to exclude that it leads to a local maximum, the starting point is not an arbitrary modulation. The preselected modulation, shown in figure 3.8 (a), is used.
The result of the evolutionary algorithm is illustrated in figure 3.8 (b). A comparison between the corresponding magnetic field and the solution without a modulation of the radius is shown in figure 3.9 (a).
Regarding the magnetic field before and after modulation, one can see, that the magnetic field is mainly modified at its peak. In the area around $z = -10\,\text{mm}$ and $z = 10\,\text{mm}$, one can recognize that the curvature is reduced and approaches a linear behavior. The location of the largest change is comprehensible, since the right curvature is at its maximum (B_z'' is minimal) there. The magnetic field itself is also close to its maximum and hence the integrand of F_3 is maximal. It is illustrated in figure 3.9 (b), where the integrand of F_3 is shown. But even after smoothing the modulation of the inner radius by the evolutionary algorithm, the focusing performance of this set-up is only improved by 4 % compared to the set-up without modulation of the inner radius.
As long as a magnetic field in vacuum is considered, no discontinuity in the slope B_z' can occur. Hence, the presence of a magnetic field, which vanishes in front and behind the solenoid, is inseparably connected to a presence of curvature.

In conclusion, the approach of shaping the inner radius is not as effective as expected for a PMS, with already optimized dimensions. Especially with respect to a much more

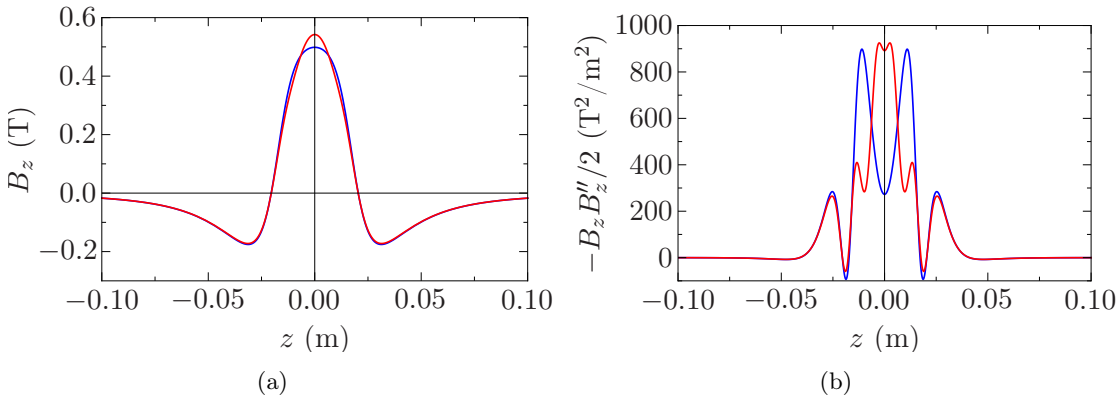

Figure 3.9 – (a) Comparison of the longitudinal on-axis field of a PMS with (red) and without (blue) modulated inner radius. (b) The corresponding integrands of the third field integral show the slight improvement by the modulation.

complex production, a 4 %-improvement by a modulated inner radius does not seem to be worthwhile.

The method of modulating the inner radius has been tested for different dimensions of the PMS, but in any case the improvement of F_2/F_3 does not exceeded 5 %. For example, a PMS with a small inner radius ($R_i = 2.5\,\text{mm}$, $R_o = 44.5\,\text{mm}$, $L = 7.4\,\text{mm}$) was optimized by the same algorithm. Here a larger influence of the inner radius' shape, due to its proximity to the longitudinal axis, could be expected. But even in this case, an improvement of only 2 % regarding F_2/F_3 could be achieved. The small effect of the shaped inner radius leads to the request to investigate further set-ups.

3.3 Two axially magnetized solenoids

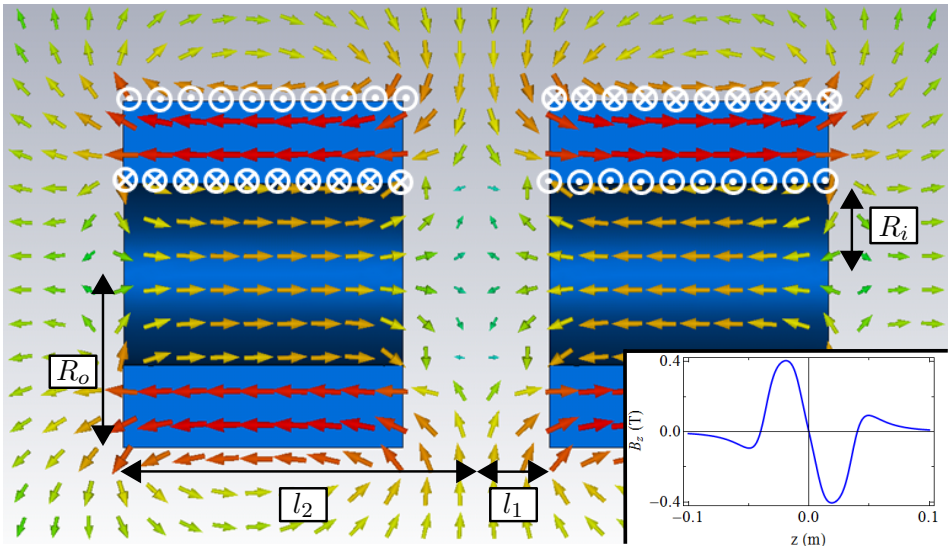

Figure 3.10 – Illustration of two axially magnetized solenoids. The geometry of this set-up is described by the inner radius R_i, the outer radius R_o, l_1 and l_2. By means of the indicated surface currents, the magnetic field can be calculated analytically. The inset shows the longitudinal on-axis field.

Another approach is to use two axially magnetized solenoids, which are magnetized in opposite directions and separated by a distance $2l_1$. A scheme of this set-up, where a typical field distribution is shown and all required variables are introduced, is shown in figure 3.10.
Here, the idea is to create a longer, flattened magnetic field and using less magnetic material at the same time. As already discussed, figure 3.6 shows that set-up 1 is weight limited. Using two PMS instead of one, the weight of magnetic material, which should yield to a certain focusing strength F_2, can be reduced in cases where $L/2 > R_i$ [52]. Additionally, it is obvious, that a set-up with two solenoids can lead to lengthened, flattened fields.
But on the other side, the PMSs may be closer to the magnetic shielding for dimensions with improved focusing performance. So, they would exhibit a lack of focusing strength, due to the reasons described in section 3.1, and may not be a solution anymore. Furthermore, there will be definitely a third slope in-between both solenoids.
All these points are illustrated in an example, shown in the inset of figure 3.10. If the positive effects overweigh the negative effects for suitable dimensions is hard to predict because of the countless different field shapes.

That is why a systematic numerical investigation is performed, as it was already done for set-up 1. The magnetic field can be evaluated as a superposition of two single solenoids and reads as

$$
\begin{aligned}
B_z(z) = \frac{\mu_0 \rho}{2} \Bigg(& \underbrace{\frac{z_+ + L/2}{\left(R_i^2 + (z_+ + L/2)^2\right)^{1/2}} - \frac{z_+ - L/2}{\left(R_i^2 + (z_+ - L/2)^2\right)^{1/2}}}_{\text{left sol.}} \\
& \underbrace{- \frac{z_+ + L/2}{(R_o^2 + (z_+ + L/2)^2)^{1/2}} + \frac{z_+ - L/2}{(R_o^2 + (z_+ - L/2)^2)^{1/2}}}_{\text{left sol.}} \\
& \underbrace{- \frac{z_- + L/2}{\left(R_i^2 + (z_- + L/2)^2\right)^{1/2}} + \frac{z_- - L/2}{\left(R_i^2 + (z_- - L/2)^2\right)^{1/2}}}_{\text{right sol.}} \\
& \underbrace{+ \frac{z_- + L/2}{(R_o^2 + (z_- + L/2)^2)^{1/2}} - \frac{z_- - L/2}{(R_o^2 + (z_- - L/2)^2)^{1/2}}}_{\text{right sol.}} \Bigg),
\end{aligned}
\tag{3.7}
$$

where $z_\pm = z \pm (l_2 + l_1)/2$ indicates a shift in negative or positive z-direction, respectively. With the definitions, shown in figure 3.10, $L/2$ has to be replaced by $(l_2 - l_1)/2$ and R_o by the expression given in (2.63), because the calculations are again carried out with ϵ instead of R_o.

The algorithm, which leads to the results presented in figure 3.11, is analogous to the one performed for set-up 1. Two PMS, that are identical in their dimensions, can be described with four parameters. Thus, three parameters R_i, ϵ, l_1 are freely varied. The parameter l_2 is numerically determined with the constraint that the focusing strength stays constant for every parameter set (R_i, ϵ, l_1). Due to the three free parameters, the results are presented in four dimensional plots. The three space dimensions indicate the solenoid's parameters, while a color scale serves as fourth dimension and shows F_2/F_3. Here, the constraints concerning weight and size of the set-up are directly applied. The maximal weight of the solenoids is again set to 650 g while the limit for the length of the magnetic field $(w/2)_{\max}$ is determined to 50 mm. Allowing a larger $w/2$ would lead to focusing strength-losses larger than 15 % if the necessary magnetic shielding is taken into account (cf. section 3.1).

The possible solutions which fulfill both constraints are shown as colored squares. Additionally, points which fulfill the weight constraint but exceed the length constraint are represented as black squares. With respect to the solutions, where only the set-ups that are exceeding the weight limit are disregarded (combination of colored and black squares), the optimal dimensions are marked with a blue cross.
These dimensions would lead to a focusing performance of $F_2/F_3 = 41.45 \times 10^{-5}\,\mathrm{m}^2$, which is indeed 26 % better than the result from set-up 1 and the best result achieved so far.

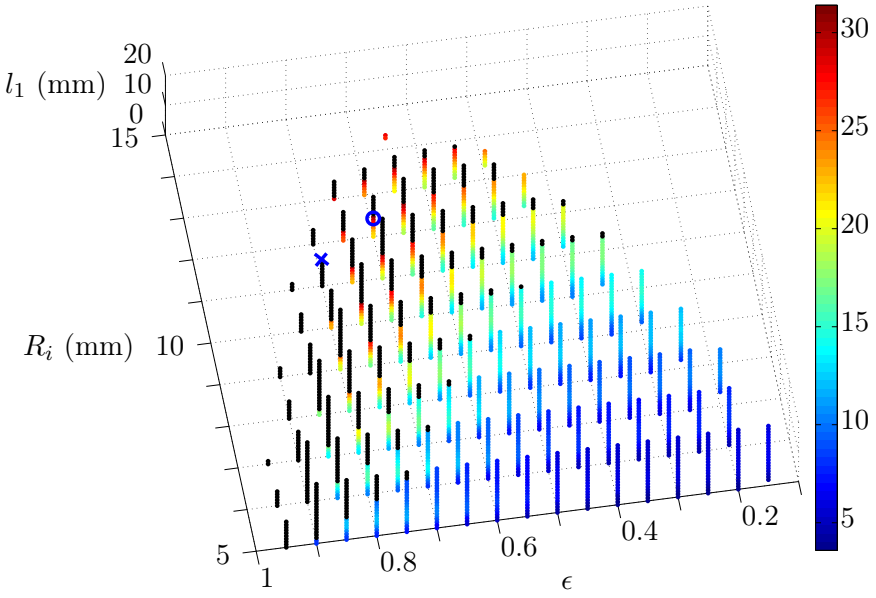

Figure 3.11 – The focusing performance for different dimensions of set-up 3 are shown. ϵ, R_i and l_1 are scanned and depicted as the three space dimensions (l_2 is not freely varied but determined by the constraint $F_2 = \text{const.}$). The corresponding focusing performance is shown as color of the dots. The colored dots indicate the solutions, which fulfill the weight and the length limitation. The dimensions of the black dots fulfill the weight limit but the length limit is neglected here.

The corresponding longitudinal on-axis magnetic field is shown together with the optimal field from set-up 1 in figure 3.12 (a). Figure 3.12 (b) depicts the associated integrands of the third field integral and reveals the reason for the improvement over set-up 1.
The lengthened magnetic field, which is induced by the same amount of magnetic material and exhibits the same focusing strength, shows much smaller slopes on both outer edges (the squared maximum slope of set-up 2 is approximately two times smaller than the one of set-up 1). It even overcompensates the additional slope in-between the solenoids, so that F_3 is finally reduced.

Hence, in general the use of two axially magnetized solenoids can lead to smaller emittance growths than utilizing a single solenoid, if a constraint concerning weight is given. But in the special case, where the length of the magnetic field is limited due to the fact that it has to "fit" inside a magnetic shielding, the possible solutions are further restricted (only the colored squares in figure 3.11) and the optimal dimensions are marked with a

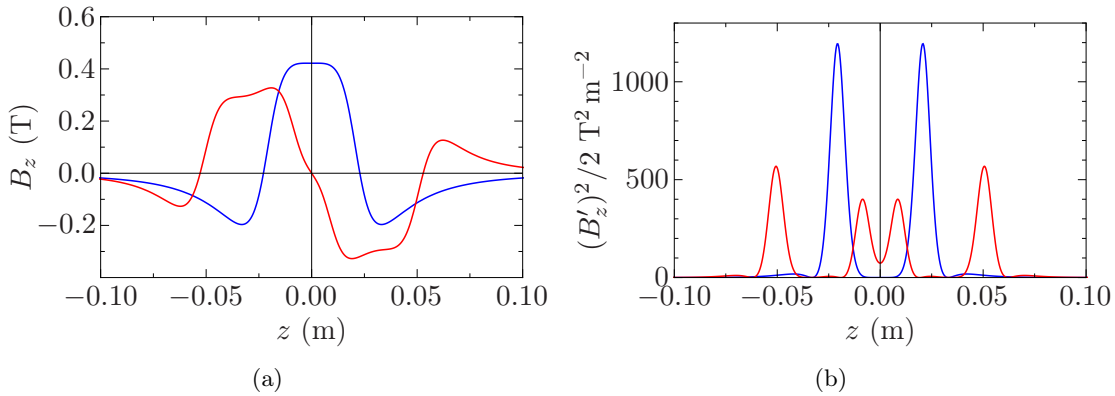

(a) (b)

Figure 3.12 – (a) Comparison of the longitudinal on-axis field of the optimized set-up 3 (red) and the optimum for set-up 1 (blue). For both set-ups, only the weight restriction is taken into account. Figure (b) shows the corresponding integrands of F_3. A comparison of the integrals reveals that two PMS can have a better focusing performance than one, if a weight limitation is considered.

blue circle. The corresponding field is already shown in the inset of figure 3.10.
The specifications of this optimum for set-up 3 are given in table 3.3. The given weight below 650 g shows that the concept of saving weight was successful. Set-up 3 is not weight limited anymore but length limited. The length limitation however does not allow to use the advantages over set-up 1, which are illustrated in figure 3.12 (b).

Finally set-up 3 is 5 % worse than set-up 1 with respect to the focusing performance, so that it does not provide an improvement for the particular PMS at REGAE. In the next section set-up 4, containing of two radially magnetized solenoids, is introduced and will show the desired improvement over set-up 1 with respect to its focusing performance.

dimension specifications		focusing properties	
R_i (mm)	12	F_2 (T^2 m)	7.26×10^{-3}
ϵ	0.7	F_3 (T^2 m^{-1})	23.12
R_o (mm)	22.7	F_2/F_3 (m^2)	31.4×10^{-5}
l_1 (mm)	6.7		
l_2 (mm)	35.8		
m (kg)	0.516		

Table 3.3 – Optimal dimensions for set-up 3. The weight far below 650 g clearly shows that this set-up is length limited and not weight limited like set-up 1.

3.4 Pair of radially magnetized solenoids

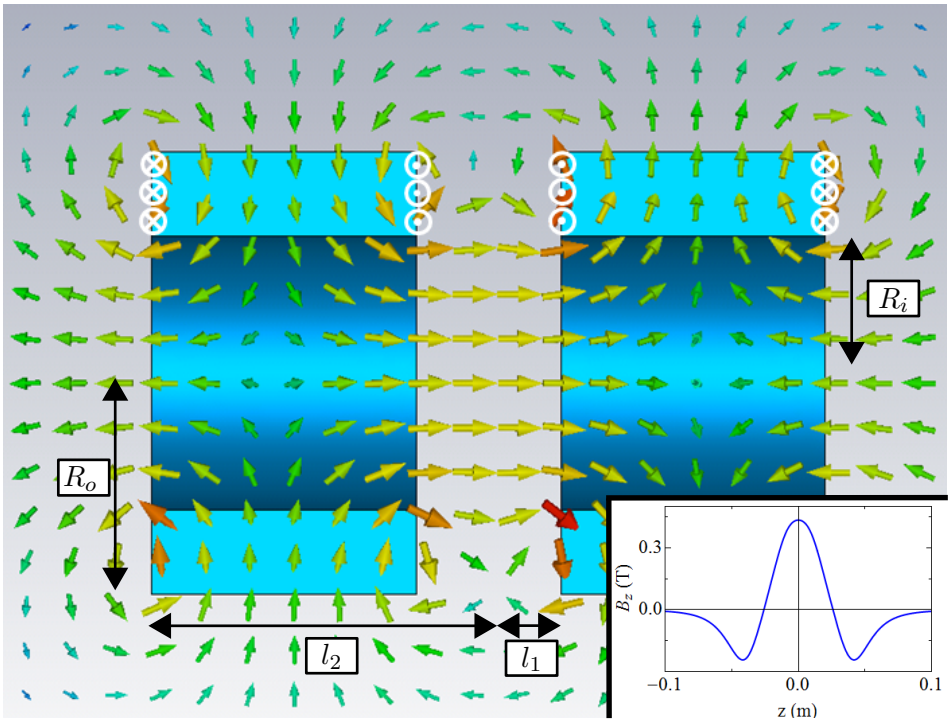

Figure 3.13 – Illustration of two radially magnetized solenoids. The description of the geometry is analogue to set-up 3. By means of the indicated surface currents, the magnetic field can be calculated analytically. Regarding the course of the magnetic field lines, one can see that set-up 4 mimics the field distribution of set-up 1.

The last approach, which is presented in this thesis, is to utilize two radially magnetized annular permanent magnets in order to generate a solenoidal field.
As for the other set-ups, a scheme of set-up 4 is shown in figure 3.13. It illustrates a typical field distribution and defines all variables that are used to describe the dimensions of this set-up.
Regarding both, the 2D-magnetic field in the y-z-plane and the longitudinal on-axis field along the z-axis (shown in the inset), it is noticeable that this set-up mimics the magnetic field of set-up 1, which is mostly mentioned in electron optics literature [1, 49, 53]. Mimicking the magnetic field of the single axially magnetized PMS with two radially magnetized solenoids allows for a larger influence on the field shape since a third free parameter, the distance $d = 2l_1$ between both solenoids, is introduced.
Furthermore, the idea to save weight with two instead of one solenoid, which was men-

tioned for set-up 3, should be valid here as well. But in contrast to set-up 3, using two radially magnetized solenoids is not connected with an additional slope in-between them (cf. figure 3.12, figure 3.15).
Last but not least set-up 4 exhibits two important advantages with respect to its magnetic shielding. First, the flux density in-between the two solenoids is almost not influenced by a surrounding shielding. As consequence, the necessary magnetic shielding does not decrease the focusing strength but even increases it by redistributing the undershoots while leaving the positive peak barely unchanged (cf. section 4.2.2). The opposite was true for set-up 1-3.
Hence, the length limitation $(w/2)_{\max}$ is not set at the point where 15 % of the focusing strength is lost in presence of a shielding (because it does not occur), but where a local maximum of the focusing performance emerges.
As explained before for set-up 1, further lengthening of $w/2$ leads to an improved focusing performance for a PMS without shielding, but it would be overcompensated by an increased slope at the undershoots within a shielding. Moreover, the leaking fields, which are surrounding the solenoids, are not that distinct as for the previous set-ups. In consequence less shielding material is required. This fact will be described in chapter 4.
Again a description of the magnetic field for set-up 4, using the model of surface currents, is developed. With these magnetic fields, a computer based scan of the dimensions can lead to the optimal dimensions with respect to the focusing performance.
Figure 3.13 illustrates that the current sheets are located on different surfaces than it was the case for the other set-ups. With the explanation given in section 2.2.2 it is clear that the surface currents for radially magnetized solenoids do not occur on the inner and outer radius but on its front and rear surface. The resulting magnetic field can be approximated by a superposition of many magnetic fields, all induced by single current loops on the front and rear surface with different radii. With the formula for the magnetic field of a current loop 2.53, the superposition can be written as:

$$B_z(z) = \sum_k \left(\begin{array}{l} \left. -\dfrac{\mu_0 I R_k^2}{2\left((z+l_2)^2+R_k^2\right)^{3/2}} + \dfrac{\mu_0 I R_k^2}{2\left((z+l_1)^2+R_k^2\right)^{3/2}} \right\} \text{left sol.} \\ \left. +\dfrac{\mu_0 I R_k^2}{2\left((z-l_1)^2+R_k^2\right)^{3/2}} - \dfrac{\mu_0 I R_k^2}{2\left((z-l_2)^2+R_k^2\right)^{3/2}} \right\} \text{right sol.,} \end{array} \right. \tag{3.8}$$

where the given summation of R_k is an abbreviation and is defined as follows

$$\sum_k R_k = \sum_{k=1}^{s} R_i + \frac{R_o - R_i}{s-1}\,(k-1)\,. \tag{3.9}$$

The total current of course has to be divided into s parts, so that the current I for every loop is given by

$$I = \frac{I_{tot}}{s} = \frac{\rho \cdot l_{\perp I,\parallel M}}{s} = \frac{\rho(R_o - R_i)}{s}. \tag{3.10}$$

Instead of the summation over many current loops an integration of equation (2.54) over R would have been possible as well. But for the numerical calculation there is no difference noticeable.
Following the procedure as before, the parameter ϵ is used, which is defined by equation (2.63) ($L/2$ has to be replaced by $(l_2 - l_1)/2$ here).

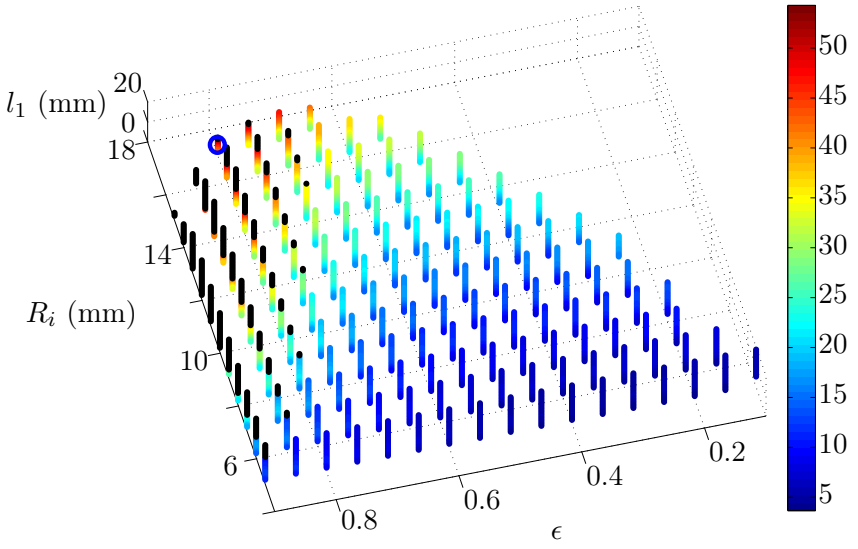

Figure 3.14 – Dimension scan for set-up 4. R_i, ϵ and l_1 are freely varied, while l_2 is used to keep the focusing strength constant. The colored points are solutions which fulfill the length and the weight criterion. The color indicates the focusing performance. Black points are solutions that are beneath the weight limit but above the length limit. They partly have higher focusing performances. Thus, set-up 4 is length limited not weight limited.

The results are analogously to set-up 3 visualized as a four dimensional plot in figure 3.14, where the color of the points serves as fourth dimension and indicates the focusing performance. The weight and length restriction are already applied.
As mentioned above, the maximum length is set at the point, where the maximal focusing performance for the set-up inside a magnetic shielding is reached. FEM-simulations, presented in the next chapter, yield the value $(w/2)_{\max} = 45\,\mathrm{mm}$. The best dimensions

dimension specifications		focusing properties	
R_i (mm)	17	F_2 ($\mathrm{T^2\,m}$)	7.26×10^{-3}
ϵ	0.8	F_3 ($\mathrm{T^2\,m^{-1}}$)	13.4
R_o (mm)	25.4	F_2/F_3 ($\mathrm{m^2}$)	54.3×10^{-5}
l_1 (mm)	7.8		
l_2 (mm)	44.8		
m (kg)	0.628		

Table 3.4 – Optimal dimensions for set-up 4.

are marked with a blue circle. They are documented in table 3.4 and result in a focusing performance of $F_2/F_3 = 54.3 \times 10^{-5}\,\mathrm{m^2}$. This result is 65 % better than the result from set-up 1 concerning focusing performance.
The comparison of the optimal magnetic fields and the corresponding integrands of F_3 for set-up 1 and set-up 4 is shown in figure 3.15 (a), (b). It exhibits the advantages of set-up 4, which were claimed above in this section. Indeed two radially magnetized solenoids can induce a magnetic field, which mimics the magnetic field from set-up 1. Set-up 4 allows to create a lengthened magnetic field, which provides the needed focusing strength, with less magnetic material. Therefore the peaks in the integrand of F_3 are drastically reduced in size. Due to its beneficial behavior inside a magnetic shielding, the length limitation does not restrict the possible solutions as strong as it was the case for set-up 3. Furthermore set-up 4 does not exhibit a third slope in-between both solenoids, which diminished F_2/F_3 in set-up 3.

Hence, set-up 4 provides by far the best result achieved within these investigations. It allows for a 65 % smaller emittance growth, if one compares it to a common PMS (set-up 1) with already optimized dimensions. A reduction of the induced emittance growth by 65 % is an improvement, which is definitely worthwhile to be implemented at REGAE. But it remains to show, that set-up 4 can be magnetically shielded such that the three ongoing experiments at REGAE do not disturb each other. The investigations on this topic are shown in the following chapter.

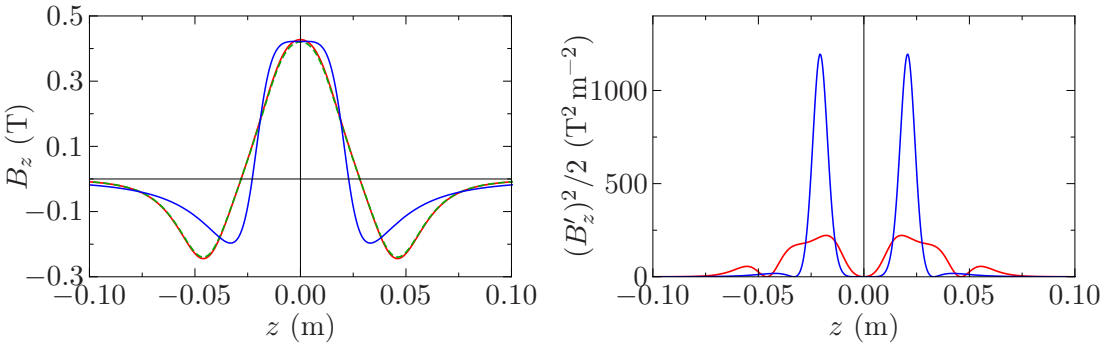

Figure 3.15 – (a) Comparison of the longitudinal on-axis field of the optimized set-up 4 (red) and the optimum for set-up 1 (blue). The smaller slopes of set-up 4 are recognizable. The green dashed curve is obtained by a FEM simulation in order to cross-check the analytical calculations.
(b) The corresponding integrands of F_3, which clearly show the advantageous behavior of set-up 4.

4 Development of a magnetic shielding

As already mentioned in the previous chapter, the future target chamber at REGAE has to be designed in a way, that it can host three different experiments, namely the electron diffraction, the external injection and the TEM experiment. Since every experiment requires a different configuration of the two permanent magnetic solenoids (PMS) close to the target, a lifting system for both PMSs and the target is planned.
In figure 3.2 it is schematically shown, how the lifting system can meet the requirements for all three experiments. In cases where one or two of the PMSs are not needed for the ongoing experiment, it has to be assured that the leaking magnetic fields from the vertically removed PMSs only deflect the electron beam in tolerable limits.
In the present chapter, it is investigated, if this is feasible for the two most promising PMS designs — set-up 1 and set-up 4 — introduced in chapter 3. The following considerations concerning set-up 1 should also be valid for set-up 2. It is shown for these set-ups, that a vertical travel of 100 mm is not sufficient. It is the minimal travel foreseen and therefore assumed in the following. Any larger travel will lead to smaller deflections.
Due to mechanical stability and the wish to keep the vacuum chamber as small as possible, the travel cannot be increased arbitrarily. Thus, a magnetic shielding has to be developed. Furthermore, it is important that the two PMSs do not exert magnetic forces on each other. It would lead to forces along the z-direction, which are not acceptable for the piezo-based micropositioning systems. In section 4.1 it is shown, that this leads to the requirement of a magnetic shielding, which surrounds the PMS and not the electron beam. To avoid longitudinal forces, the shielding and the PMS should also not move relatively to each other.
As consequence, shielding, PMS and their mechanical connections to the micropositioning stage have to weigh less than 1.5 kg, which is the maximal load capacity of the stage. The design of such a light weight magnetic shielding requires some special measures that are documented for set-up 1 and set-up 4 in section 4.1 and 4.2 respectively.

4.1 Magnetic shielding of an axially magnetized solenoid

In this section, magnetic stray fields of set-up 1 are under investigation. Finite element method (FEM) simulations are performed, in order to evaluate them. In cases, where the geometry exhibits a rotational symmetry, 2D FEM simulations are sufficient. They

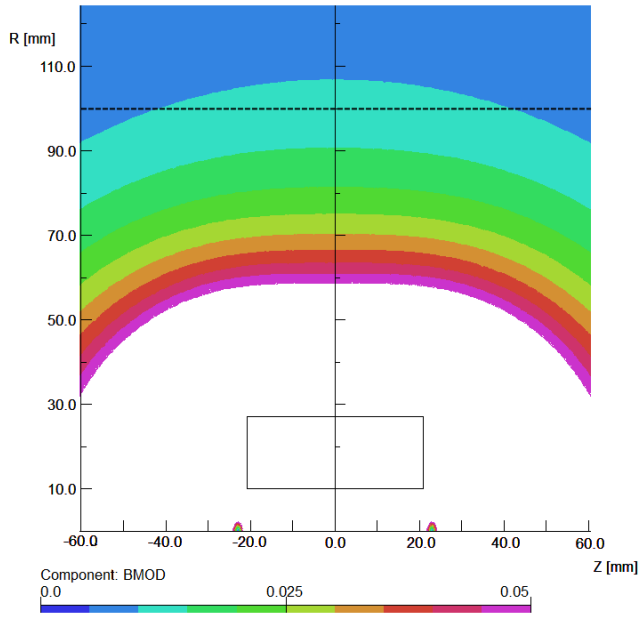

Figure 4.1 – 2D FEM simulation of set-up 1. The colors indicate the magnitude of the magnetic field. The unit of the color scale values is Tesla. White regions exhibit magnetic fields larger than 50 mT.

are executed in the Opera-2D software [42].
Figure 4.1 shows a simulation result of set-up 1 without any magnetic shielding. Here, the magnitude of the magnetic field $B := |\boldsymbol{B}|$ within the r-z-plane (in the following regarded as the upper y-z-plane) is depicted. One can recognize the strong decay with increasing distance from the magnet, which is typical for permanent magnetic solenoids. Figure 4.2 (a) shows a line-out of B_y along the dashed line. But despite this behavior, the magnetic field along the dashed line still significantly deflects an electron beam, moving on this path.
With this magnetic field, which is perpendicular to the beam direction, and the relativistic

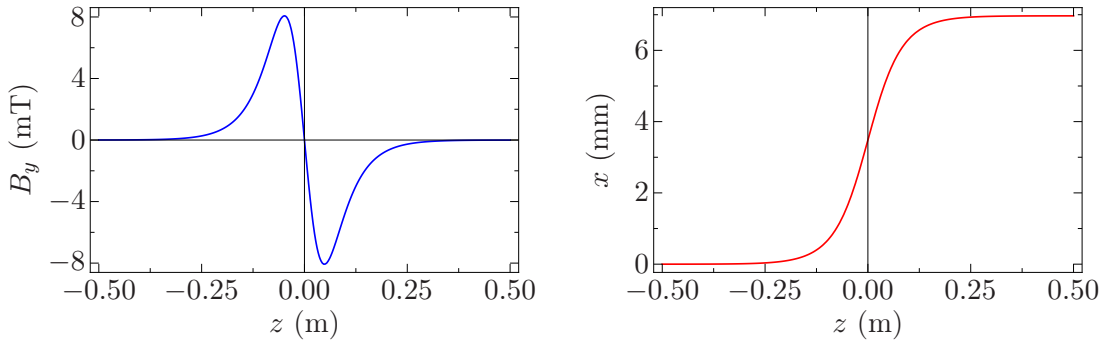

(a) (b)

Figure 4.2 – (a) Line-out of B_y along the dashed line in figure 4.1
(b) The deflection of an electron beam with a mean beam energy of 5.6 MeV caused by the magnetic field shown in (a).

Lorentz force equation, one can easily calculate the deflection of the electrons:

$$\dot{p}_x = e v_z B_y \tag{4.1}$$

$$\gamma m v_x(z) = \int_{-\infty}^{z} e B_y(\tilde{z}) \mathrm{d}\tilde{z} \tag{4.2}$$

$$x(z) = \frac{e}{\gamma m \beta c} \int_{-\infty}^{z} \int_{-\infty}^{\tilde{z}} B_y(\hat{z}) \mathrm{d}\hat{z} \mathrm{d}\tilde{z}, \tag{4.3}$$

whereby a constant longitudinal velocity $v_z = \beta c$ and an initial velocity without transversal component is assumed.
The result of this calculation is shown in figure 4.2 (b). It turns out that the deflection of an electron beam with $\gamma = 12$ is approximately 7 mm. Although it is a static parallel offset, such a deflection is certainly not acceptable for any experiment and has to be reduced by utilizing a magnetic shielding.

At first glance, there are several different means to realize a magnetic shielding. Since the micropositioning stage of the PMS is limited in the load capacity by 1.5 kg and typical magnetic shieldings require a large amount of a high-permeable material, a reasonable idea is to decouple the shielding from the PMS or rather from its stage.
Here, one possibility is to shield the electron beam instead of the PMS. It could be realized by a tube, which is mounted on the lifting system (not on the micropositioning stage) and is screening the electron beam path as long as possible inside the target chamber.
This possibility is illustrated in figure 4.3 (a). The effectiveness of this solution is investigated with the 3D FEM software CST EM Studio [54], since the geometry is not

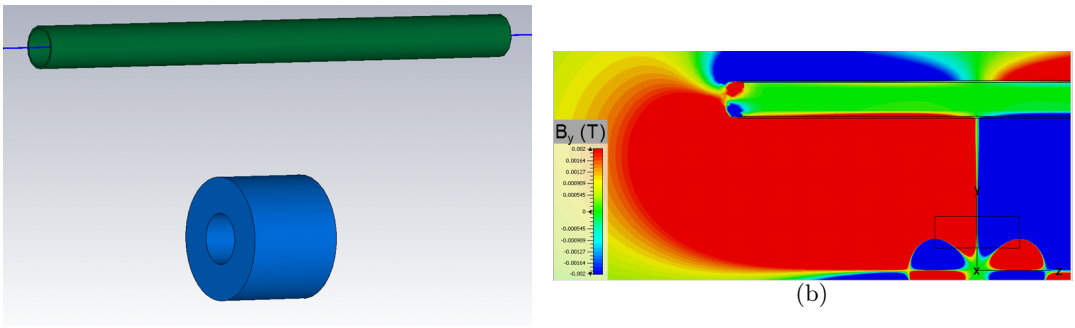

(a) (b)

Figure 4.3 – (a) A scheme, that shows how the electron beam could be shielded by a tube. In this case the weight can weigh above 0.7 kg
(b) A cross section in the y-z-plane of a 3D FEM simulation.

cylindrically symmetric anymore. The simulation reveals two problems of this solution. First, the magnetic field is not sufficiently shielded at the ends of the tube, which can be seen in 4.3 (b). Such a behavior is typical for non-closed shieldings in which the flux is collected and guided but leaks finally out at the open ends. Although the field is properly shielded within the tube, the peaks of the field at the ends deflect the electrons such, that they are parallel displaced by at least 5 mm.
Second and even more important, this possibility does not avoid, that the two PMSs inside the target chamber exert magnetic forces on each other. The magneto-static solver of CST EM Studio includes magnetic force calculations. For the TEM configuration, where both solenoids have a longitudinal distance of $2f_{3\,\mathrm{MeV}} \approx 160$ mm from each other, longitudinal forces up to 6.8 N are present. These forces act on the micropositioning stages, which are only designed to withstand longitudinal forces smaller than 3 N. Hence, this solution is not practicable at REGAE.

A second possibility is to shield the PMS by surrounding it with a long cylinder, like it is shown in figure 4.4. This cylinder could be mounted onto the lifting system so that there are no weight limitations. The PMS would move inside this magnetic shielding in order to reach the longitudinal positions for the external injection and the TEM experiment. Therefore the micropositioning stage, which is situated outside of the shielding, is mechanically connected to the PMS by a rod for example.
Simulations with EM Studio have shown, that the required slit on the bottom side of the shielding and the holes for the electron beam barely influence the shielding qualities.
Due to the fact that a large amount of highly permeable material can be used, electron deflections smaller than 100 µm are easily achieved. Furthermore the two PMSs inside the target chamber do not “magnetically see” each other, so that there are no magnetic

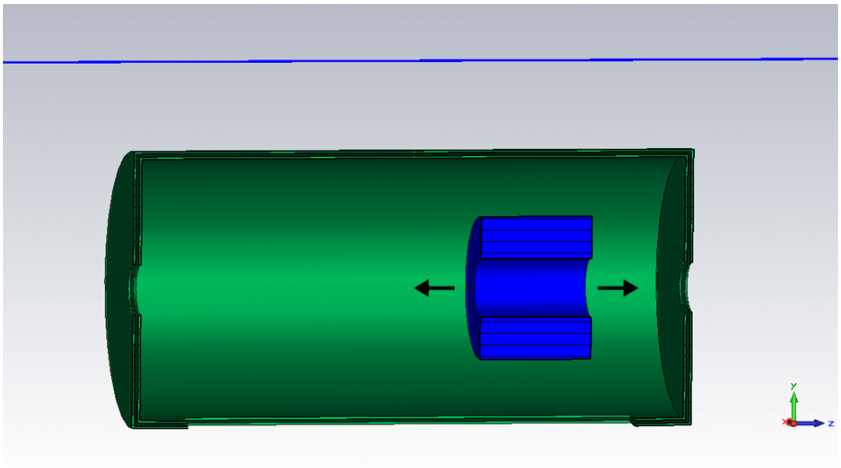

Figure 4.4 – Schematic of the concept to shield the PMS with a cylinder, which is not connected to the micropositioning stage. In this case the PMS moves inside the shielding.

forces between them. But on the other hand there are magnetic forces between the PMS and its shielding, if the PMS is in an asymmetrical position like it is illustrated in figure 4.4.
The magneto-static simulations have shown forces of about 25 N on the PMS at the closest positions to the shielding. These longitudinal forces again act on the micropositioning stage and are therefore an exclusion criterion for this solution.

Hence, the PMS as well as the magnetic shielding has to be positioned on the micropositioning system with the consequence that the whole system has to weigh less than 1.5 kg. After subtraction of the weight of the PMS (approximately 650 g) and the weight for a holding structure (estimated with 150 g), a maximal weight of 700 g remains for the magnetic shielding.
This weight limitation in combination with the high magnetic flux density — the white region in figure 4.1 indicates flux densities, which are at least three orders of magnitude larger than the earth magnetic field exhibits — which has to be shielded, requires an optimized design of the shielding.
There are three major parameters, which describe a magnetic shielding and should be optimized. The first parameter is the utilized material, the second parameter is the shape or thickness modulation along the shielding and the third parameter are the dimensions of the shielding. All of them have a large influence on the relative permeability μ inside the shielding, which is decisive for the shielding behavior.

4.1.1 Suitable materials

As already mentioned in 2.2.2 magnetically "soft" materials with large relative permeabilities μ are most suitable for magnetic shieldings, since shielding materials are meant to redirect the magnetic flux from the shielded volume into the material.
Mu-metal, an alloy of 77 % nickel, 15 % iron and smaller parts of copper, molybdenum, manganese and silcon, exhibits a very large relative permeability $\mu_{\mathrm{Mu}} = 250000$, so that it is often used for magnetic shieldings [55]. But it also shows a disadvantage, namely the small saturation flux density of $B_S = 0.8\,\mathrm{T}$. At this point and above, the flux density inside the *Mu-metal* increases only with $B(H) = \mu_0 H$. This means that the relative permeability drastically drops for large external fields.
VacoFlux, consisting of 49 % cobalt, 49 % iron and 2 % vanadium, exhibits smaller relative permeabilities up to $\mu_{\mathrm{Vaco}} = 13000$ but the largest known saturation flux density of $B_{\mathrm{S,Vaco}} = 2.35\,\mathrm{T}$ [56]. Therefore it is particularly useful for very large external magnetic fields. The underlying $B(H)$ and $\mu(B)$ curves are shown in figure 4.5, which additionally displays the behavior of magnetic iron (it will become important for the shielding of set-up 4).

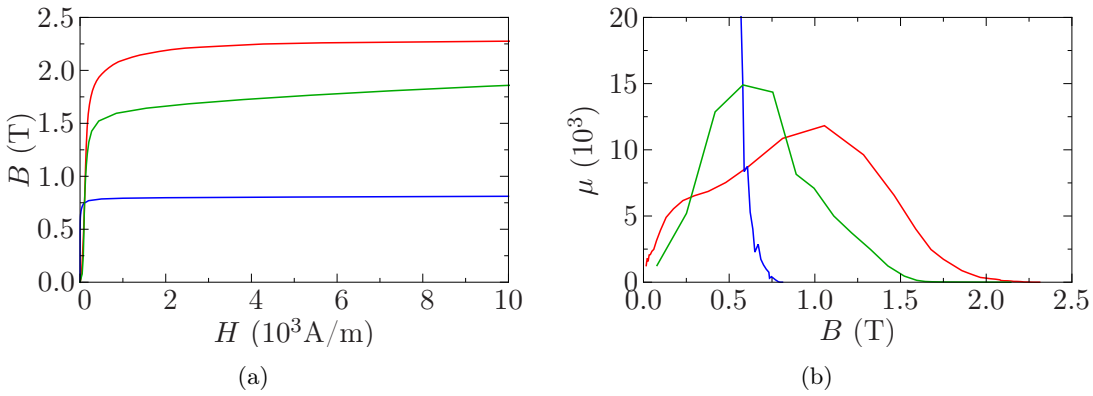

Figure 4.5 – (a) Initial magnetization curve of *Mu-metal* (blue), *VacoFlux* (red) and magnetic iron (green). It is valid for materials, which are demagnetized in the initial state. (b) The corresponding relative permeability μ as function of the magnetic flux density.

In order to determine the most suitable material for the present set-up 1, one can utilize a first order approach. In this approach it is assumed that the whole outer magnetic flux Φ_O flows through a cylindrical magnetic shielding, as shown in figure 4.6. The outer flux Φ_O is defined as the flux, which is not passsing through the bore of the solenoid. After

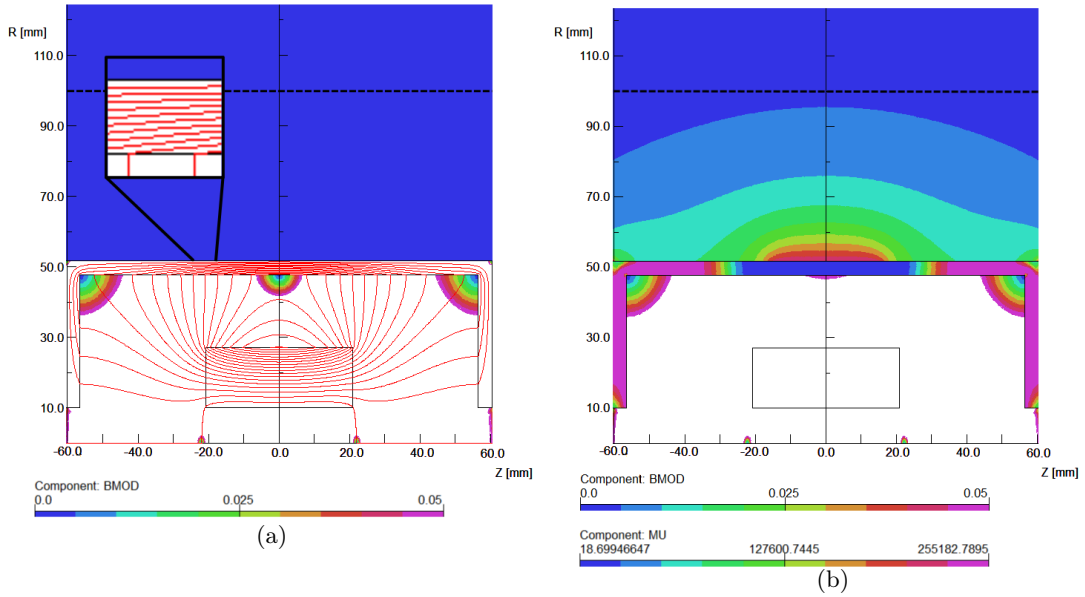

Figure 4.6 – (a) Simulation of the *VacoFlux* shielding for set-up 1. The color indicates the magnitude of the magnetic field. The red lines represent the magnetic field lines. In the inset, one can see that the field lines within the shielding are equidistant and parallel to the z-axis in the cylinder jacket.
(b) Simulation of the *Mu-metal* shielding. The color outside the shielding indicates the magnitude of the magnetic field, while the color in the region of the shielding shows the relative permeability (note the two color scales). The magnetic field leaves the shielding, where the shielding material is in saturation.

the calculation of Φ_O, it can easily be translated to a magnetic flux density inside the shielding for given shielding dimensions.
This flux density can be correlated to a certain permeability for the different materials (cf. figure 4.5). The higher the permeability, the more reasonable is the assumption that the whole flux flows through the shielding and hence the better is the shielding behavior. In general, a magnetic flux through a certain face A is defined by

$$\Phi = \int_A \boldsymbol{B} \mathrm{d}\boldsymbol{A}. \tag{4.4}$$

According to equation (4.4), the outer magnetic flux for set-up 1 is given by the integral of the magnetic flux density over the x-y-plane, except the cross sectional area of the

solenoid. Hence, Φ_O can be determined by

$$\begin{aligned}\Phi_O &= \int_{R_o}^{\infty}\int_{0}^{2\pi} B_z \mathrm{d}\varphi \mathrm{d}r \\ &= 2\pi\bar{r}\int_{R_o}^{\infty} B_z \mathrm{d}r \\ &= 2.02\times10^{-3}\,\mathrm{Wb},\end{aligned} \tag{4.5}$$

where the integral and $\bar{r}$ — the centroid of the magnetic field distribution $B_z(r)$, $r \in [27.1\,\mathrm{mm}, 200\,\mathrm{mm}]$ on the r-axis — are both obtained from the 2D simulation.
For a shielding cylinder with an outer radius of $R_{\mathrm{o,Shd}} = 51.7\,\mathrm{mm}$ and a wall thickness of $d = 4\,\mathrm{mm}$, the magnetic flux Φ_O yields to the magnetic flux density inside the cylinder jacket

$$B = \frac{\Phi_O}{A} = \frac{\Phi_O}{2\pi\,(R_{\mathrm{o,Shd}} - d/2)\,d} = 1.62\,\mathrm{T}, \tag{4.6}$$

where it is assumed that the flux density B is constant over the cross sectional area A and only directed along the z-axis $B = B_z$. This is a reasonable approximation, as indicated in the inset of figure 4.6.
The determined flux density corresponds to a relative permeability of $\mu_{\mathrm{Vaco}} \approx 4000$ for *VacoFlux* and $\mu_{\mathrm{Mu}} = 1$ for *Mu-metal*. The reason for this large difference is the saturation effect of *Mu-metal* (slope in the $B(H)$ curve drops to $\mu_0\mu = \mu_0$), which occurs for the present external magnetic field strength. Even if only half of the outer flux Φ_O is directed through the magnetic shielding, the *Mu-metal* will still be in saturation.
Increasing the wall thickness would be a measure to avoid the saturation effects in *Mu-metal*, but it is not an option here since the shieldings, shown in figure 4.6, have already a weight of 1.7 kg. Thus, *VacoFlux* is preferable over *Mu-metal* for the present shielding problem of set-up 1. This result, which is calculated by the first order approach, can also be found in the simulations, illustrated in figure 4.6. The definition of a shielding factor

$$S = B_{in}(r = 42.7\,\mathrm{mm}, z = 0\,\mathrm{mm})/B_{out}(r = 56.7\,\mathrm{mm}, z = 0\,\mathrm{mm}) \tag{4.7}$$

shows that the shielding of *VacoFlux* with $S_{\mathrm{Vaco}} = 257$ is much more effective than the one of *Mu-metal* with $S_{\mathrm{Vaco}} = 3$.
The deflection of an electron beam, that passes the set-up in figure 4.6 (a) on the dashed line, is still a parallel offset. But the offset is reduced by a factor of approximately 150 compared to the set-up without any shielding. Such an offset of 45 µm would be acceptable for the REAGE-experiments but the weight of the shielding is more than two times larger than feasible.
So the next step during the development of a viable shielding should be a reduction of

the shielding's weight.
This can be achieved by a closer investigation of the magnetic flux along the shielding.

4.1.2 Thickness modulation along the shielding

In the previous section, a first order approach has been used to determine a suitable shielding material. This approach consists of the assumption, that the whole outer flux of set-up 1 flows through the shielding. Hence, the magnetic flow is assumed to be constant along the shielding, so that a uniform wall thickness along the shielding is the logical consequence of this approach.
A second order approach, in which it is taken into account that not the whole outer flux flows through the shielding and that the flux varies along the shielding, is more realistic. Due to the imperfectness of the shielding ($\mu \neq \infty$), there is of course magnetic flux in the space between the solenoid and the shielding and even a small fraction outside of the shielding. Since parts of this magnetic flux enter or leave the shielding at different positions, the assumption of a constant flux along the shielding is not valid anymore.
This fact leads to the possibility to remove shielding material at positions of low magnetic flux. In order to determine the flux distribution inside the shielding, 2D-FEM simulations are performed.
But instead of using the nonlinear material analysis, simulations for linear materials are applied. The nonlinear material analysis would take the $B(H)$ curves of the occurring materials into account and solve the two reduced Maxwell equations for the magnetostatic fields self consistently by iteration. The iteration process is necessary because of the dependency $\mu(B) \leftrightarrow B(\mu)$.
For linear materials, the field equations are solved under the assumption that the given permeability μ_{sim} is independent from the magnetic flux density inside the material. This kind of simulation is ideal to determine the magnetic flux distribution along the shielding for a certain wall thickness and a constant permeability.
The result of such a simulation with $\mu_{\mathrm{sim}} = 4250$ is shown in figure 4.7. The value of the permeability is not arbitrarily chosen but will finally lead to a shielding weight of 650 g)

Using the following equations for the calculation of the magnetic flux

$$\begin{aligned} \Phi_j(z) &= 2\pi\,(R_{\mathrm{o,Shd}} - d/2)\,dB_j(z), \quad z \in [-57.5\,\mathrm{mm},\, 0\,\mathrm{mm}], \quad r = 49.2\,\mathrm{mm} \\ \Phi_c(r) &= 2\pi r dB_c(r), \quad r \in [10\,\mathrm{mm}, 49.7\,\mathrm{mm}], \quad z = -57\,\mathrm{mm}, \end{aligned} \tag{4.8}$$

where j and c stand for the jacket and the cap of the cylindrical magnetic shielding, the relation between thickness of the shielding d and the magnetic flux density $B_{j/c}(d)$ becomes

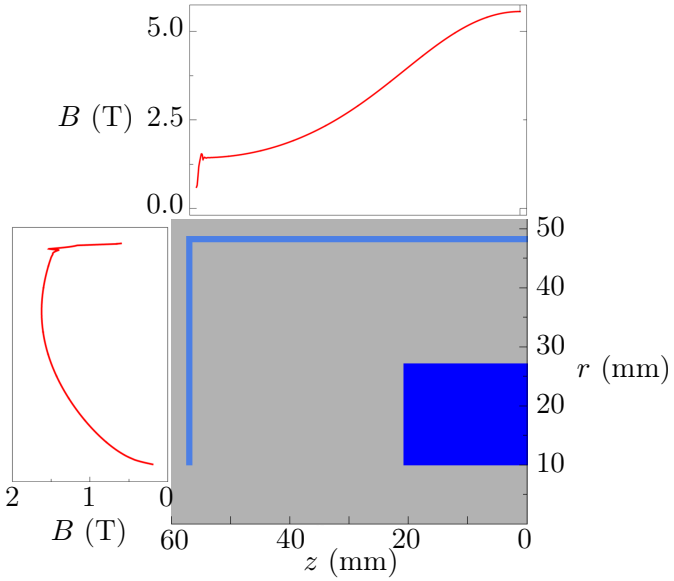

Figure 4.7 – The lower right side shows half of set-up 1 with a magnetic shielding of constant thickness. The lower left and the upper graph show the magnetic flux density inside the shielding, which is directly obtained from the simulation by line-outs.

evident. With the requirement that the magnetic flux density is equal to $B_{\mathrm{sim}} \approx 1.6\,\mathrm{T}$, which in the case of VacoFlux corresponds to the permeability $\mu_{\mathrm{sim}} = 4250$ defined in the simulation:

$$B_{j/c}(d) \stackrel{!}{=} B_{\mathrm{sim}}, \tag{4.9}$$

one can determine a magnetic shielding with variable wall thickness but almost constant permeability $\sim \mu_{\mathrm{sim}}$ along the shielding.
This is an important requirement for an effective and light weight magnetic shielding, since strongly varying permeabilities along a shielding are counterproductive.
Parts of a shielding with a much higher permeability than the mean permeability of the shielding contribute little to a higher shielding factor because the attracted magnetic flux will leave the shielding again elsewhere. Hence, at this points the weight of the magnetic shielding is unnecessarily increased.
Parts with a much lower permeability than the mean permeability lead to a strong leakage of the magnetic flux and therewith diminish the effectiveness of the shielding.

The resulting wall thickness of the above described algorithm can be seen in figure 4.8. The large variations of the magnetic flux $\Phi_j(z)$ and $\Phi_c(r)$ lead to wall thicknesses in the range of 0.12 mm to 3.3 mm. In figure 4.9, the shielding with an adapted thickness and a weight of about 650 g is compared to a shielding with constant thickness and the same

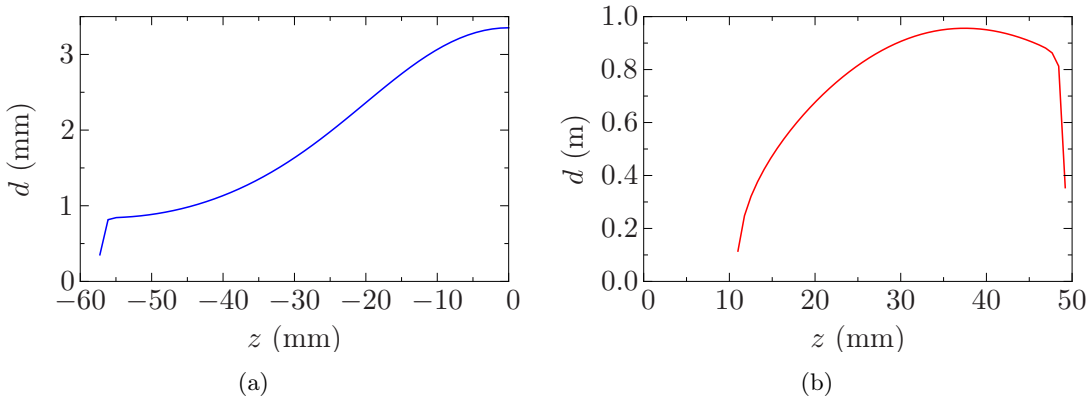

Figure 4.8 – (a) Modulation of the wall thickness $d_{\mathrm{Shd}}(z)$ for the cylinder jacket. It allows for a constant permeability inside the shielding
(b) Modulated wall thickness $d(r)$ along the cylinder cap.

weight. Of course, this time a nonlinear material simulation is performed.
As can be clearly seen, the adaption of the shielding thickness to the magnetic flux leads to an almost constant permeability and hence to an improved shielding behavior. For the shielding with constant thickness, the drop in permeability at $z = 0$ due to saturation effects causes a significant leakage of magnetic flux. In consequence, the shielding factor, defined in equation 4.7, is given by $S_{\mathrm{var}} = 95$ for the shielding with variable thickness and only $S_{\mathrm{const}} = 3$ for the one with constant thickness.
In the set-up of figure 4.9 (a), the radial component of the magnetic flux density along the line $r = 100\,\mathrm{mm}$ leads to a parallel offset of $105\,\mu\mathrm{m}$. In figure 4.9 (b), an offset of $2.33\,\mathrm{mm}$ results, where for both cases an electron beam with $5.6\,\mathrm{MeV}$ is assumed.
With respect to the shielding factor and the deflection of an electron beam the shielding with an adapted thickness is several ten times better than a shielding with a constant wall thickness. This improvement leads to tolerable deflections in the form of parallel offsets on the order of $100\,\mu\mathrm{m}$, so that the solution with an adapted wall thickness is pursued in the following of this work.

In order to check the possibility of using magnetic iron instead of *VacoFlux*, the whole algorithm is repeated with the magnetic properties of *Armco* iron (cf. figure 4.5). The only necessary modification is to insert the new magnetic flux density $B_{\mathrm{sim}} \approx 1.1\,\mathrm{T}$, which corresponds to the permeability $\mu_{\mathrm{sim}} = 4250$ for *Armco* iron, into equation (4.9). The result is a shielding with similar shielding properties but with a weight of $1.01\,\mathrm{kg}$ that is significantly above the permitted weight.
Thus, the more expansive *VacoFlux*, which is in addition difficult to process, seems to be

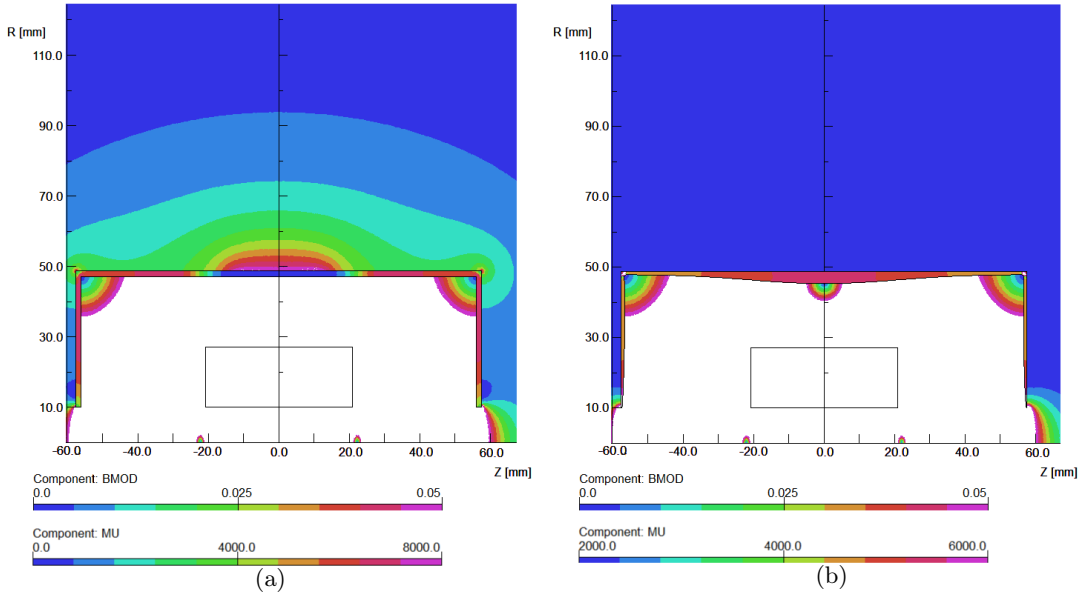

Figure 4.9 – (a) Simulation of a shielding with constant wall thickness and a weight of 0.65 kg. The color in the cross sectional area of the shielding indicates the relative permeability. The color in the remaining regions show the magnetic flux density in Tesla (note the two color scales).
(b)Corresponding simulation for a shielding with modulated wall thickness and the same weight. The permeability fluctuates much less than in (a)

the only suitable material for the shielding of set-up 1.

4.1.3 Dimensions of the shielding

In a last step, the optimal dimensions $R_{\mathrm{o,Shd}}$ and $L/2_{\mathrm{o,Shd}}$ for a magnetic shielding should be determined.
Increasing one or both dimensions of the shielding will lead to a higher weight for the case that the wall thickness is left unchanged. But a larger shielding will lead to a reduced magnetic flux inside the shielding, simply due to the fact that a larger part of the flux will flow through the volume in-between the solenoid and the shielding. In consequence, the wall thickness could be reduced while keeping the relative permeability constant inside the shielding.
Wether the weight increase due to a larger shielding dimension or the weight reduction caused by a decreased wall thickness is dominant, will be investigated in the following.

Therefore the algorithm for the adaption of the wall thickness to the local magnetic flux is performed for different shielding dimensions.
In a first run, the radius of the shielding $R_{\mathrm{o,Shd}}$ is varied in the range between 35 mm and 95 mm for a fixed length $L/2_{\mathrm{o,Shd}} = 57.5\,\mathrm{mm}$.
In a second run, the length of the shielding is varied in the range between 57.5 mm and 79.5 mm, while the radius is kept fixed at $R_{\mathrm{o,Shd}} = 59.7\,\mathrm{mm}$. The weight is determined for every shielding dimension.
The results of these investigations are shown in figure 4.10. On the left side, the weight

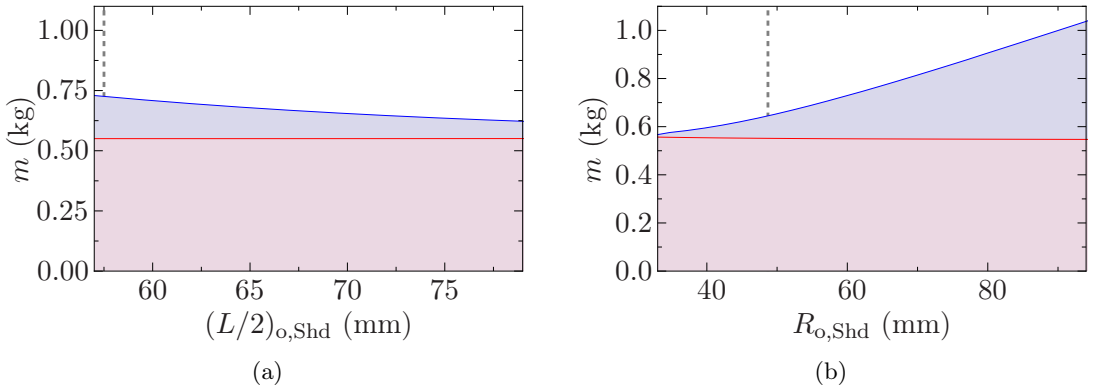

Figure 4.10 – (a) Weight of the shielding for different lengths of the shielding but a fixed relative permeability ($R_{\mathrm{o,Shd}} = 59.7\,\mathrm{mm}$). The line indicates the upper limit, which is set by the experimental set-up.
(b) Weight of the shielding for different outer radii ($L/2_{\mathrm{o,Shd}} = 57.5\,\mathrm{mm}$). The lower limit at 48.7 mm is determined by the constraint that the losses of the focusing strength within the shielding should not reach 10 %.

of the shieldings with a fixed permeability $\mu \approx 4250$ but varying length is depicted. One can see, that the weight can be reduced by lengthening the shielding. With respect to the cylinder jacket the loss of weight due to the reduced wall thickness exactly compensates the gain of weight, caused by the lengthening. Only at the cylinder caps of the shielding, a reduction of weight can be achieved.
Together with the fact, that a larger shielding leads to less negative effects for the focusing properties, the reduction of weight by lengthening is the reason to exploit the maximal possible length $L/2_{\mathrm{o,Shd}} = 57.5\,\mathrm{mm}$. It is determined by the experimental set-up of the TEM experiment (cf. section 3.1).
In figure 4.10 (b) the weight as a function of the radius $R_{\mathrm{o,Shd}}$ is shown. Again, the weight of the cylinder jacket is not dependent on the radius if the permeability inside the shielding is kept fixed. The weight of the cylinder caps decrease for smaller radii.

Investigations of the focusing strength and performance of the shielded PMS have shown, that they also diminish for smaller radii.
So, for the determination of a suitable radius a trade off between the reduction of weight and reduction of the focusing strength/performance has to be made. Similar to the definition of an upper limit for the length of the magnetic field $(w/2)_{\max}$ inside a magnetic shielding (cf. section 3.1), a lower limit of the shielding's radius is set at the point, where 10 % of the initial focusing strength is lost. This point is reached at the radius $R_{\mathrm{o,Shd}} = 48.7\,\mathrm{mm}$.

In conclusion, shielding cylinders with larger length, smaller radius and the same relative permeability (which leads to comparable shielding factors) have a reduced weight. This fact is taken into account for the shielding design.
Due to the length limitation and the lower limit for the radius, suitable dimensions for a light weight, effective shielding are found to be $L/2_{\mathrm{o,Shd}} = 57.5\,\mathrm{mm}$ and $R_{\mathrm{o,Shd}} = 48.7\,\mathrm{mm}$. This knowledge is already used in section 4.1.2, so that the performance of the shielding with these dimensions is illustrated in figure 4.9.

4.1.4 Influence on the focusing properties of the PMS

In the last section, the influence of the shielding on the focusing characteristics of the PMS has been mentioned. In chapter 3, this influence has already led to a length limitation for the magnetic field of a PMS. The reason for the introduction of a length limitation $(w/2)_{\max}$ has been qualitatively explained in section 3.1. It is intended to prevent, that a PMS inside a magnetic shielding exhibit a too small focusing strength (losses larger than 20 %) or significantly diminished focusing performance.
How the quantitative implication $(w/2)_{\max} = 35\,\mathrm{mm}$ is deduced, has not been explained and is therefore shown here.

In order to determine the half length $(w/2)_{\max}$, the above mentioned dimensions of a magnetic shielding are assumed. They are not changed anymore for different PMSs since the maximal length of the shielding, which is optimal with respect to the weight and the focusing characteristics, is already reached. The radius of the shielding could be increased in order to improve the focusing characteristics of some PMSs, but regarding the weight in figure 4.10 (b), there is not much scope anymore.
Linear material simulations for PMSs with different lengths of the magnetic field — inside the magnetic shielding of figure 4.7 — are performed with a relative permeability of the shielding given by $\mu_{\mathrm{Shd}} = 4250$. This kind of simulation exhibits the advantage that the adaption of the wall thickness has not to be done for all different cases. The longitudinal on-axis fields for the different PMSs are obtained by line-outs and are used to determine

the focusing strength and performance.
The results are shown in figure 4.11, where (a) depicts the focusing strength and (b) the focusing performance. As can be seen, a 20 % loss of the focusing strength occurs

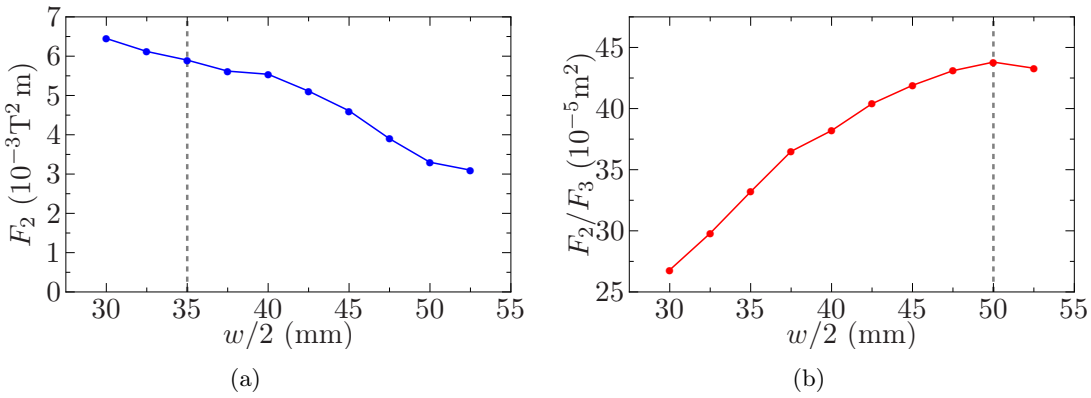

Figure 4.11 – (a) Focusing strength for PMSs with different length of the magnetic field $w/2$. The dashed line shows $(w/2)_{\max}$. It is set, where 20 % of the focusing strength for the PMS without shielding are lost.
(b) The focusing performance of the different PMSs. The optimum cannot be used due to $(w/2)_{\max}$ from (a).

much earlier ($w/2 = 35$ mm) than a local maximum of the focusing performance ($w/2 = 50$ mm). The critical reason for the focusing strength losses can be seen in figure 4.12. For shorter magnetic field distributions the positive peak is only slightly diminished by the surrounding shielding, while for long distributions a significant part of the inner flux (positive peak) is redirected by the shielding. Hence, for this type of PMS (set-up 1) the length limitation is set at $(w/2)_{\max} = 35$ mm by the occurring focusing strength losses within a magnetic shielding.

4.2 Magnetic shielding of two radially magnetized solenoids

The studies on a magnetic shielding of an axially magnetized solenoid can be performed analogously for two radially magnetized solenoids (set-up 4). Thus, the investigations are documented here in a more compact way since they have been comprehensively explained in section 4.1.

The 2D FEM simulations of set-up 4 without a shielding, by which one can determine if a shielding is required or not, show quite different results than the simulations of set-

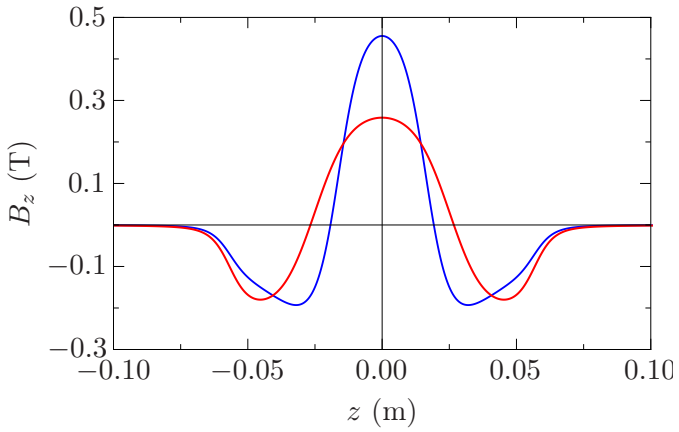

Figure 4.12 – The longitudinal on-axis fields for two different PMSs inside a magnetic shielding. The blue curve corresponds to a PMS, which exhibits a magnetic field length of $w/2 = 32.5\,\mathrm{mm}$ in the unshielded condition. The red curve would have a magnetic field length of $w/2 = 50\,\mathrm{mm}$.

up 1. The magnitude of the magnetic field around the PMS is illustrated in figure 4.13. In comparison to figure 4.1 one can see, that the magnetic stray fields in set-up 4 are much less pronounced than in set-up 1. This advantageous behavior is also visible in the line-out of B_y along the dashed line, which is shown in figure 4.14 (a).
This component of the magnetic field, which is perpendicular to the direction of motion of the electron beam, does not exceed values above 2 mT. Therefore its maximum is approximately four times smaller than the maximum, which occurs in set-up 1 on the same line-out.
Also interesting is the totally different field distribution. Instead of one change of direction and a central symmetry, which lead to the parallel offset in set-up 1, three changes of direction and a central symmetry are visible.
The resulting deflection of an electron beam, which propagates along the dashed line in figure 4.13 with a mean beam energy of 5.6 MeV, is calculated by means of equation (4.1) and is shown in figure 4.14 (b). As can be seen, the electron beam describes one period of a wiggling process, so that the effective deflection behind the stray field of the PMS is with $x = -3\,\mu\mathrm{m}$ close to zero. The amplitude of this wiggling motion is also surprisingly small with $x_{\max} = 100\,\mu\mathrm{m}$.
In comparison to the maximal deflection of the electron beam for set-up 1 with magnetic shielding, it turns out that the maximal deflection for set-up 4 without shielding is even slightly smaller. From this point of view, a magnetic shielding for set-up 4 is not necessarily required.

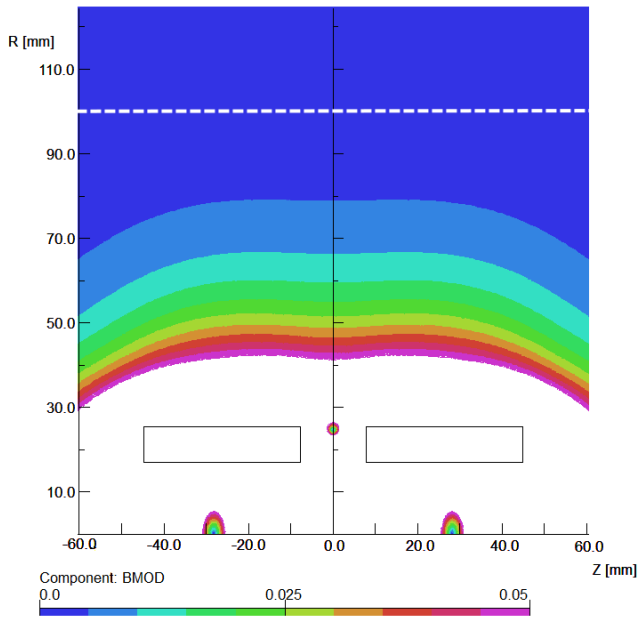

Figure 4.13 – 2D FEM simulation of set-up 4. The colors indicate the magnitude of the magnetic field in Tesla. White regions exhibit magnetic fields larger than 50 mT.

But it again has to be assured that the two PMS-systems do not exert magnetic forces larger than 3 N on each other. As mentioned before, these longitudinal forces would act on the piezo-based micropositioning stages, which are not designed to withstand that. Three dimensional FEM simulations performed with CST EM Studio have shown, that this requirement is not or only narrowly fulfilled for set-up 4 without a shielding.
It turned out that the magnetic force calculations for this set-up with four magnets are strongly dependent on the three dimensional mesh, which is utilized in the FEM simulation. Hexahedral meshes, where the simulation volume is divided into little cuboids, show less accurate force calculations than tetrahedral meshes, where the volume is divided into small tetrahedrons. The accuracy is assessed by the vectorial sum of the forces on all parts. This sum should be zero for the present closed system without any external force. Hence the difference from zero can be used as a measure of quality of the simulation.
In figure 4.15 the results of the best hexahedral and tetrahedral simulation are shown. Here, the mid points of the two PMS-systems have a distance of approximately twice the focal length for a beam energy of 3 MeV ($f_{3\ \mathrm{MeV}} \approx 160\,\mathrm{mm}$).
Considering the fact that both annular permanent magnets of each PMS-system are mechanically connected to each other and placed on a micropositioning system, leads to a resulting force of 1.1 N on both micropositioning systems for the tetrahedral simulation.

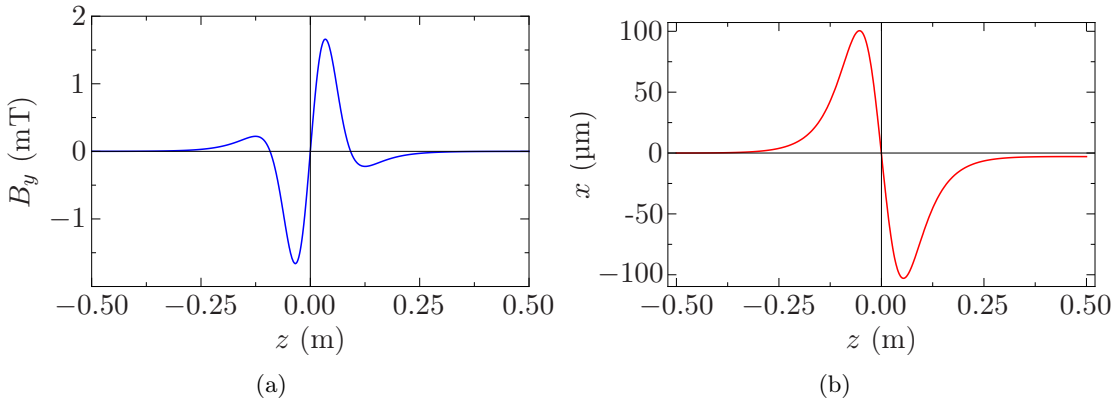

Figure 4.14 – (a) Line-out of B_y along the white dashed line in figure 4.13
(b) The deflection of an electron beam with a mean beam energy of 5.6 MeV caused by the magnetic field shown in (a).

The hexahedral simulation shows resulting forces of −5.2 N on the left system and 3.1 N on the right system.
Due to the large variances in the determination of the forces and since some simulations show forces, that are larger than 3 N, the decision to develop a magnetic shielding is made. Once the PMS systems are fabricated, it will be easy to measure the occurring forces and to judge if the magnetic shielding should be installed or not.
An advantage of a shielding will be, that the micropositioning stages are not damaged if the distance between the two PMSs inside the target chamber should fall below 160 mm.

4.2.1 Thickness modulation along the shielding

For set-up 1, a suitable shielding material has been determined in a separate section 4.1.1 in order to explain the importance of the material's saturation flux density as example. For this set-up, the selection of the right material will be done during the adaption of the wall thickness. Analogously to section 4.1.2, a linear material simulation is performed for set-up 4 that is surrounded by a shielding cylinder. This leads to the magnetic flux density distribution inside a shielding with constant permeability $\mu = 4250$.
Figure 4.16 shows the simulated configuration on the lower right side and the obtained magnetic flux density distributions on the lower left and upper right. Comparing it with figure 4.7 one can see that the distribution looks totally different than for set-up 1.
The big difference illustrates the importance to match the shielding to any particular magnet set-up, if special measures like wall thickness adaption are applied to reduce the

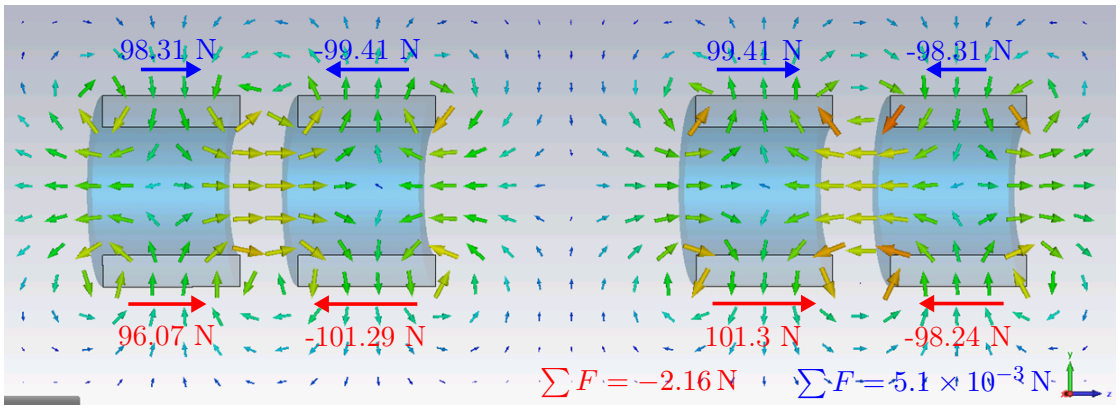

Figure 4.15 – Simulation of the forces onto the PMSs in set-up 4. The red values indicates the results, achieved with a hexahedral mesh. The more accurate results are achieved with a tetrahedral mesh. They are shown as blue values. The sum of the forces can be understood as measure of the simulation quality.

shielding's weight.

Using equation (4.8) yields the magnetic flux distribution. Subsequently, the adapted wall thickness can be calculated by supposing a constant flux density distribution along the shielding. In the case of utilizing *VacoFlux* as shielding material, $B \approx 1.6\,\mathrm{T}$ makes the presumed permeability of $\mu = 4250$ possible. For *Armco* iron the analogue flux density is given with $B \approx 1.1\,\mathrm{T}$.
The resulting thickness along the shielding is depicted in figure 4.17 for both cases. The corresponding masses are calculated to 0.26 kg for the use of *VacoFlux* and to 0.38 kg if *Armco* iron is utilized. At this point, the already observed advantage of set-up 4 concerning magnetic stray fields can be clearly seen.
Here, the stray fields are much smaller than the ones, which occur in set-up 1. Even a shielding out of magnetic iron weighs only 60 % of the *VacoFlux* shielding with similar permeabilites, used in set-up 1. Therefore, the much cheaper and easier to process magnetic iron can be used to shield the two radially magnetized PMSs.
The shielding factor could of course be increased until the maximal weight of 0.7 kg. But in chapter 5, which will deal with the technical realization of the so far theoretical design considerations, it is shown that additional weight is needed to achieve vacuum suitability of set-up 4. Hence, the thickness modulation from figure 4.17 is used for the shielding, which is shown in figure 4.18 (a).
The simulation shows that the permeability inside the shielding does not drop below 4150 and therefore the flux density beyond the shielding is effectively reduced compared to the case without a shielding in figure 4.13.

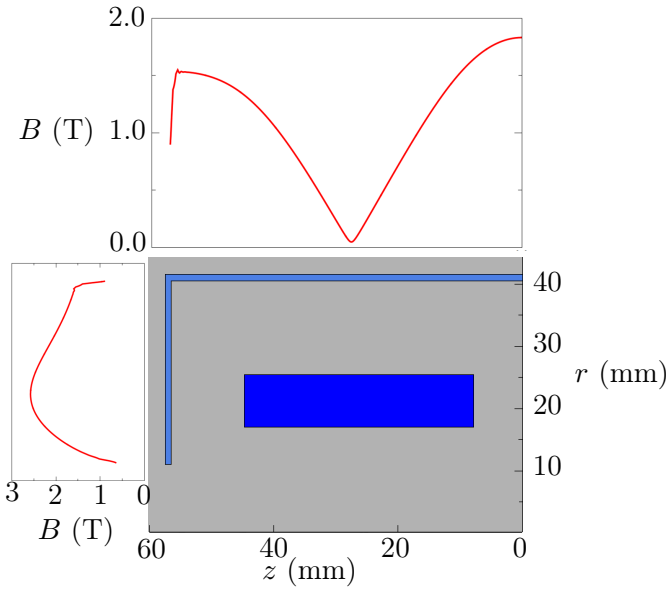

Figure 4.16 – The lower right side shows half of set-up 4 with a magnetic shielding of 1 mm wall thickness. The lower left and the upper graph show the magnetic flux density inside the shielding. It is directly obtained from the linear material simulation by line-outs.

To quantify this fact, a shielding factor is defined

$$S = B_{in}(r = 36.5\,\text{mm}, z = 0\,\text{mm})/B_{out}(r = 45.5\,\text{mm}, z = 0\,\text{mm}), \tag{4.10}$$

which reaches the value of 129.
In figure 4.18 (b), the corresponding deflection of an electron beam ($\gamma \approx 12$), which is passing along the dashed line, is shown as blue curve. It is compared to the deflection by a shielding with constant wall thickness and a weight of 0.38 kg (red curve). One can see the advantage of the wall thickness modulation, which is not that distinct as it was the case for set-up 1. But the parallel offset is still reduced by a factor of 2.6, so that the shielding with modulated wall thickness is preferred. Its parallel offset of 56 µm is satisfying. It should be noted that the final deflection after the wiggling motion for set-up 4 without shielding was only 3 µm. But the amplitude of the wiggling process is larger than 100 µm and even more important, the magnetic forces on the micropositioning stage could exceed the limit of 3 N without a magnetic shielding.

Due to the relaxation of the weight problem, different dimensions of the shielding are not considered. Other than for set-up 1, a magnetic shielding in general and especially with small radius $R_{\text{o,Shd}}$ does not diminish but increase the focusing strength of two

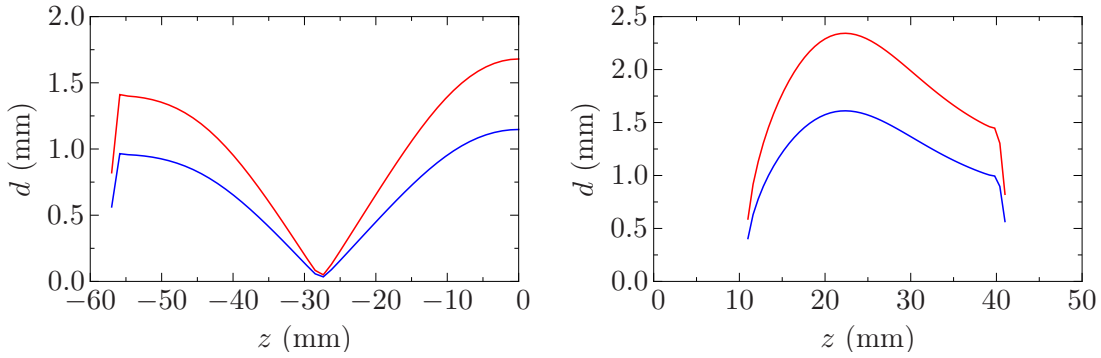

Figure 4.17 – (a) Adapted wall thickness $d(z)$ for the cylinder jacket, which allows for a constant permeability inside the shielding. The blue and red curve show the wall thicknesses of a *VacoFlux* and a magnetic iron shielding respectively.
(b) Modulation of the wall thickness $d(r)$ along the cylinder cap. They are both determined with the simulated flux density, illustrated in figure 4.16. The drop of the wall thickness at the point where the cylinder cap and jacket interfere is neglected for the further shielding design.

radially magnetized PMSs (cf. next section 4.2.2). This fact is the second reason, why the shielding's dimensions are not as critical as for set-up 1.

4.2.2 Influence on the focusing properties for two radially magnetized solenoids

In analogy to the investigations of a magnetic shielding for set-up 1, the effect of the shielding onto the focusing properties of set-up 4 is studied. The influence on the focusing properties, which is dependent on the length of the magnetic field distribution $w/2$ along the z-axis, has led to an upper limit for $w/2$ in section 3.4.

The value of this upper limit is determined in the following. Therefore, linear material simulations for PMSs with different lengths $w/2$ of the magnetic field within a magnetic shielding are performed. For every investigated length, the parameter set from figure 3.14 is chosen, which exhibits the respective length $w/2$ and the best focusing performance under this condition. The relative permeability of the shielding is fixed with $\mu_{\mathrm{Shd}} = 4250$ and the dimensions of the shielding can be seen in figure 4.16. This linear simulation exhibits the advantage that the adaption of the wall thickness has not to be done for all the different PMSs in order to achieve a constant permeability along the shielding.

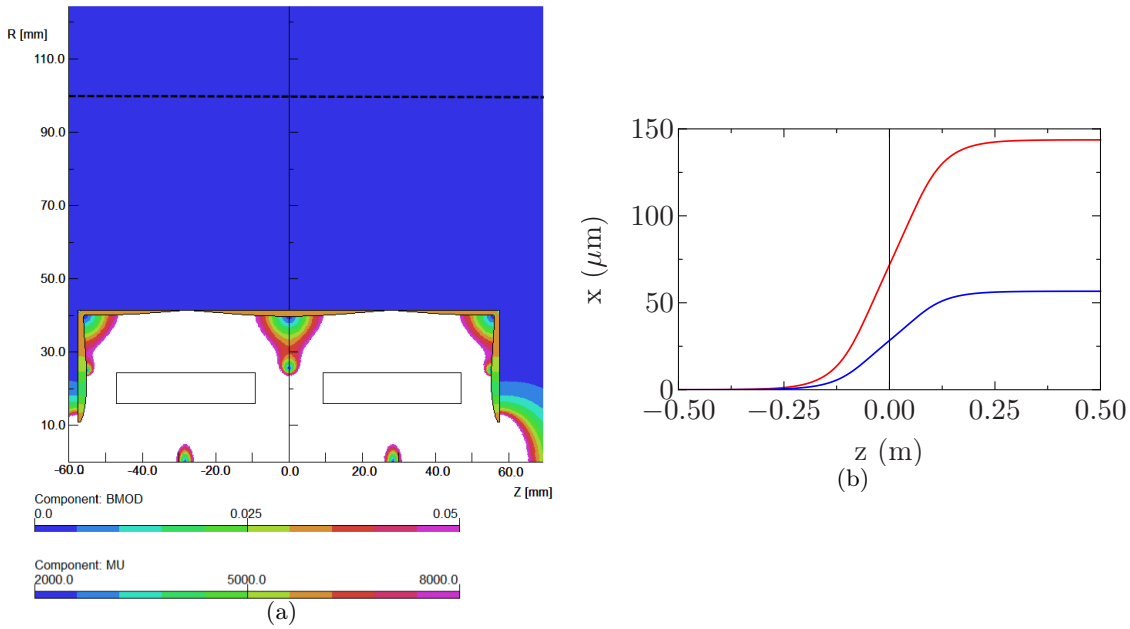

Figure 4.18 – (a) Simulation of the shielding with modulated thickness. The color in the region of the shielding shows the permeability. The color in the other regions indicates the magnetic flux density in Tesla.
(b) The blue curve shows the deflection of an electron beam with $\gamma = 12$. It passes the PMS on the dashed line in (a). If one would use a shielding with constant wall thickness, the deflection of the beam is shown by the red curve.

From the simulated longitudinal on-axis fields, the focusing strength and performance for the different PMSs are determined and shown in figure 4.19.
One big advantage of set-up 4, which is visible in figure 4.19 (a), is the fact, that a surrounding shielding does not decrease the focusing strength. Even for larger length of the magnetic field distribution, the shielding has almost no influence on the focusing strength. A major reason for this is, that the magnetic flux in-between the two radially magnetized solenoids is "protected" so that it is not redirected through the shielding. It can be seen in figure 4.20, where one short and one long magnetic field distribution is shown before and after application of the shielding. In any case the positive peak almost retains its initial form.
This is a big difference to an axially magnetized solenoid (cf. figure 4.12). As consequence, the upper limit of the length is not anymore set by a loss of the focusing strength by 20 % but reached at the point $(w/2)_{\max} = 45\,\mathrm{mm}$, where the maximal focusing performance is reached.

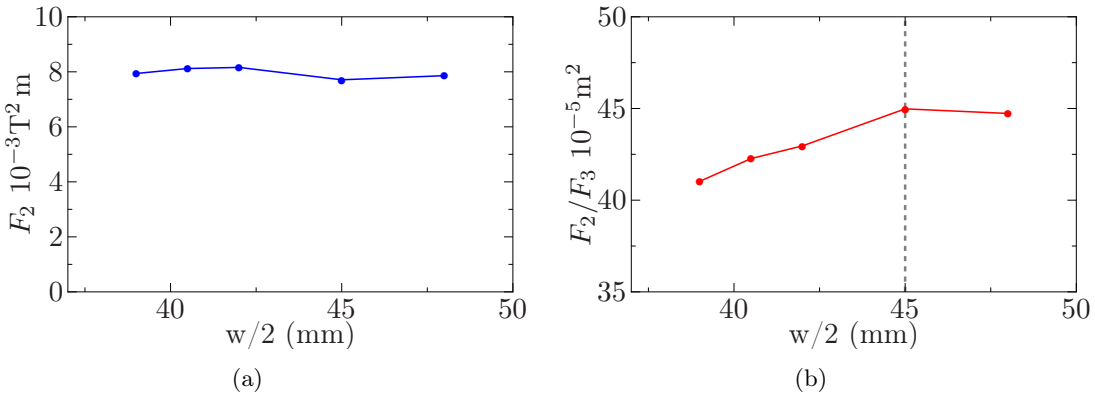

Figure 4.19 – (a) Focusing strength for PMSs with different length of the magnetic field $w/2$. It is almost not influenced by the surrounding shielding, even for long magnetic fields.
(b) The focusing performance of the different PMSs. Due to the fact that there are no losses in focusing strength, the length limitation is set at the optimum of the focusing performance $(w/2)_{\max} = 45$.

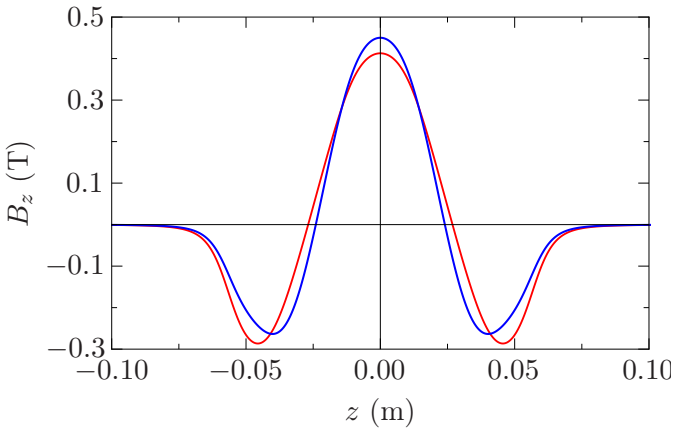

Figure 4.20 – The longitudinal on-axis fields for two different PMSs inside a magnetic shielding. The blue curve corresponds to a PMS, which has a magnetic field length of $w/2 = 39\,\mathrm{mm}$ in the unshielded condition. The red curve shows the field of a PMS, which exhibits $w/2 = 45\,\mathrm{mm}$ without a shielding.

In conclusion, for both set-ups 1 and 4 a feasible magnetic shielding could be developed. Set-up 4 exhibits not only the better focusing performance (F_2/F_3 is 65 % larger than set-up 1 without shieldings and 54 % larger within shieldings), but also advantages with respect to its behavior within a magnetic shielding (no losses of focusing strength and less magnetic stray fields, which leads to a lighter shielding). Thus, set-up 4 is preferred over set-up 1. In the next chapter 5 the technical realization of the theoretical design studies for set-up 4 is presented.

5 Technical Implementation

Chapter 3 dealt with the design of a PMS with large focusing strength and preferably small induced emittance growth. It led to a PMS, consisting of two radially magnetized annular permanent magnets, since this design shows significant advantages concerning emittance growth and the possibility to magnetically shield it. In chapter 4 a magnetic shielding of this PMS was developed so that these focusing elements can be used in REGAE's future target chamber.
The considerations in both chapters were rather theoretical without including the aspect of producibility. This chapter is about the transfer of the theoretical ideas into a technically feasible solution. It also contains a first analysis of possible errors concerning focusing strength and induced emittance growth, which are caused by unavoidable production tolerances.

5.1 Implementation of two radially magnetized solenoids

For the most promising PMS, set-up 4, which was found in chapter 3, two annular permanent magnets are required. The magnetization of these magnets has to point in radial direction. While it points towards the rotation axis for one magnet, it points against the rotation axis for the second magnet (cf. figure 3.13). In dialogue with an experienced manufacturer of neodymium (NdFeB) magnets, the Vacuumschmelze GmbH (VAC) [51], it turned out that the demanded radial magnetization cannot be fabricated. The radial alignment of the microscopic magnetic moments in a NdFeB-powder is in general possible. Also the next manufacturing step, the pressing of the magnetic powder is feasible. But the required final sintering process cannot be performed, since it lets burst the magnet into many fragments. This is due to the strong anistropy of the thermal expansion coefficient, which is associated with the magnetic anisotropy. Since the anisotropy of the thermal coefficient of the powder elements has to be unidirectional for a stable macroscopic magnet, only unidirectional magnetizations are feasible.
But an annular permanent magnet with radial magnetization can be approximated by using several wedges with unidirectional magnetization like it is illustrated in figure 5.1. Twelve wedges are a common segmentation, which is used for permanent magnetic

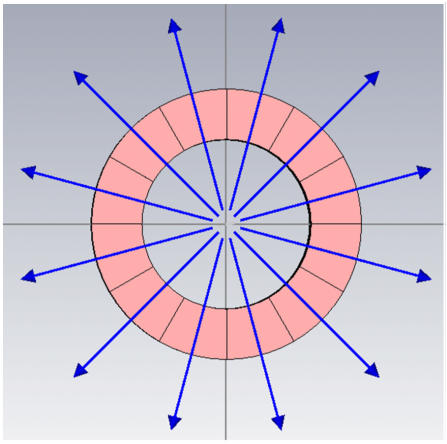

Figure 5.1 – Approximation of a radially magnetized solenoid by twelve unidirectional magnetized wedges.

quadrupoles [48] and will be used here as well.
In order to achieve an accurate positioning of these wedges (gap sizes between the wedges under 50 µm) it is essential to glue them. Using a housing for positioning would lead to an average gap size of about 0.1 mm between the twelve wedges. Since the wedges will more or less randomly align in the housing, gap sizes significantly larger than 0.1 mm cannot be excluded.
The utilization of glue leads to the requirement that the set-up has to be encapsulated leak-tight because no kind of glue is suitable for the required vacuum inside the target chamber. The material of choice for such an encapsulation is a non-magnetic steel, as the leak-tight welding of non-magnetic steel is a proved method at VAC, which is not the case for aluminium. As consequence, the encapsulation will weigh about 0.3 kg. This is the reason, why the weight of the magnetic shielding has been kept beneath 0.4 kg in section 4.2.1.
The necessity of a welded encapsulation has a further consequence. The occurring heat during the welding process does not allow to use the permanent magnetic material *Vacodym 745 HR* with a remanence field of $B_R = 1.44\,\mathrm{T}$ at room temperature, which has been foreseen in chapter 3 and 4. Exceeding a temperature of 70 °C, there are high irreversible losses of the remanence field. As it is expected that temperatures up to 100 °C occur at the magnets during the welding process, *Vacodym 745 HR* is not a suitable material for the PMS system. *Vacodym 837 TP* exhibits exclusively reversible losses up to a temperature of 110 °C, so that its remanence field of $B_R = 1.37\,\mathrm{T}$ at room temperature is restored after the welding [3]. Hence, *Vacodym 837 TP* combines a large remanence with a sufficient heat resistance and is going to be utilized for the PMSs at REGAE. The

algorithm, which has been used to find the optimal dimensions of set-up 4 in section 3.4, is again performed with the new surface current density $\rho = B_R/\mu_0 = 1.09 \times 10^6\,\mathrm{A/m}$.

Since the redesign of the magnetic shielding in the next section will also cause small modifications on the dimensions of the PMS, the effects of all changes — including the segmentation, dimension and remanence changes and the influence of the shielding — on the focusing properties are presented in the last section.

5.2 Redesign of the magnetic shielding

The design of a light weight magnetic shielding has led to some special measures, as documented in chapter 4. But especially the important modulation of the wall thickness along the shielding turned out to be very difficult to manufacture. In combination with the required thin walls ($< 1\,\mathrm{mm}$) at some positions (cf. figure 4.18), even expensive and complex methods like lathing two halves out of a solid block are not feasible. Hence, a simplification of the shielding's shape is required, but the very important constancy of the relative permeability along the shielding has to be retained.
One idea is to transform the shielding cylinder with modulated wall thickness into a cylinder with gaps parallel to the magnetic flux and constant wall thickness. Under the assumption, that the same amount of magnetic flux flows through the shielding with gaps, the calculations for achieving a constant permeability/magnetic flux density are still valid. The used definition of the magnetic flux $\Phi = BA \;\Leftrightarrow\; B = \Phi/A$ refers to the cross sectional area A of the shielding, which is perpendicular to the magnetic flux Hence, the modulation of the cross sectional area A along the course of the field lines within the shielding can be either achieved by a thickness modulation or by creating gaps with varying width. To illustrate the idea, figure 5.2 shows a magnetic shielding with forty gaps. The design considerations of this shielding are discussed in the following.
A first important property of shieldings with gaps are the number of gaps respectively shielding stripes. The smaller the number of the shielding stripes is, the larger is the maximal gap width of every single gap (indicated by the red line in figure 5.2). This is the case, although the sum of the maximal gap widths is independent from the number of stripes. Three dimensional simulations with CST EM Studio concerning this topic have shown, that a shielding with twenty stripes and a maximal gap size of 14 mm is almost one order of magnitude less effective than the closed cylinder if one evaluates the maximal $B_y(0, 0.1, z)$-component on a line with 100 mm vertical distance to the solenoid axis. Later in this section one can see, that a shielding with 40 stripes and a maximal gap size of 4.5 mm is as effective as the shielding with thickness modulation.
In conclusion, shieldings with holes or gaps can reach the same shielding quality as closed

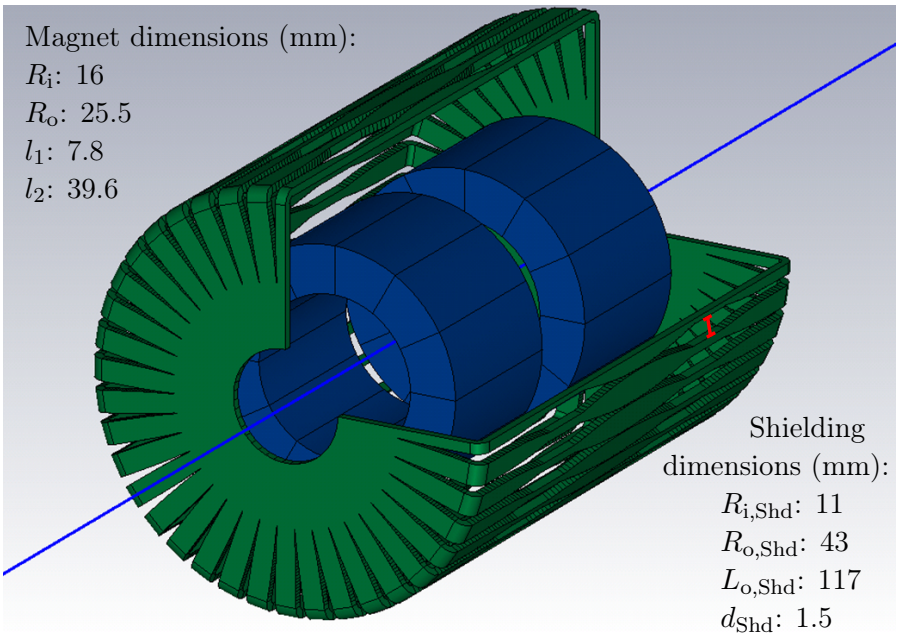

Figure 5.2 – The final shielding design with longitudinal gaps instead of a thickness modulation. The dimensions of the PMS and the shielding are given. The red line indicates the maximal gap width.

shieldings. But it is important that the gaps are not too large, so that the way into the shielding is still energetically favorable for magnetic field lines arriving in the middle of the gap. Under this condition, the flux inside a shielding with gaps and a shielding with wall thickness-modulations is actually equal. Hence, the calculations to achieve a constant permeability from section 4.2 are still valid but implemented with gaps here.
The minimum wall thickness of the shielding stripes (not the width) is given by the maximal thickness $d_{\max}$, which occurs in the set-up of the thickness modulation. If this thickness is chosen, the shielding stripes touch at the position of the maximal thickness and their width b along the shielding is generally given by

$$b(z) = 2\frac{d(z)}{d_{\max}} \tan\left(\frac{2\pi}{2n}\right)(R_{o,Shd} - d_{\max}), \tag{5.1}$$

where n defines the number of stripes and $d(z)$ indicates the function shown in figure 4.17 (a). For the caps of the cylinder $d(z)$, $b(z)$ and $R_{o,Shd}$ have to be replaced by $d(r)$, $b(r)$ and r respectively. The function $d(r)$ is depicted in figure 4.17 (b).

By means of equation (5.1), the width of the stripes is determined for the thickness modulation, which was calculated in section 4.2.1. Here, a problem arises due to the

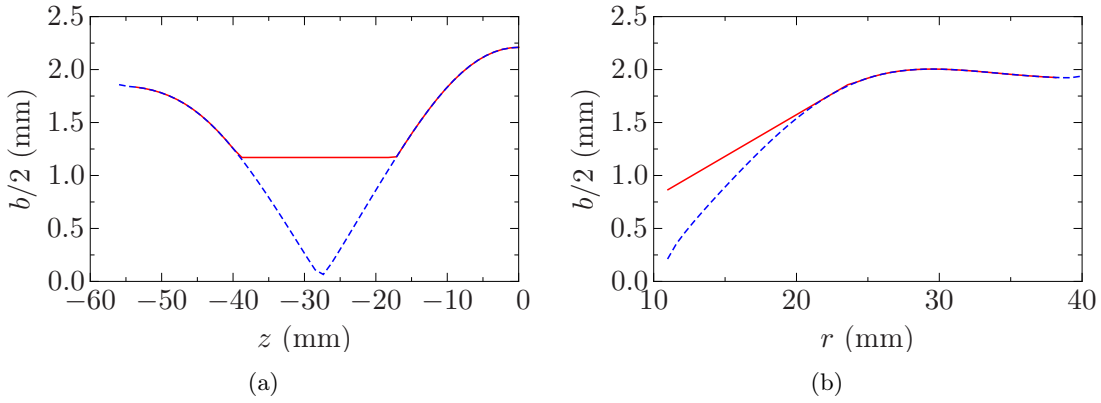

Figure 5.3 – The width of the shielding stripes before the modification, which yields $d_{\max} \leq 1.5\,\mathrm{mm}$. (a) The blue dashed curve shows the half width $b/2$ of a shielding stripe, if no fabrication constraints are applied. Very tiny structures occur. With constraints, the shielding stripe is represented by the red curve. (b) Analogously, $b/2$ is shown for the cylinder cap. For the half width, shown as red curve, the stripes adjoin to each other for stability.

relative large value of $d_{\max} = 2.34\,\mathrm{mm}$, which is reached at the caps of the cylinder. It leads to very small widths of the stripes along the cylinder jacket, as can be seen in figure 5.3 (a). These small widths are inconvenient in the production and for the mechanical stability. For ease of the production, the width of the stripes should be comparable to their thickness. This constraint leads to a shape, which is also shown in figure 5.3 (a). The weight of the additional iron, which does not improve the shielding behavior, is 35 g and therewith almost 10 % of the whole weight. It can be reduced by bringing the maxima of $d(z)$ and $d(r)$ closer to each other. Furthermore, the standard wall thicknesses for sheets of magnetic iron should be considered. Since DESY has sheets of high-quality magnetic iron with a thickness of 1.5 mm on stock, the current set-up is slightly modified to fulfill $d_{\max} \leq 1.5\,\mathrm{mm}$ and $d_{\max}(z) \approx d_{\max}(r)$. It cannot be achieved by only changing the shielding dimensions but also requires a change of the PMS dimensions, in order to reduce the flux in the shielding caps. This step is accompanied by a slight decrease of the focusing performance by 6 % . The parameters, shown in figure 5.2, allow the use of the 1.5 mm iron sheets, since $d_{\max}(z) = 1.48\,\mathrm{mm}$ and $d_{\max}(r) = 1.44\,\mathrm{mm}$ is achieved for the final set-up. The modulated width of the forty stripes is illustrated in figure 5.4. Again, material has to be added on the cylinder jacket for stability and producibility reasons. But the weight of the material, which is redundant with the perspective on the shielding quality, is reduced to 10 g. Also the part of the stripe for the cylinder cap is producible and stable, if one adds a small amount of material (5 g) so that the stripes touch in the

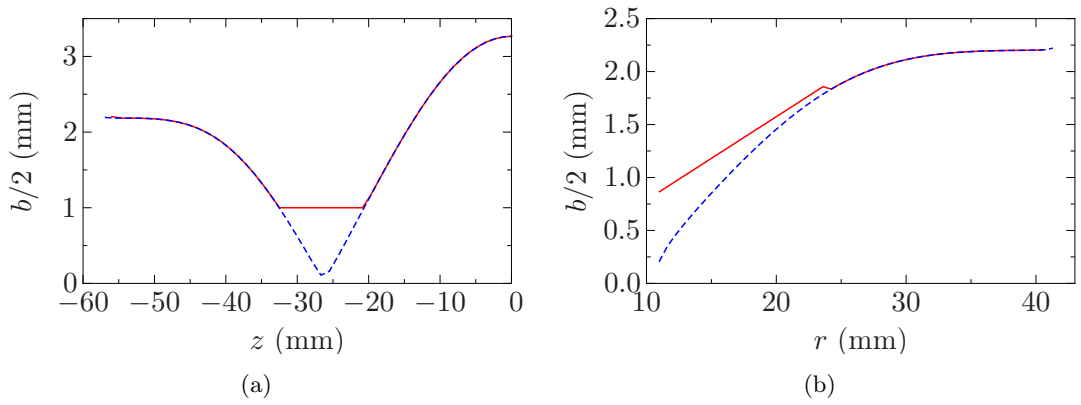

Figure 5.4 – The width of the shielding stripes after the modification. (a) The blue dashed curve shows the calculated half width $b/2$. With the constraint $b/2 > 1\,\text{mm}$, the final shielding stripe is represented by the red curve. (b) Analogously, $b/2$ is shown for the shielding cap. The step in the red curve marks the point, where the stripes adjoin for additional stability (from $r = 11\,\text{mm}$ to $r = 23\,\text{mm}$).

middle of the cap. Finally, these stripes can be cut out of iron sheets by wire eroding or water jet cutting. After being bent, they can be mounted onto a holding structure and form the shielding, which is already shown in figure 5.2.

5.3 Effects of the segmentation and production tolerances

Figure 5.2 shows the final set-up of the PMS in combination with its magnetic shielding. In order to conclusively assess its properties from a beam dynamics point of view, 3D FEM simulations with CST EM Studio [54] and particle tracking simulations with ASTRA (A Space Charge Tracking Algorithm) [57] are performed. Here, three different methods can be applied, which yield the possibility to compare their results.
In the first method the longitudinal on-axis field is extracted from the 3D FEM simulation. This field is shown in figure 5.5 for the case with and without the magnetic shielding. A comparison between the longitudinal on-axis field of a perfect radially magnetized solenoid (green dashed curve) and an approximation by twelve wedges (blue curve) shows only negligible small deviations. Nevertheless, the subsequent numerical determination of the second and third field integral is only valid for the perfect radially magnetized solenoid. In the case of the wedges the cylindrically symmetry is broken, which excludes this possibility. Hence, this method is only applied for the perfect case. The field integrals can be inserted into the equations (2.33) and (2.52), which yields the

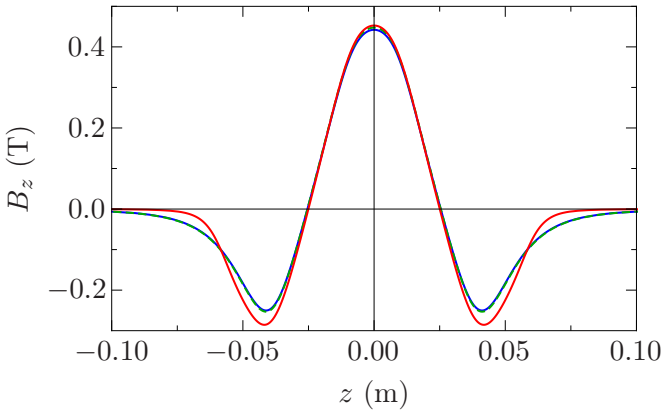

Figure 5.5 – The longitudinal on-axis field of the final PMS design. The blue curve shows the field for a perfect radially magnetized solenoid without shielding. The red curve and the green dashed curve show the field of the twelve wedges with and without the shielding respectively.

focusing strength and emittance growth within the thin lens approximation. For the calculation of the emittance growth a radial uniform transverse beam distribution with $\sigma_{x,y} = 0.53\,\text{mm}$ is assumed. This value is for good measure 50 % larger than in the design simulation of the external injection experiment and will be used for all following emittance growth determinations. The results are documented in table 5.1 and provide a possibility of comparison for the final set-up with the wedges.
The second method is to implement the longitudinal on-axis field in a particle tracking simulation, performed with ASTRA. The advantage here is that the thin lens approximation is not required. Furthermore it provides results for the focal spot size and the distance between the principle plane of the PMS and the focal spot if a prefocused bunch enters the solenoid. These simulations are performed with the design parameters of the external injection experiment, while the emittance growth simulation is still performed with $\sigma_{x,y} = 0.53\,\text{mm}$ at the PMS. The results are shown in table 5.1. They are in good agreement with the results from the first method. As expected, the results for the emittance growth are slightly smaller than the results from the first method, since the thin lens approximation is not applied (cf. section 2.1.3). But again, it is only exact for the perfect radially magnetized solenoid.
The third method is applicable to both cases. Here a 3D fieldmap is extracted from the FEM simulation. It can be included in ASTRA for particle tracking simulations. The advantage of this method is that not only the case with the wedges can be simulated but also the effects of the production tolerances can be observed. The disadvantage is that very accurate simulations of the magnetic field are required.

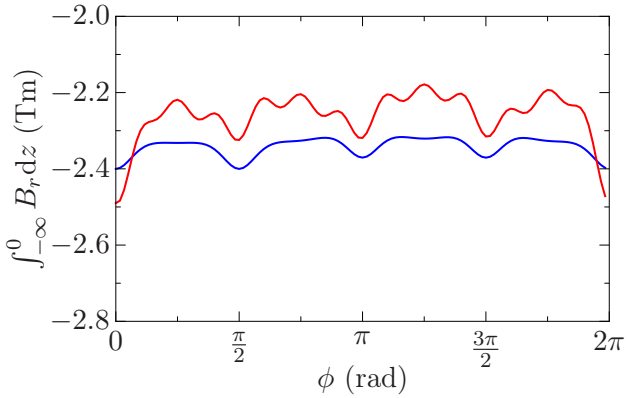

Figure 5.6 – The integral of the radial magnetic field component B_r over z is shown on a concentric circle with a radius of $r = 10\,\mathrm{mm}$ in the x-y-plane. The blue curve shows the field for the perfect radially magnetized solenoids, the red curve for the set-up consisting of twenty-four wedges. The integral is only executed from $z = 0.5\,\mathrm{m}$ to $z = 0\,\mathrm{m}$ so that a large magnitude is reached (B_r exhibits a change of sign at $z = 0$).

Regarding table 5.1, one can see that the emittance growth, determined by this method is about thirty times larger than the emittance growth, which is calculated by the first two methods. This large difference is unphysical since the second and the third method, which are both applicable to the ideal case, should yield identical results. Hence, the deviation must be caused by numerical problems. One numerical problem with respect to the third method is noticeable in figure 5.6. Of course, the radial magnetic field component B_r and its integral along z should be constant on a concentric circle in the x-y-plane for the ideal case. But the simulations show deviations of $\pm 2\,\%$ from the mean value. Nevertheless it is unlikely, that this relative small inadequacy of the simulation causes the large errors. Thus there must be other numerical problems. Further investigations are required here.
Despite the inaccuracy of the simulation, a first estimation of the effects, which are caused by the wedges and their production tolerances are made.
The simulation results of the set-up with perfect wedges show the expected B_r-modulations with twelve periods in figure 5.6. The variations of $\pm 7\,\%$ on a circle with 10 mm radius — notice the transverse beam size of $\sigma_{\mathrm{x,y}} = 0.53\,\mathrm{mm}$ — seem again too small to cause the peculiar results for the emittance growth, shown in the third last line of table 5.1.
The effects of the production tolerances are assessed in multiple simulations. The specifications of the manufacturer concerning the tolerances are $\pm 3°$ in the magnetization direction and $\pm 3\,\%$ for the remanence field. Both specifications are Peak-to-Peak val-

ues and the distribution within these borders is assumed to be uniform. Within these specifications the errors of the twenty-four wedges are randomly chosen and the wedges are not rearranged. This procedure is repeated for ten simulations. The worst and the best result with respect to the emittance growth are shown in the last two lines of table 5.1. The worst result with an emittance growth of about $4\,\pi$ mm mrad reveals that the arbitrary arrangement of the wedges is not sufficient.
In consequence it is necessary to measure the actual errors for every wedge. Subsequently they can be assembled such that their errors cancel out each other. Since the best random arrangement already exhibits an emittance growth, which is "only" twice as large as for the perfect radially magnetized solenoid, an optimized arrangement should allow for results close to the ideal case.

In conclusion, the presented simulations are not accurate enough to make quantitative statements. But they show that certain random distributions of the wedges with production tolerances obviously have a significant effect on the focusing properties of the PMS despite the large aperture of 32 mm.
On the other hand they indicate that an optimized arrangement of the wedges should yield an emittance growth similar to the one of the ideal case. For the determination of the best arrangement and for quantitative statements, the numerical problems of the 3D FEM simulations have to be identified and solved. It is also planned to develop an analytical model, which can describe the wedges with their production tolerances. Here, the magnetic field induced by surface currents of the wedges can be calculated by means of Biot Savart's law (cf. section 2.2.2). The knowledge about the right arrangement of the wedges, which will be gained during the development of this model, is necessary to preselect suitable combinations. This is important since 24! possibilities can neither be assessed with FEM simulations nor with the analytical model.

	F_2 (T^2 mm)	$f_{5.6}$ (mm)	$f_{5.6\ \text{p.f.}}$ (mm)	f_3 (mm)	F_3 (T^2/m)	ϵ_n (π µm rad)	σ_{min} (µm)
I.C. w/Shd. Meth.1	8.12	205	—	68	19.2	0.01	—
I.C. w/Shd. Meth.2	—	217	172	78	—	0.008	2.3
I.C. Meth.1	7.43	224	—	74	16.5	0.009	—
I.C. Meth.2	—	237	184	84	—	0.007	2
I.C. Meth.3	—	236	184	84	—	0.284	9.5
24 W. w/o tol. Meth.3	—	238 245	184 189	84 87	—	0.153 0.02	5.5 2.1
24 W. w/ tol. Meth.3	—	315 173	229 144	97 75	—	3.866 3.692	111 59.3
24 W. w/ tol. Meth.3	—	233 253	181 196	82 90	—	0.598 0.45	14.1 4.4

Table 5.1 – Focusing properties of the final design with and without shielding. The set-up with shielding is investigated under the assumption of a perfect radially magnetized solenoid (I.C. w/Shd., I.C. stands for ideal case). The set-up without shielding is investigated for the case of a perfect radially magnetized solenoid (I.C.), for the case of twenty-four wedges without consideration of production tolerances (24 W. w/o tol.) and for the case of wedges with production tolerances (24 W. w/ tol.). Three different methods, which are explained in the text, are used. In the case of a perfect radially magnetized solenoid all three methods can be applied. Here, the comparison of the results reveals numerical problems of method 3. As results are shown the two field integrals F_2 and F_3, the focal length for a beam with kinetic energies of 5.6 MeV and 3 MeV ($f_{5.6}$, f_3) and the emittance growth for a radial uniform beam with $\sigma_{x,y} = 0.53$ mm at the entrance of the solenoid. $f_{5.6\ \text{p.f.}}$ and σ_{min} refer to start-to-end simulations with design parameters of the external injection experiment. $f_{5.6\ \text{p.f.}}$ defines the distance between the mid plane of the PMS and the focal spot, σ_{min} is the focal spot size. In cases, where differences in the x and y direction occur, the values of both directions are given.

6 Conclusion and Outlook

In the present thesis the design of a permanent magnetic solenoid (PMS) for REGAE is discussed. It will be deployed for two future experiments, the external injection experiment and the transmission electron microscope. The requirements, which result from these two experiments, are fulfilled by the developed design.
A large focusing strength is needed for a small transverse beam size at the entrance of the gas target in the external injection experiment and for a large magnification in the transmission electron microscope. This is achieved by the presented PMS designs. In comparison, achieving the required focusing strength with a typical electromagnetic solenoid has shown to be difficult. Furthermore, the PMS design is much more compact and allows for a positioning directly in front of the target inside the target chamber.
A second demand is a small emittance growth induced by the PMS. This characteristic is assessed for different designs. Therefore a description of the beam dynamics in the solenoid — based on four field integrals of the longitudinal on-axis magnetic field — is used. It reveals the close relation between the emittance growth and the spherical aberration coefficient. The investigations of the different designs have shown that the induced emittance growth for two radially magnetized PMSs is considerably smaller than for an axially magnetized PMS, if a weight limitation has to be applied. In the particular case at REGAE, a reduction of the emittance growth by 65 % is feasible. The utilization of two axially magnetized PMSs or a modulation of the inner radius do not yield significant improvements.
Not only the design of a PMS has been performed but also the development of a magnetic shielding, which surrounds the PMS. It assures that the three different experiments in the target chamber do not disturb each other by magnetic leakage fields. Since the PMS and the shielding are mounted onto a micropositioning stage with a limited load capacity, the whole system has to weigh below 1.5 kg. In order to fulfill the weight restriction special measures have been carried out during the shielding design. Here, the most effective method is the adaption of the wall thickness to the local magnetic flux inside the shielding. It allows for a large and constant permeability. Thus, a shielding of two radially magnetized solenoids with a weight below 400 g exhibits a sufficient shielding effect. If the system is removed by a distance of 100 mm from the beam, a deflection of 50 µm (parallel offset) occurs for an electron bunch with $\gamma = 12$. Such a deviation is

acceptable for all three experiments.
In the last part of this thesis, the technical implementation of the theoretical design considerations is discussed. The radially magnetized solenoid can only be approximated by a certain amount of wedges with an unidirectional magnetization. The effects of this segmentation and of the fabrication tolerances for permanent magnets are taken into account in simulations. It is shown that an arbitrary arrangement of the wedges with their individual fabrication tolerances is not sufficient in order to achieve the small emittance and focal spot size, which is aimed-at. But once having measured the remanence field and the magnetization direction for each of the twenty-four wedges, it should be possible to find an arrangement, where a large part of the fabrication errors are canceled out.
A magnetic shielding with a modulated wall thickness is not impossible to fabricate but very complex and expensive. In order facilitate the fabrication, the thickness modulation is transformed into a shielding with gaps of varying width but constant wall thickness. This redesign allows to fabricate the shielding from sheets of magnetic iron. Simulations have shown that the shielding quality is not diminished by gaps, as long as they do not exceed a certain width.

All in all this thesis provides a complete and detailed design approach of a PMS focusing system, which is mandatory for the external injection experiment and the TEM at REGAE. In chapter 3 four different set-ups of PMSs are compared with respect to their focusing properties. The comparison is based on a description of the beam dynamics, which utilizes four field integrals of the longitudinal on-axis field. For the two most suitable set-ups a magnetic shielding is developed in chapter 4. It is required to assure that three different experiments can be performed in the target chamber at REGAE. A solution to the problem that the PMS and the shielding have to weigh below 1.5 kg is proposed. Chapter 5 deals with the technical implementation. The PMS and the shielding are redesigned such that they can be fabricated. The consideration of the fabrication tolerances shows that the arrangement of the PMS wedges has to be optimized.

Outlook

As already mentioned in the conclusion, the fabrication tolerances lead to a negative effect on the focusing properties of the PMS. This applies only for the case where the wedges with their individual errors are arbitrarily arranged within the rings. In order to minimize these effects, the error in the remanence field and the magnetization direction should be measured for every wedge. Subsequently an arrangement of the wedges has to be determined such that their errors are optimally cancelled out. One way to find the optimal arrangement of the wedges is to develop an analytical model, with which it is

possible to calculate the magnetic field induced by surface currents of the twenty-four wedges by means of Biot Savart's law. Although the results of this analytical model and of 3D FEM simulations can be cross checked for the final arrangement, a measurement of a 3D fieldmap is essential.
If the measured magnetic field is in good agreement with the calculations and fulfills the requirements for the external injection experiment and the TEM, the two PMS systems are ready to be integrated into the new target chamber. A procedure for a beam based alignment has to be developed. It is planned to extend the already existing procedure for the electromagnetic solenoids to the PMS. The fact that the PMS systems are mounted onto stages with an accuracy below 10 nm allows for a very accurate alignment.
After this step, the beam optic components at REGAE will be able to generate focal spot sizes below 10 µm at the target. Thus they are ready for the external injection experiment. As described in more detail in the introduction, this experiment will merge conventional and laser wakefield accelerators by utilizing the strong focused, sub 10 fs short and low emittance electron bunches — which REGAE can generate — in order to investigate a linear wakefield [5]. The aim is to provide a method for direct reconstruction of the electric field within the wakefield. Therefore, the external injection experiment can be an important complement to theoretical models and particle-in-cell (PIC) simulations, describing and optimizing laser wakefields for electron acceleration.

For the TEM experiment, all required beam optic elements in front of the target will be installed as soon as the PMS systems are implemented into the new target chamber. Also the objective lens, which is the second PMS system behind the target, will be ready. This lens plays a key role for the quality of the TEM and should provide a strong focusing strength and a small emittance growth. Both properties have been optimized for the PMS.
The intermediate lenses, which will be located downstream of the objective lens, still have to be designed. As soon as they are implemented, real space imaging at REGAE is possible. As explained in the introduction, this high energy TEM will allow for a time resolution on the order of picoseconds, if pump probe experiments are performed. This is a huge advantage over conventional TEMs, which have typically time resolutions of milliseconds. Furthermore a high energy TEM has the two advantages of a decreased sample damage and an increased maximal sample thickness. Hence, a high energy TEM could allow to perform living cell imaging.

Bibliography

[1] O. Klemperer and M. Barnett. *Electron Optics*. Cambridge University Press, 1971.

[2] P.W. Hawkes and E. Kasper. *Principles of Electron Optics*, volume 1. Academic Press, 1996.

[3] Vacuumschmelze GmbH & Co. KG. Seltene-Erd-Dauermagnete: VACODYM VACOMAX. Technical report, Vacuumschmelze GmbH & Co. KG, Grüner Weg 37, D 63450 Hanau, 2012.

[4] Klaus Halbach. Physical and optical properties of rare earth cobalt magnets. *Nuclear Instruments and Methods in Physics Research*, 187(1):109–117, August 1981.

[5] Benno Zeitler, Irene Dornmair, Tim Gehrke, Mikheil Titberidze, Andreas R. Maier, Bernhard Hidding, Klaus Flöttmann, and Florian Grüner. Merging conventional and laser wakefield accelerators. *SPIE Proceedings*, 8779:877904–877904, May 2013.

[6] T. Mehrling, J. Grebenyuk, F. S. Tsung, K. Floettmann, and J. Osterhoff. Transverse emittance growth in staged laser-wakefield acceleration. *Phys. Rev. ST Accel. Beams*, 15(11):111303–, November 2012.

[7] R. J. Dwayne Miller, Ralph Ernstorfer, Maher Harb, Meng Gao, Christoph T. Hebeisen, Hubert Jean-Ruel, Cheng Lu, Gustavo Moriena, and German Sciaini. 'making the molecular movie': first frames. *Acta Crystallographica Section A*, 66(2):137–156, 2010.

[8] Bradley J. Siwick, Jason R. Dwyer, Robert E. Jordan, and R. J. Dwayne Miller. An atomic-level view of melting using femtosecond electron diffraction. *Science*, 302(5649):1382–1385, 2003.

[9] Max Hachmann. Transverse emittance measurement at REGAE via a solenoid scan. Master's thesis, Institut Experimentalphysik- Universität Hamburg, November 2012.

[10] Frank Mayet. Simulation and characterization of the RF system and global stability analysis at the REGAE linear electron accelerator. Master's thesis, Department Physik- Universität Hamburg, Oktober 2012.

[11] Klaus Floettmann. Design and performance of printed circuit steering magnets for the flash injector. In *Proceedings of IPAC*, 2010.

[12] Hossein Delsim-Hashemi. Imaging detector for Relativistic-Electron-Microscope regae. Technical Report 5, DESY, October 2012.

[13] T. Gehrke. Earth magnetic and AC magnetic field measurements and compensation at REGAE. Technical report, DESY, 2012.

[14] T. Tajima and J. M. Dawson. Laser electron accelerator. *Phys. Rev. Lett.*, 43(4):267–270, July 1979.

[15] E. Esarey, C. B. Schroeder, and W. P. Leemans. Physics of laser-driven plasma-based electron accelerators. *Rev. Mod. Phys.*, 81(3):1229–1285, August 2009.

[16] W. P. Leemans, B. Nagler, A. J. Gonsalves, Cs. Toth, K. Nakamura, C. G. R. Geddes, E. Esarey, C. B. Schroeder, and S. M. Hooker. Gev electron beams from a centimetre-scale accelerator. *Nat Phys*, 2(10):696–699, October 2006.

[17] Matthias Fuchs, Raphael Weingartner, Antonia Popp, Zsuzsanna Major, Stefan Becker, Jens Osterhoff, Isabella Cortrie, Benno Zeitler, Rainer Horlein, George D. Tsakiris, Ulrich Schramm, Tom P. Rowlands-Rees, Simon M. Hooker, Dietrich Habs, Ferenc Krausz, Stefan Karsch, and Florian Gruner. Laser-driven soft-x-ray undulator source. *Nat Phys*, 5(11):826–829, November 2009.

[18] S. Kneip, C. McGuffey, J. L. Martins, S. F. Martins, C. Bellei, V. Chvykov, F. Dollar, R. Fonseca, C. Huntington, G. Kalintchenko, A. Maksimchuk, S. P. D. Mangles, T. Matsuoka, S. R. Nagel, C. A. J. Palmer, J. Schreiber, K. Ta Phuoc, A. G. R. Thomas, V. Yanovsky, L. O. Silva, K. Krushelnick, and Z. Najmudin. Bright spatially coherent synchrotron x-rays from a table-top source. *Nat Phys*, 7(9):737–737, September 2011.

[19] A. R. Maier. Stable water-window x-ray pulses from a laser-plasma driven undulator. in preparation, 2013.

[20] F. Grüner, S. Becker, U. Schramm, T. Eichner, M. Fuchs, R. Weingartner, D. Habs, J. Meyer-ter Vehn, M. Geissler, M. Ferrario, L. Serafini, B. van der Geer, H. Backe, W. Lauth, and S. Reiche. Design considerations for table-top, laser-based vuv and x-ray free electron lasers. *Applied Physics B: Lasers and Optics*, 86(3):431–435, 2007-02-01.

[21] F. J. Grüner, C. B. Schroeder, A. R. Maier, S. Becker, and J. M. Mikhailova. Space-charge effects in ultrahigh current electron bunches generated by laser-plasma accelerators. *Phys. Rev. ST Accel. Beams*, 12(2):020701–, February 2009.

[22] Kazuhisa Nakajima. Compact x-ray sources: Towards a table-top free-electron laser. *Nat Phys*, 4(2):92–93, February 2008.

[23] R. Weingartner, S. Raith, A. Popp, S. Chou, J. Wenz, K. Khrennikov, M. Heigoldt, A. R. Maier, N. Kajumba, M. Fuchs, B. Zeitler, F. Krausz, S. Karsch, and F. Grüner. Ultralow emittance electron beams from a laser-wakefield accelerator. *Phys. Rev. ST Accel. Beams*, 15(11):111302–, November 2012.

[24] A. Pukhov and J. Meyer-ter Vehn. Laser wake field acceleration: the highly non-linear broken-wave regime, 2002-04-15.

[25] B. Zeitler. REGAE beamline extension. Technical report, University of Hamburg, Center for Free-Electron Laser Science, 2012.

[26] U. Hahn and K. Zapfe. Richtlinien für UHV-Komponenten bei DESY. Technische Spezifikation Nr.: Vakuum 005/2008; Version 1.6 / 22.09.2010, DESY, 2010.

[27] M. Knoll and E. Ruska. Das elektronenmikroskop. *Zeitschrift für Physik*, 78(5-6):318–339–, 1932.

[28] Rolf Erni, Marta D. Rossell, Christian Kisielowski, and Ulrich Dahmen. Atomic-resolution imaging with a sub-50-pm electron probe. *Phys. Rev. Lett.*, 102(9):096101–, March 2009.

[29] N.D. Browning, M.A. Bonds, G.H. Campbell, J.E. Evans, T. LaGrange, K.L. Jungjohann, D.J. Masiel, J. McKeown, S. Mehraeen, B.W. Reed, and M. Santala. Recent developments in dynamic transmission electron microscopy. *Current Opinion in Solid State and Materials Science*, 16(1):23–30, February 2012.

[30] Ramesh Srinivasan, Vladimir Lobastov, Chong-Yu Ruan, and Ahmed Zewail. Ultrafast electron diffraction (ued). *HCA*, 86(6):1761–1799, 2003.

[31] Stephanie Manz. Towards ultrafast electron diffraction and dynamic microscopy with regae. Poster, 2013.

[32] J.D. Jackson and K. Müller. *Klassische Elektrodynamik*. Walter De Gruyter Incorporated, 2002.

[33] Sekels GmbH. Magnetische Abschirmungen: Grundlagen, Lieferprogramm, Messtechnik. `http://www.sekels.com/`.

[34] Vacuumschmelze GmbH. Magnetische Abschirmungen. `http://www.vacuumschmelze.com/`, 1988.

[35] H. Busch. Berechnung der Bahn von Kathodenstrahlen im axialsymmetrischen elektromagnetischen Felde. *Ann. Phys.*, 386(25):974–993, 1926.

[36] J. Rossbach and P. Schmüser. Basic course on accelerator optics, Feb 1993.

[37] Vinit Kumar. Understanding the focusing of charged particle beams in a solenoid magnetic field. *Am. J. Phys.*, 77(8):737–741, August 2009.

[38] W. Glaser. *Grundlagen der Elektronenoptik*. Springer-Verlag Wien, 1952.

[39] M. Reiser. *Theory and Design of Charged Particle Beams*. Wiley, 2008.

[40] Walter Glaser. Strenge Berechnung magnetischer Linsen der Feldform $h = h_0/(1 + (z/a)^2)$. *Zeitschrift für Physik*, 117(5-6):285–315–, 1941.

[41] W. Demtröder. *Experimentalphysik 2 Elektrizität und Optik*. Springer-Verlag Berlin Heidelberg, Fünfte, überarbeitete und erweiterte Auflage, 2009.

[42] Vector Fields Limited. OPERA-2D. `http://www.cobham.com/about-cobham/aerospace-and-security/about-us/antenna-systems/specialist-technical-services-and-software/products-and-services/design-simulation-software.aspx`, 2011.

[43] Thomas R. Lyle. Xxxii. on circular filaments or circular magnetic shells equivalent to circular coils, and on the equivalent radius of a coil. *Philosophical Magazine Series 6*, 3(15):310–329, 1902.

[44] P. Grivet. *Electron Optics*. Pergamon Press Oxford, 1965.

[45] Friedrich Lenz. Berechnung der elektronenoptischen kenngrößen eines speziellen magnetischen linsenfeldes ohne numerische bahnintegrationen. *Ann. Phys.*, 444(5):245–258, 1951.

[46] P. Durandeau. Construction des lentilles electroniques magnetiques. *J. Phys. Radium*, 17:18A – 25A, 1956.

[47] G. Liebmann. A unified representation of magnetic electron lens properties. *Proc. Phys. Soc.*, B68:679 – 685, 737 – 745, 1955.

[48] S. Becker, M. Bussmann, S. Raith, M. Fuchs, R. Weingartner, P. Kunz, W. Lauth, U. Schramm, M. El Ghazaly, F. Grüner, H. Backe, and D. Habs. Characterization and tuning of ultrahigh gradient permanent magnet quadrupoles. *Phys. Rev. ST Accel. Beams*, 12(10):102801–, October 2009.

[49] A.L. Septier. *Focusing of Charged Particles*. Number Vol. 1. Academic Press, 1967.

[50] K. Flöttmann. Beam dynamics in RF guns and injectors. Draft Version, Jan 2011.

[51] VACUUMSCHMELZE GmbH. `http://www.vacuumschmelze.com/`, 2013.

[52] K. Flöttmann. Private Communication. On Solenoids.

[53] P.W. Hawkes and E. Kasper. *Principles of Electron Optics*, volume 2. Academic Press, 1996.

[54] EM Studio. Version 2013.01. CST AG, Darmstadt, Germany, 2013. `http://www.cst.com`.

[55] Vacuumschmelze GmbH & Co. KG. Mumetall zur Abschirmung statischer und niederfrequenter Magnetfelder. Technical report, Vacuumschmelze GmbH & Co. KG, 2011.

[56] Vacuumschmelze GmbH & Co. KG. Weichmagnetische Kobalt-Eisen-Legierungen. Technical report, Vacuumschmelze GmbH & Co. KG, 2001.

[57] K. Floettmann. *ASTRA - A Space Charge Tracking Algorithm*. DESY, Version 3.0, October 2011.

Acknowledgments

First of all I would like to thank Prof. Dr. Florian Grüner for giving me the opportunity to do my master thesis in his group. It was a great experience to work in this innovative community.

I also want to thank Dr. Klaus Flöttmann, my supervisor throughout the last year. He supported me in every aspect of this work and has always taken the time to faithfully discuss open questions. I admire his great experience and knowledge, from which I could learn a lot.

Furthermore I like to thank Benno Zeitler. He could answer all my questions concerning the remarkable external injection experiment, which he drives forward with great dedication. I am thankful, that he took the time to proofread the prototype of this thesis.
The encouragements to work "Faster" and to achieve "Excellent results" have always cheered the whole office.

I thank Stephanie Manz, with whom I could discuss the design of any magnetic lens, and Michaela Marx, who supported me in questions about the FEM simulations. Darek Kocon helped me in the final stage of construction and I am very grateful for that.
Last but not least I want to thank the whole group. I enjoyed the pleasant working atmosphere and the great helpfulness among each other.

Erklärung

Hiermit bestätige ich, dass die vorliegende Arbeit von mir selbstständig verfasst wurde und ich keine anderen als die angegebenen Hilfsmittel — insbesondere keine im Quellenverzeichnis nicht benannten Internet-Quellen — benutzt habe und die Arbeit von mir vorher nicht einem anderen Prüfungsverfahren eingereicht wurde. Die eingereichte schriftliche Fassung entspricht der auf dem elektronischen Speichermedium. Ich bin damit einverstanden, dass die Masterarbeit veröffentlicht wird.

Ort, Datum

Unterschrift